

LOAN DOCUMENT

PHOTOGRAPH THIS SHEET

LEVEL

INVENTORY

AD-A238 756



DTIC ACCESSION NUMBER

WRDC-TR-90-4059

DOCUMENT IDENTIFICATION

Aug 1990

DISTRIBUTION STATEMENT

H
A
N
D
L
E

W
I
T
H

C
A
R
E

ACCESSION FOR	
NTIS	GRA&I <input checked="" type="checkbox"/>
DTIC	TRAC <input type="checkbox"/>
UNANNOUNCED	<input type="checkbox"/>
JUSTIFICATION	
BY	
DISTRIBUTION/	
AVAILABILITY CODES	
DISTRIBUTION	AVAILABILITY AND/OR SPECIAL
A-1	

DISTRIBUTION STAMP

DATE ACCESSIONED

DATE ACCESSIONED

DATE RETURNED

DATE RETURNED

91 7 28 045

DATE RECEIVED IN DTIC

91-05971

REGISTERED OR CERTIFIED NUMBER

PHOTOGRAPH THIS SHEET AND RETURN TO DTIC-FDAC

AD-A238 756



WRDC-TR-90-4059

CREEP OF OXIDE SINGLE CRYSTALS



G.S. Corman

GE Corporate Research and Development
P.O. Box 8
Schenectady, NY 12301

August 1990

Final Report for Period September 1987 - September 1989

Approved for public release; distribution unlimited.

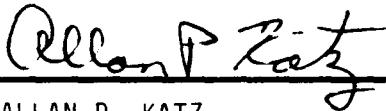
MATERIALS LABORATORY
WRIGHT RESEARCH AND DEVELOPMENT CENTER
AIR FORCE SYSTEMS COMMAND
WRIGHT-PATTERSON AIR FORCE BASE, OHIO 45433-6533

NOTICE

WHEN GOVERNMENT DRAWINGS, SPECIFICATIONS, OR OTHER DATA ARE USED FOR ANY PURPOSE OTHER THAN IN CONNECTION WITH A DEFINITELY GOVERNMENT-RELATED PROCUREMENT, THE UNITED STATES GOVERNMENT INCURS NO RESPONSIBILITY OR ANY OBLIGATION WHATSOEVER. THE FACT THAT THE GOVERNMENT MAY HAVE FORMULATED OR IN ANY WAY SUPPLIED THE SAID DRAWINGS, SPECIFICATIONS, OR OTHER DATA, IS NOT TO BE REGARDED BY IMPLICATION, OR OTHERWISE IN ANY MANNER CONSTRUED, AS LICENSING THE HOLDER, OR ANY OTHER PERSON OR CORPORATION; OR AS CONVEYING ANY RIGHTS OR PERMISSION TO MANUFACTURE, USE, OR SELL ANY PATENTED INVENTION THAT MAY IN ANY WAY BE RELATED THERETO.

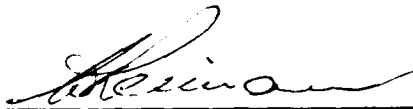
THIS REPORT HAS BEEN REVIEWED BY THE OFFICE OF PUBLIC AFFAIRS (ASD/PA) AND IS RELEASABLE TO THE NATIONAL TECHNICAL INFORMATION SERVICE (NTIS). AT NTIS IT WILL BE AVAILABLE TO THE GENERAL PUBLIC INCLUDING FOREIGN NATIONS.

THIS TECHNICAL REPORT HAS BEEN REVIEWED AND IS APPROVED FOR PUBLICATION.



ALLAN P. KATZ
Project Engineer

FOR THE COMMANDER



WALTER H. REIMANN, Chief
Materials Development Branch
Metals & Ceramics Division

IF YOUR ADDRESS HAS CHANGED, IF YOU WISH TO BE REMOVED FROM OUR MAILING LIST, OR IF THE ADDRESSEE IS NO LONGER EMPLOYED BY YOUR ORGANIZATION PLEASE NOTIFY WRDC/MLLM, WRIGHT-PATTERSON AFB, OH 45433-6533 TO HELP MAINTAIN A CURRENT MAILING LIST.

COPIES OF THIS REPORT SHOULD NOT BE RETURNED UNLESS RETURN IS REQUIRED BY SECURITY CONSIDERATIONS, CONTRACTUAL OBLIGATIONS, OR NOTICE ON A SPECIFIC DOCUMENT.

REPORT DOCUMENTATION PAGE				Form Approved OMB No. 0704-0188	
1a. REPORT SECURITY CLASSIFICATION Unclassified		1b. RESTRICTIVE MARKINGS None			
2a. SECURITY CLASSIFICATION AUTHORITY		3. DISTRIBUTION/AVAILABILITY OF REPORT Approved for public release: distribution unlimited.			
2b. DECLASSIFICATION/DOWNGRADING SCHEDULE					
4. PERFORMING ORGANIZATION REPORT NUMBER(S)		5. MONITORING ORGANIZATION REPORT NUMBER(S) WRDC-TR-90-4059			
6a. NAME OF PERFORMING ORGANIZATION GE Corporate Research & Development Center		6b. OFFICE SYMBOL (if applicable)	7a. NAME OF MONITORING ORGANIZATION Materials Laboratory (WRDC/MLLM) Wright Research Development Center		
6c. ADDRESS (City, State, and ZIP Code) P.O. Box 8 Schenectady, NY 12301		7b. ADDRESS (City, State, and ZIP Code) Wright-Patterson AFB, OH 45433-6533			
8a. NAME OF FUNDING/SPONSORING ORGANIZATION		8b. OFFICE SYMBOL (if applicable)	9. PROCUREMENT INSTRUMENT IDENTIFICATION NUMBER F33615-87-C-5345		
8c. ADDRESS (City, State, and ZIP Code)		10. SOURCE OF FUNDING NUMBERS			
		PROGRAM ELEMENT NO. 62102F	PROJECT NO. 2420	TASK NO. 01	WORK UNIT ACCESSION NO. AK
11. TITLE (Include Security Classification) Creep of Oxide Single Crystals					
12. PERSONAL AUTHOR(S) Gregory S. Corman					
13a. TYPE OF REPORT Final		13b. TIME COVERED FROM <u>Sept. 87</u> to <u>Sept. 89</u>	14. DATE OF REPORT (Year, Month, Day) August 1990		15. PAGE COUNT 97
16. SUPPLEMENTARY NOTATION					
17. COSATI CODES			18. SUBJECT TERMS (Continue on reverse if necessary and identify by block number) Ceramic Oxides, Ceramic Composites, Creep, Zirconia, Thoria, Beryllia, Yttrium-Aluminum Garnet, Alumina, Silicon Carbide, Scandia, Single Crystal		
FIELD	GROUP	SUB-GROUP			
19. ABSTRACT (Continue on reverse if necessary and identify by block number) The constant-load compressive creep behavior of single crystals of yttria-stabilized zirconia, thoria, yttrium-aluminum garnet, beryllia, alumina and silicon carbide were determined. Of the materials tested, yttrium-aluminum garnet was judged to be the best candidate for reinforcement fiber development due to its good creep resistance, low anisotropy and inherent oxidation resistance. C-axis aligned beryllia is also expected to have very good creep resistance; however, severe creep anisotropy caused by easy basal slip may limit its usefulness as a reinforcement. Data from this study and from the literature suggests that the creep resistance of cubic oxide single crystals improves as the size of the glissile dislocation Burger's vector increases.					
20. DISTRIBUTION/AVAILABILITY OF ABSTRACT <input checked="" type="checkbox"/> UNCLASSIFIED/UNLIMITED <input type="checkbox"/> SAME AS RPT. <input type="checkbox"/> DTIC USERS			21. ABSTRACT SECURITY CLASSIFICATION Unclassified		
22a. NAME OF RESPONSIBLE INDIVIDUAL Allan P. Katz		22b. TELEPHONE (Include Area Code) (513) 255-9824		22c. OFFICE SYMBOL WRDC/MLLM	

SUMMARY

Achievement of the Integrated High Performance Turbine Engine Technology (IHPTET) Initiative's goals will necessitate development of new materials systems for structural applications in these advanced propulsion systems. Such materials may need to maintain chemical, mechanical and structural stability at temperatures above 1650°C (3000°F). One promising class of candidate materials is ceramic matrix composites (CMCs). Ideally these composites would combine the superior temperature stability of ceramics with the high fracture toughness of a well-engineered composite structure.

A major problem with the development of CMCs for high temperature use is the lack of a suitable reinforcement fiber. Currently available fibers all show chemical degradation, microstructural changes, mechanical degradation, oxidative attack, or severe creep at temperature well below 1650°C in oxidizing environments. It will thus be necessary to develop a new, creep resistant, oxidatively stable fiber for this application. Such a new fiber would preferably be an oxide for oxidative stability and thermomechanical compatibility with an oxide matrix. Unfortunately, typical polycrystalline oxides are known to be susceptible to severe grain growth and creep via diffusional and grain boundary sliding mechanisms at the temperatures of interest. Single crystal oxides would therefore be necessary.

The purpose of this study was to quantitatively examine the creep behavior of several interesting single crystal oxide materials. This was done for two main reasons, the first of which was to assess the viability of the selected materials as composite reinforcements. The second, and more important reason, was that there is currently a serious lack of high temperature creep data on single crystal oxides. There are therefore very few criteria by which potentially creep resistant oxides can be identified. It was hoped that the creep data generated in this study would allow for identification of such criteria, and thereby help to guide selection of an optimum oxide for fiber development.

The primary materials studied were yttria-stabilized zirconia (YSZ), thoria, yttrium-aluminum garnet (YAG) and beryllia. We had also hoped to study scandia; however, problems with specimen quality prevented this. Limited testing was also performed on alumina and silicon carbide single crystals in order to check the accuracy of the testing technique, and to provide data for direct comparisons with that from the primary materials.

Despite their high melting points and low cation diffusivities, creep resistance of the YSZ and thoria were relatively poor. On the other hand, YAG, which was the lowest melting point material studied (1950°C), displayed the best creep resistance. Creep rates for YAG were lower than those for c-axis sapphire at comparable temperatures and stresses. This makes YAG the most creep resistant oxide known for which quantitative data exist, and a serious candidate for reinforcement filament development.

Experimental problems with platen deformation and reaction during testing prevented quantitative measurement of creep behavior of c-axis beryllia. However, when tested in such an orientation as to allow for basal slip, beryllia was found to creep significantly at temperatures as low as 650°C. This extreme anisotropy in deformation behavior would probably severely limit the performance of beryllia in high temperature composite reinforcement

applications.

Creep results on pure, 6H polytype SiC single crystals indicate that this material offers no advantage over more typical polycrystalline SiC materials. C-axis aligned crystals did display lower creep rates than any of the oxides; however, off-axis crystals deformed readily via basal slip at temperatures as low as 800°C. Moreover, creep rates for the c-axis single crystal SiC were higher than for other forms of polycrystalline SiC reported in the literature.

The creep data generated in this study, supplemented by that available from the literature, were examined with regard to identifying factors influencing the creep resistance of refractory oxide single crystals. The factor which gave the best correlation with creep resistance was size of the glissile dislocation Burgers vector. This suggests that future searches for creep resistant single crystal oxides should consider materials with complex structures and large lattice parameters.

PREFACE

This report was prepared by G.S. Corman of the General Electric Corporate Research and Development Center, Schenectady, New York. The work described was performed under the provisions of contract F33615-87-C-5345 for the Materials Laboratory, Wright Research and Development Center, Aeronautical Systems Division, during the period from September 30, 1987 to September 30, 1989. F.N. Mazandarany and K.L. Luthra acted as program managers; A.P. Katz served as the Air Force Project Engineer.

In addition to the above mentioned persons, the author wishes to thank D. Marsh of GE CRD for performing the X-ray crystal alignments. Helpful discussions with L. Matson of WRDC/MLLM, W.B. Hillig regarding material selection, and with M.K. Brun concerning design, construction and operation of the creep furnace are also greatly appreciated. Special thanks to P. Breslin for preparation of the manuscript.

TABLE OF CONTENTS

Section	Page	
1.	INTRODUCTION	1
1.1	Material Selection	2
2.	EXPERIMENTAL PROCEDURE	5
2.1	Material Sources	5
2.2	Specimen Preparation	7
2.3	Creep Testing	7
3.	RESULTS	10
3.1	Data Fitting Procedure	10
3.2	Yttria-Stabilized Zirconia	12
3.3	Thoria	28
3.4	Scandia	36
3.5	Yttrium Aluminum Garnet	36
3.6	Beryllia	50
3.7	Alumina	56
3.8	Silicon Carbide	58
4.	DISCUSSION	68
5.	CONCLUSIONS AND RECOMMENDATIONS	81
	REFERENCES	82

LIST OF ILLUSTRATIONS

Figure		Page
1	Typical as-received crystals.	6
2	Photographs of creep measurement furnace.	9
3	Typical YSZ creep specimens.	17
4	Typical creep strain vs. time behavior for YSZ specimens.	18
5	Steady state creep rate data for [111] YSZ.	20
6	Steady state creep rate data for [110] YSZ.	21
7	Steady state creep rate data for [100] YSZ.	22
8	Surface features on undeformed YSZ creep specimens. Continued - Surface features on a deformed and etched [111] YSZ creep specimen.	24 25
9	Comparison of YSZ high temperature creep data with lower temperature constant strain rate deformation data from Ref. 4.	27
10	Transmission optical micrograph of a polished ThO ₂ specimen.	29
11	Typical creep strain vs. time behavior of ThO ₂ specimens.	30
12	Steady state creep rate data for [100] ThO ₂ .	33
13	Steady state creep rate data for [110] ThO ₂ .	34
14	Comparison of the creep behavior of single crystal and polycrystalline ThO ₂ .	35
15	Transmission optical micrograph of a partially polished Sc ₂ O ₃ crystal from Batch 1.	37
16	As-received Sc ₂ O ₃ crystals from Batch 2.	38

LIST OF ILLUSTRATIONS (Cont'd.)

Figure		Page
17	Transmission optical micrograph of a partially polished Sc_2O_3 crystal from Batch 2.	39
18	Typical YAG creep specimens.	40
19	Typical creep strain vs. time behavior for YAG specimens.	42
20	Steady state creep rate data for [100] YAG.	44
21	Steady state creep rate data for [110] YAG.	45
22	Steady state creep rate data for [111] YAG.	46
23	Surface features on YAG creep specimens.	48
24	Surface features on YAG creep specimens.	49
25	Steady state creep rate data for $[\bar{1}\bar{1}01]$ BeO.	52
26	Steady state creep rate data for $[\bar{1}\bar{1}00]$ BeO.	54
27	Micrograph of $[\bar{1}\bar{1}00]$ BeO creep specimens.	55
28	Reflected light micrographs of a twinned Al_2O_3 creep specimen.	57
29	Steady state creep rate data for [0001] Al_2O_3 .	60
30	Comparison of [0001] Al_2O_3 creep data at 200 MPa from the present study with previous deformation data.	61
31	Steady state creep rate data for 45° SiC.	64
32	Steady state creep rate data for [0001] SiC.	65
33	Surfaces of a tested 45° SiC specimen.	66
34	Surface of [0001] SiC creep specimen.	67
35	Creep data for several forms of SiC at 200 MPa.	69

LIST OF ILLUSTRATIONS (Concluded)

Figure		Page
36	Creep rates for several single crystal oxides at 100 MPa.	70
37	Creep rates at 100 MPa for several single crystal oxides as a function of inverse homologous temperature.	74
38	Bulk diffusivities for the slower moving species in a number of oxides.	76
39	Flow stress at a deformation rate of 10^{-5} /sec for various orientations of BeO, Al ₂ O ₃ and SiC.	77

LIST OF TABLES

		Page
Table 1	Some High melting Oxides with Potential as Ceramic Matrix Composite Reinforcements	3
Table 2	Calculated Schmid Factors for the Materials Tested Based on Applied Stress Directions and Proposed Slip Systems	11
Table 3	Values of G_0 and δG Used for Estimating High Temperature Shear Moduli	13
Table 4	Results of Trace Impurity Analysis by Neutron Activation	14,15
Table 5	Steady-State Creep Data for Yttria-Stabilized Zirconia Single Crystals	19
Table 6	Steady-State Creep Data for Thoria Single Crystals	32
Table 7	Steady-State Creep Data for Yttrium Aluminum Garnet Single Crystals	43
Table 8	Steady State Creep Data for Beryllia Single Crystals	51
Table 9	Steady State Creep Rate Data for C-Axis Sapphire	59
Table 10	Steady State Creep Data for Silicon Carbide Single Crystal	63
Table 11	Values of A, n, and Q Determined from Regression Fitting of the Creep Data to Equation (6)	72
Table 12	Estimated Temperature and Stress Limitations for an Allowable Creep Rate of 10^{-8} /sec.	73
Table 13	Shear Moduli and Burger's Vectors for Several Cubic Oxides	80

1. INTRODUCTION

Major improvements in the performance of gas turbine engines for propulsion applications will require the utilization of new, higher temperature, lower density structural materials. Ceramic-based materials offer several key advantages for such applications, namely high refractoriness, low density and freedom from dependence on strategic ingredients. Unfortunately, ceramics also have low fracture toughness, resulting in a strong dependence of strength on microstructural and surface defects and typically brittle failure. One promising method of providing for increased fracture toughness is to incorporate the ceramics as engineered composite structures. In such systems, the reinforcement (most appropriately a continuous fiber) performs several functions, such as stiffening of the composite and increasing the matrix strain to failure. The most important role of the fiber is to provide crack bridging and increased work of fracture via matrix-fiber debonding and fiber pullout. It is therefore clear that composite performance is directly dependent on the integrity of the reinforcing fiber.

The IHPTET initiative has sought to identify and ultimately develop structural composites for use in the temperature range 1650° to 2200°C (3000° to 4000°F) under oxidizing conditions. Unfortunately, there are no currently acceptable reinforcement fibers for use under these conditions. Current ceramic fibers all show severe strength degradation and excessive creep at temperatures well below 1650°C. Only carbon fiber maintains adequate mechanical behavior; however, carbon fiber suffers from susceptibility to oxidation and displays a very low axial thermal expansion, making it very difficult to provide for a thermomechanical match between the fiber and matrix. It is thus necessary to develop a new, oxidation resistant fiber for use above 1650°C.

Selection of appropriate materials for fiber development is a difficult task. Clearly, oxidation considerations play an important role, and materials inherently stable with regard to oxidation, such as oxides, are preferred. Also because of oxidation considerations, the matrices of ultra-high temperature composites will most likely need to be oxides. Providing for a proper thermal expansion match to an oxide matrix would generally be easier with an oxide fiber. Luckily, many refractory, phase stable oxides are known; however, the creep behavior of oxides is justifiably suspect. Polycrystalline oxides are known to readily creep at temperatures below 1650°C via diffusional and grain boundary sliding mechanisms, or by flow of viscous grain boundary phases. Fortunately these mechanisms do not come into play in single crystal materials.

Thus oxide single crystals represent a very attractive class of materials for fiber development. However, the creep behavior of oxide single crystals via dislocation glide and climb mechanisms is not well understood. In the literature, creep studies have been done on only a small number of materials, providing an insufficient data base for a priori identification of creep resistant oxides. This study was therefore undertaken in order to generate creep data on several interesting materials and to provide insight into the selection of other creep resistant single crystal oxides.

1.1. Material Selection

The appropriate selection criteria for high-temperature structural materials have been discussed previously by Hillig(1), and so will not be discussed in detail here. Many of the properties of ceramic materials are found to degrade as a function of homologous temperature (temperature divided by melting point). Thus to maintain these properties at high temperatures, a material with as high a melting point as possible would be desired. A list of high melting point oxides is given in Table 1. It is interesting to note that these oxides fall into a relatively small number of structural types. It would therefore be desirable to obtain creep data on a candidate material from each structure type in order to identify the most promising families.

The most refractory oxides are those with the fluorite structure; however, few are legitimate reinforcement candidates. The stoichiometries of UO_2 and CeO_2 vary extensively with temperature and oxygen partial pressure, with UO_2 oxidizing completely to U_3O_8 above 600°C in air. The very high density and radioactivity of ThO_2 would make it inappropriate as a reinforcement; nevertheless, it is still a scientifically interesting material simply because it is the highest melting oxide known. HfO_2 and ZrO_2 undergo two phase transformations between room temperature and their melting points unless they are stabilized by an alkaline earth oxide or rare earth oxide additive. For ultra-high temperature applications Y_2O_3 is generally the stabilizer of choice. Although pure HfO_2 has a higher melting point than pure ZrO_2 , once stabilized the differences are much less. Also, ZrO_2 has a much lower density and is much less expensive than HfO_2 . Previous deformation experiments have been done on yttria-stabilized zirconia (YSZ) at temperatures lower than those of interest for this study(2-4). This would suggest that fully-stabilized zirconia would be very susceptible to creep deformation at temperatures above 1650°C . Nevertheless both ThO_2 and YSZ were included in this study: thoria because of its very high melting point, and YSZ to provide a basis of comparison within a single structure type. It was also desirable to have a readily available, cheap material, such as YSZ, in the test matrix to allow for validation of the creep measuring apparatus and identification of any experimental problems prior to testing other, more expensive and rarer materials.

The rocksalt structure oxides are not attractive candidates despite their high melting points. In addition to reaction problems with atmospheric CO_2 and H_2O at low temperatures, single crystal MgO and CaO have both been shown to have poor resistance to high temperature deformation(5,6). Also, since hardness values decrease in the series $\text{MgO} > \text{CaO} > \text{SrO} > \text{BaO}$ (5), deformation resistance of SrO and BaO is not expected to be better.

Beryllium oxide is the only wurtzite structure oxide of interest for structural applications. BeO does have problems with reactivity toward H_2O at high temperatures and toxicity; however, these problems can be minimized by having the BeO encapsulated in a dense composite matrix. Beryllia does undergo a hexagonal to tetragonal phase transformation at 2050°C (5), but this is a high enough temperature that it would still be useful over most of the temperature range of interest. Moreover, beryllia's low density and high thermal conductivity make it a very attractive reinforcement candidate, and it was therefore included in this study.

Table 1. Some High Melting Temperature Oxides With Potential to be Ceramic Matrix Composite Reinforcements

Oxide	Melting Point (°C)	Structure	Density (g/cc)
ThO ₂	3220	Fluorite (cubic)	9.86
HfO ₂	2845	Fluorite (cubic)*	9.68
UO ₂	2840	Fluorite (cubic)	10.96
ZrO ₂	2765	Fluorite (cubic)*	5.83
CeO ₂	2610	Fluorite (cubic)	7.13
BeO	2570	Wurtzite (hexagonal)	3.01
MgO	2800	Rocksalt (cubic)	3.58
CaO	2610	Rocksalt (cubic)	3.32
SrO	2455	Rocksalt (cubic)	4.70
BaO	1920	Rocksalt (cubic)	5.72
Sc ₂ O ₃	2480	C-type R ₂ O ₃ (cubic)	3.84
Y ₂ O ₃	2420	C-type R ₂ O ₃ (cubic)	5.03
SrZrO ₃	2806	Perovskite (orthorhombic)	5.48
BaZrO ₃	2650	Perovskite (cubic)	6.26
LaCrO ₃	2510	Perovskite (orthorhombic)	6.69
CaZrO ₃	2345	Perovskite (monoclinic)	4.76
LaAlO ₃	2100	Perovskite (rhombohedral)	
Cr ₂ O ₃	2270	Corundum (hexagonal)	5.21
Al ₂ O ₃	2040	Corundum (hexagonal)	3.96
MgCr ₂ O ₄	2400	Spinel (cubic)	4.39
MgAl ₂ O ₄	2135	Spinel (cubic)	3.59
Y ₃ Al ₅ O ₁₂	1950	Garnet (cubic)	4.55

* Requires addition of a stabilizer, generally an alkaline earth oxide or rare earth oxide.

There are several rare earth sesquioxide compounds which could be included in Table 1, but only Y_2O_3 and Sc_2O_3 have been listed. This was done since the rare earth sesquioxides all have densities considerably higher than yttria without any significant advantage in terms of melting point or reactivity. Also, the rare earths lighter than H_o have phase transformations in the temperature range of interest (7) while that for yttria is above this range ($2280^\circ C$). Previous deformation data exist for Y_2O_3 single crystals which indicate they are susceptible to high temperature deformation (8). Thus scandia was selected for study to represent the c-type rare earth oxide materials; but, as will be discussed later, problems with material quality prevented creep measurements on Sc_2O_3 .

The perovskite-like oxides appear quite attractive based on melting points, but they suffer from several problems. First, most are distorted perovskite structures with several phase transformations between room temperature and their melting points. The alkaline earth zirconates (and corresponding hafnates) and rare earth chromates suffer from volatility of the alkaline earth and chromium atoms at high temperatures. Such volatility may not be a problem in a composite where the fibers are encapsulated in a dense matrix; however, in the creep tests used in this study the sample is completely exposed to the furnace atmosphere and specimen volatility would not be acceptable. As such, no adequate perovskite candidate material was identified for testing.

Next on the list are corundum and spinel structure oxides. Among these, chromium oxide and magnesium-chromate spinel again suffer from potential chromium volatility problems. However, the aluminum analogues of these materials, sapphire and magnesium-aluminate spinel, have been long recognized as attractive high-temperature materials. Consequently their single crystal deformation behavior has already been extensively studied, and it was not considered necessary to re-examine the creep behavior of these materials in detail. Because of the commercial availability of single crystal filaments, sapphire has been particularly well studied, and c-axis sapphire has become an unofficial standard by which the creep resistance of oxides is generally compared. Limited testing of c-axis sapphire was therefore included in this study in order to check the accuracy of the creep data being generated against that already in the literature.

The final structure group listed in Table 1 is the garnets, represented by yttrium aluminum garnet (YAG), $Y_3Al_5O_{12}$. Although not as high melting as most of the preceding materials, previous literature data on $Gd_3Ga_5O_{12}$ (8) indicate that garnets may be highly deformation resistant at temperatures very close to their melting points. Structural analysis conducted by L. Matson at WRDC/MLLM has suggested that YAG should be creep resistant due to the large number of atoms per unit cell, large lattice parameter, packing factor and complexity of the structure. These factors suggest the dislocation structure should form partials separated by complex stacking faults which hamper their motion. Creep studies of YAG were not included in the original proposal for this program, but, due to problems with scandia crystal quality, YAG was studied in place of scandia upon suggestion of the Air Force.

Although oxides were identified as the primary materials for evaluation in this study, many other classes of materials are being considered for ceramic composite reinforcement applications. One of the leading non-oxide candidate materials is SiC, which is attractive

because of its perceived creep resistance, among other attributes. It would therefore be advantageous to have creep data on single crystal SiC to provide for comparison with the oxide creep data. For this reason single crystal SiC was included in this study, though on a somewhat limited basis.

2. EXPERIMENTAL PROCEDURE

2.1. Material Sources

The materials used in this study were procured from a number of sources and came in a variety of sizes and degrees of perfection. Figure 1 shows typical samples of each material (except SiC) as-received.

The ThO₂, Sc₂O₃ and BeO crystals were all prepared using flux growth techniques, which make them susceptible to flux contamination or entrapment. The ThO₂ and Sc₂O₃ crystals were obtained from Clarendon Laboratory, University of Oxford, United Kingdom. Both sets were grown from PbO-V₂O₃ based fluxes(9), yielding small, colored crystals with significant numbers of internal defects. The beryllia crystals were obtained from Rockwell International, Autonetics Electronics Systems Division, Anaheim, California. These crystals were produced some years ago using a K₂MoO₄-MoO₃ flux(10), and were much larger, clearer and contained fewer defects than the ThO₂ or Sc₂O₃.

The YSZ, YAG and sapphire were all prepared from melts, and as such, were available as large, defect free crystals. The YSZ was obtained from Ceres Corporation, North Billerica, Massachusetts. According to the supplier, this material is a fully yttria-stabilized zirconia containing 9.5 mole% yttria. The crystals are grown using a skull-melting technique and are commonly sold as diamond simulants for jewelry(11,12). The YAG crystal was prepared by the Czochralski technique at Commercial Crystal Labs, Naples, Florida. The supplied crystal was taken from a 1 in. diam. boule of laser quality, though undoped, YAG. The Al₂O₃ crystal was obtained in the form of a 1/8 in. diam. rod from Saphikon, Inc., Milford, New Hampshire. This product is grown using the edge-defined, film-fed growth modification of the Czochralski process(13).

The SiC single crystal used in this work was an electronic grade, pure 6H polytype, alpha-SiC crystal prepared by Cree Research, Inc., Durham, North Carolina, using a proprietary process.

Samples of each material used for creep testing were analyzed for trace impurities using neutron activation analysis. This technique was utilized due to its high sensitivity for a large number of elements and its ability to utilize small samples. The ThO₂, due to the presence of fertile isotopes in natural Th, exhibited high background radiation levels following neutron irradiation, and thus could not be analyzed by this technique. The ThO₂ was instead analyzed

* Performed by Becquerel Labs., Inc., Mississauga, Ontario, Canada

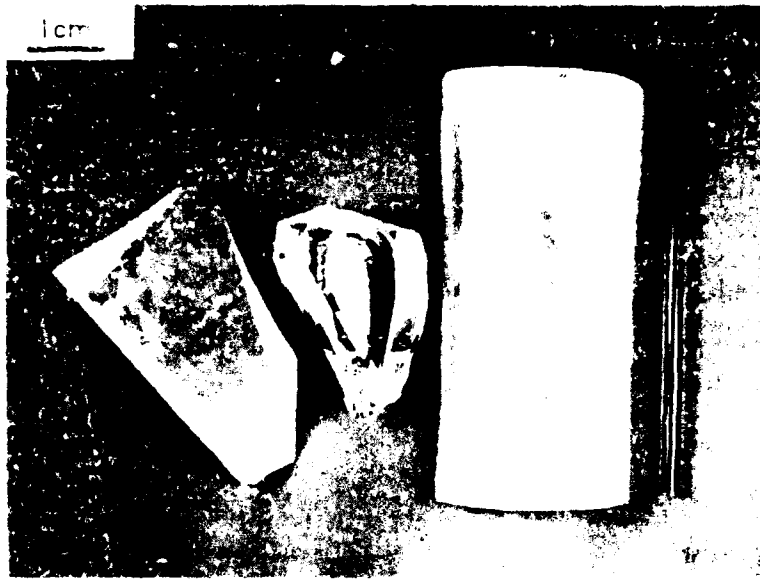


Figure 1. Typical as-received crystals:
Top, left to right: YSZ, BeO, YAG, Al₂O₃
Bottom, left to right: ThO₂, Sc₂O₃

using ICP emission spectroscopy; however, due to problems in digesting the sample, only data on a limited number of impurity metals was obtained. The SiC crystal, being of electronic grade purity, was not analyzed.

2.2. Specimen Preparation

All received single crystal materials were examined optically for indications of inclusions, porosity and/or cracking. The crystals were then aligned using standard Laue back-reflection X-ray diffraction analysis to within 2° of the desired crystallographic axis. Luckily, the ThO_2 and BeO crystals were well faceted such that X-ray alignment of each individual crystal was not necessary. Creep samples, in the shape of rectangular parallelepipeds of nominally square cross section, were then diamond abrasive machined from the aligned crystals. Grinding to final shape was done using a 600 mesh diamond abrasive wheel. Most samples were then polished using progressively finer grades of diamond polishing paste, finishing with 1 micron abrasive. Due to health concerns regarding the inhalation or ingestion of BeO dust, the sectioning of the BeO specimens was done at Ceradyne, Inc., Costa Mesa, California, and these specimens were not polished. All other sectioning and polishing was done at GE CRD.

The sizes of the prepared specimens depended on the size and shape of the starting crystal and the stress levels desired for creep testing. In all cases the aspect ratio of the creep specimens was 2.5 or larger in order to minimize end effects during deformation(14). Actual specimen sizes ranged from nominally 6.4 mm x 2.3 mm x 2.3 mm for some of the YSZ specimens to 2.3 mm x 0.9 mm x 0.9 mm for one of the ThO_2 samples.

The number of different crystallographic alignments studied varied for each material depending on crystal structure and size and number of crystals available. Creep specimens of the cubic materials YSZ and YAG were prepared with compression directions (the long axis of the samples) parallel to the [100], [110] and [111] crystallographic directions. The [100] aligned specimens had all {100} type faces, the [110] specimens had (110) end faces and (110) and (001) side faces, and the [111] specimens had (111) end faces and (110) and (112) side faces. Due to the small size of, and presence of defects in, the ThO_2 crystals, only [100] and [110] aligned specimens of ThO_2 were prepared. All of the hexagonal materials, BeO, Al_2O_3 and SiC, had samples prepared with axes parallel to the crystallographic c-axis, [0001]. In addition, BeO specimens with [1100] and [1101] (46.9° from the c-axis) alignments were prepared, as were SiC specimens at 45° to the c-axis. The alignments of several YSZ, YAG and BeO samples were checked following sample preparation, and all were found to be within 3° of the desired crystallographic direction.

2.3. Creep Testing

Uniaxial compressive creep measurements were made using a constant load arrangement. The apparatus consisted of a refractory metal hot zone, electrically heated, controlled atmosphere furnace[#] mounted in a small universal testing machine frame[†]. The testing machine

[#] Centorr Associates, Inc., Suncook, NH, Model M-60 equipped with the Physical Test Kit.

[†] Instron Corp., Canton, MA, Model TM-L.

was used to maintain furnace and loading rod alignment, and to gently lower and raise the weight pan. The loading rods were made of 2% thoria tungsten (1 inch diam. and 3/4 inch diam. for the lower and upper rod, respectively). The upper rod was connected to a water cooled brass fixture which extended outside the furnace through stainless steel bellows. The lower rod was fixed to the test machine frame. Proper alignment along with free vertical motion of the upper loading rod was accomplished using linear ball bearings mounted in the upper stationary and moving crossheads of the test machine. A photograph of the apparatus is shown in Figure 2.

Strain measurements were made using a linear variable differential transformer (lvdt)⁺ mounted to the upper loading rod in a small chamber above the main furnace chamber. The core of the lvdt was attached to a 1/8 inch diam. thoria tungsten rod which rested on the lower loading rod, thus making the lvdt body-core displacement the same as that of the upper and lower loading rods. The lvdt signal conditioner⁺ was run in a constant current mode which nullified any heating effects of the lvdt body. The lvdt signal was recorded over time using a PC-based data logging system. Effects of electrical noise and vibration from the furnace were minimized by simply averaging several readings. Overall resolution of the system was < 1 μm displacement (< .05% strain).

The creep experiments were normally carried out over a temperature range of 1650° to 1850°C, with applied stresses in the range of 12.5 to 400 MPa, depending on the material being tested. Temperature was measured using a sheathed W-5%Rh/W-26%Rh thermocouple placed within 1cm of the test crystal. Temperature control utilized the same thermocouple and a programmable controller⁺⁺, which maintained temperature within $\pm 2^\circ\text{C}$ during each test. The use of inert or reducing atmospheres during creep testing was necessary to protect the refractory metals in the furnace hot zone. The atmosphere used in most testing was high purity He, though testing of the YSZ and ThO₂ was done primarily in Ar-2%H₂. Repeat tests of the YSZ were done in both atmospheres with no noticeable differences in creep behavior.

Post-test characterization of the creep specimens was limited to optical and scanning electron microscopy. These were performed to look for evidence of slip bands or steps on the crystal surfaces by which the active slip planes might be identified. Due to the limited relief of the polished crystal surfaces very few features on the crept crystals were even detectable using SEM. For this reason most post-test characterization was done with reflected light microscopy using Nomarski interference contrast.

+ Schaevitz Engineering, Pennsauken, NJ, Model 050 MHR lvdt and Model ATA 101 signal conditioner.

++ Honeywell Industrial Controls Division, Fort Washington, PA, Model UDC 5000.

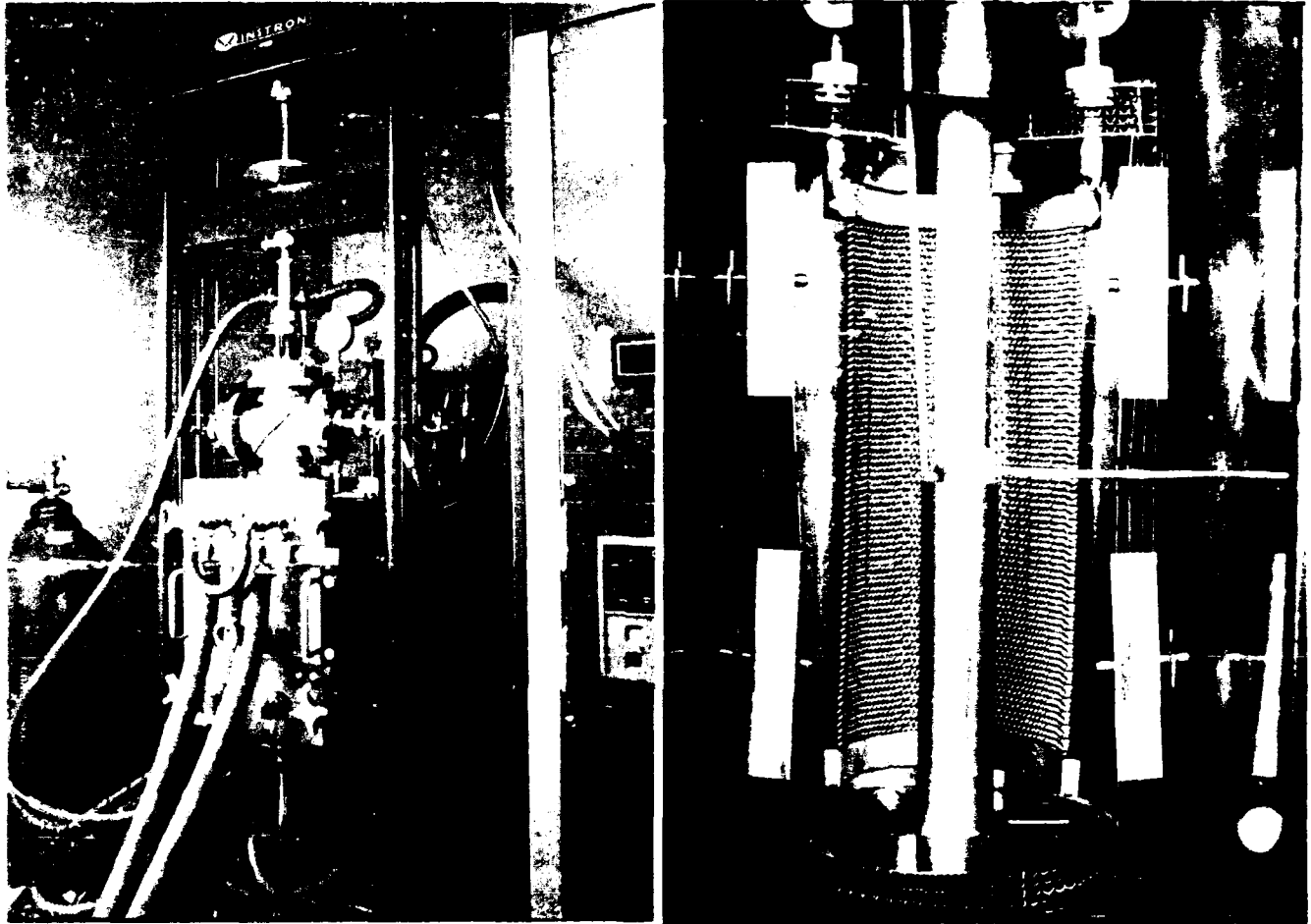


Figure 2. Photographs of creep measurement furnace:
Left: external view
Right: internal view

3. RESULTS

3.1. Data Fitting Procedure

The temperature and stress dependence of steady state creep of ceramic materials is often described using the general equation(15)

$$\dot{\epsilon} = (ADGb/kT) (b/d)^p (\sigma/G)^n \quad (1)$$

where $\dot{\epsilon}$ is the creep rate, A, p, and n are constants, D is the appropriate diffusion coefficient for the controlling mechanism, G is the shear modulus, b is the Burger's vector, d is the grain size, σ is the stress, and kT has its usual meaning. For single crystals the (b/d) term drops out. An activation volume term was not included in Equation (1) since none of the measured data displayed a significant dependence of creep activation energy on stress level.

As applied to deformation of single crystals, Equation (1) is generally interpreted as describing a slip mechanism which is limited by dislocation climb or other non-conservative dislocation motion, which is in turn limited by diffusion of one of the crystal components(15). As such, the main stress of interest is the shear stress on the active slip system, τ . This can be determined from the applied stress, σ , using the Schmid factor, S, as

$$\tau = S \sigma \quad (2)$$

Schmid factors calculated for the applied stress directions and proposed slip systems in each material tested are given in Table 2. However, since the active slip system could not be determined in many cases, the Schmid factor was not used in most data analysis. Rather the creep behavior was analyzed independently for each orientation using the applied stresses.

Of the terms in Equation (1), both D and G are temperature dependent. The temperature dependence of the diffusion coefficient can be written as

$$D = D_0 e^{-(Q/RT)} \quad (3)$$

where D_0 is a constant and Q is the activation energy for diffusion. The shear modulus at high temperatures is seldom known, but can be approximated(15) using

$$G = G_0 - \delta GT \quad (4)$$

where G_0 is the shear modulus at 0K, and δG is the rate of change of G with temperature, and T is the absolute temperature. Where available, values of G_0 and δG were estimated from literature data. Note that the values for δG were generally determined from data taken at temperatures much lower than those of interest in this study, and thus are only approximate. Also, the shear modulus of a crystal will typically be anisotropic, and will thus vary with direction in the crystal. However, temperature dependencies of crystal elastic constants were not generally available, so that crystal anisotropy was ignored. The values of G used were thus taken primarily from data on polycrystalline bodies, or were estimated by the average of

Table 2. Calculated Schmid Factors for the Materials Tested Based on Applied Stress Directions and Proposed Slip Systems

Material	Structure	Proposed Slip System	Schmid Factor for the Applied Stress Direction		
			[100]	[110]	[111]
YSZ or ThO ₂	Fluorite	{001} <110>	0	0.35	0.47
		{110} < $\bar{1}\bar{1}0$ >	0.50	0.25	0
		{111} < $\bar{1}\bar{1}0$ >	0.41	0.41	0.27
YAG	Garnet	{110} < $\bar{1}\bar{1}1$ >	0.41	0.41	0.27
		{110} < $\bar{1}\bar{1}0$ >	0.50	0.25	0
		{211} < $\bar{0}11$ >	0.29	0.43	0.38
		{211} < $\bar{1}\bar{1}1$ >	0.47	0.47	0.31
		{100} < $\bar{0}11$ >	0	0.35	0.47
		{100} < $\bar{0}10$ >	0	0.50	0.33
			[0001]	[$\bar{1}\bar{1}00$]	[$\bar{1}\bar{1}01$]
BeO	Wurtzite	(0001) < $\bar{1}\bar{1}20$ >	0	0	0.43
		{1010} < $\bar{1}\bar{1}20$ >	0	0.43	0.23
		{1010} [0001]	0	0	0.50
Al ₂ O ₃	Corundum	(0001) < $\bar{1}\bar{1}20$ >	0	-	-
		{1120} < $\bar{1}\bar{1}00$ >	0	-	-
		{1011} < $\bar{0}111$ >	0.26	-	-
SiC	6H (Wurtzite)	(0001) < $\bar{1}\bar{1}20$ >	0	-	0.50*
		{1010} < $\bar{1}\bar{1}20$ >	0	-	0.22*
		{1010} < $\bar{0}001$ >	0	-	0.43*

*Stress direction in SiC was 45° from the c-axis toward an a-axis.

the Hashin-Shtrikman upper and lower bounds(16) calculated from single crystal elastic constants. In the case of SiC the temperature dependence of G was calculated from the temperature dependence of the elastic modulus, E, using the equation

$$G = \frac{E}{2(1 + \nu)} \quad (5)$$

with a value of 0.18 for ν , the Poisson's ratio. The values of G_0 and δG used in the data analysis are listed in Table 3. It should be noted that the accuracy of the G values used is not critical, and that variance in the δG values has only a small influence on the calculated values for the creep activation energies.

Combining Equations (1), (3) and (4) above, and simplifying, gives the relation

$$\dot{\epsilon} = A' \left(\frac{G_0 - \delta GT}{T} \right) \left(\frac{\sigma}{G_0 - \delta GT} \right)^n e^{(-Q/RT)} \quad (6)$$

where A' is a constant and the other parameters are defined as above. In this equation, all parameters are known except for A' , n and Q . The values of n and Q will be referred to as the "stress exponent" and "creep activation energy," respectively, throughout the remainder of this report. Values for A' , n and Q were determined using a least squares multiple regression routine. Typically, independent regression analyses were performed for each stress direction in each material.

In the following sections much of the creep rate data will be presented graphically as plots of creep rate versus reciprocal temperature or stress. The points in these graphs represent the actual measured creep data whereas the lines are calculated from the regression fits of the creep data to Equation (6). The good agreement found between the measured creep data and the regression fits indicates qualitatively that Equation (6) adequately describes the creep behavior observed in this study.

It should be noted that the creep mechanism, and therefore the parameters in Equation (6), can depend on temperature, stress, strain, dislocation density, microstructure, etc. Using data from several specimens measured under a variety of conditions to evaluate these parameters is not, in general, valid. Ideally these parameters should be measured using differential stress or differential temperature tests on specimens with identical thermomechanical histories. However, in cases where the rates of recovery and work-hardening are identical, i.e., at high temperatures, low strain rates and under steady state conditions, correlations between different specimens are valid(26).

3.2. Yttria-Stabilized Zirconia

The chemical analysis results for the YSZ specimen are given in Table 4. Note that a large majority of the elements looked for were below detectability limits, which varied from element to element. The nominal composition of this material, according to the supplier, should be 9.5 mole% Y_2O_3 . Based on the measured ratio of yttrium to zirconium plus

Table 3 Values of G_0 and δG Used for Estimating High Temperature Shear Moduli.

Material	G_0 (GPa)	δG (MPa/K)	References
YSZ	64.5	18.6	17,18
ThO ₂	104.7	13.9	19,20
BeO	165.4	18.5	21
YAG	119.5	7.2	22,23
Al ₂ O ₃	170.0	24.3	24
SiC	197.0	40.3	25

**Table 4. Results of Trace Impurity Analysis
by Neutron Activation**

Element	Elemental Concentration (ppm by wt.) [*] for the Given Materials				
	YSZ	Sc ₂ O ₃	YAG	BeO	Al ₂ O ₃
aluminum	<500	<0.2%	22.8%	<0.1%	49.7%
antimony	1.5	<25	<1	0.3	<0.03
arsenic	<1.5	<110	<3.9	<0.2	<0.1
barium	<56	<520	<130	<130	<35
bromine	<1.3	<84	<4.9	<0.3	<0.2
cadmium	<42	<2.1%	<31	<2.4	<0.9
calcium	0.1%	<0.2%	<0.1%	<0.5%	<620
cerium	<13	<1100	<6.7	<3.1	<1
cesium	<0.9	<130	<0.7	<0.5	<0.1
chlorine	<50	<0.1%	<500	<100	<200
chromium	329	<0.9%	<6.4	<3.9	<1.1
cobalt	<0.4	<22	<0.5	<0.7	<0.2
copper	<14	<670	<36	<60	<8.7
dysprosium		<2.5	<0.8		<0.4
europium	<0.1	<3	<0.2	<0.2	<0.07
gallium	<4.1	<280	<9.1	<6.1	<2.1
germanium	<69	<0.16%	<330	<180	<260
gold	<0.02	<2.8	<0.03	<0.002	<0.001
hafnium	0.8%	<230	<0.6	<0.3	<0.4
holmium	<1.9		<5.1	<0.1	<0.1
indium	<0.008	1.9	<0.1	<0.05	<0.1
iodine	<10	<23	<4.3	<1.4	<3.6
iridium	<0.05	<8.2	0.69	<0.009	0.4
iron	0.1%	<24%	<31	<32	<7.6
lanthanum	<0.1	<71	<0.2	0.1	<0.02
lutetium	<0.5	<32	<0.2	<0.1	<0.03
magnesium	<220	<1.1%	0.17%	<880	<0.4%
manganese	<0.6	19	<3.7	<2.5	<2.7
mercury	<8.2			<1.3	
molybdenum	<18	<190	<75	30	<1
neodymium	<18		<18	<3.5	<1.9
nickel	<110	<6900	<110	<67	<18
niobium		<360	<120		<270
potassium	<380	<1%	<270	<300	<170

Table 4 (Concluded)

Element	Elemental Concentration (ppm by wt.) [*] for the Given Materials				
	YSZ	Sc ₂ O ₃	YAG	BeO	Al ₂ O ₃
preseodymium	<3.8			<3.7	
rubidium	<14	<1700	<15	<15	<3
samarium	<0.2	<2	<0.7	<0.01	<0.005
scandium	0.23	66.4%		<280	<0.02
selenium	<18	<420	<3.6	<2.8	<0.7
silver	<4.1	<1100	<2.5	<2.8	<0.4
sodium	9.3	<190	19	33	31
strontium	61	<1200	<230	<110	<34
tantalum	54	<34	<0.4	<0.6	<1.4
tellurium		<3300	<8		<1.5
terbium	<0.4		<0.3	<0.2	<0.06
thorium	<2.9	<53	<0.7	<0.4	<0.1
thulium	<1.7			0.68	
tin	<1300	<2.4%	<420	<240	<75
titanium	260	<1800	<370	<500	<290
tungsten	<1.6	<290	<6.3	<0.3	<0.2
uranium	<3.6	<48	<5.4	<0.3	<0.2
vanadium	<0.4	1.38%	<8.6	<2.1	<7.8
ytterbium	5.7	<380	<1.3	<0.07	<0.03
yttrium	11.1%	<5.8%	44.7%	<8300	<7300
zinc	<14	<2200	<15	<19	<3.4
zirconium	58.0%		<190	<120	<29

* Values followed by % are in atomic weight %. Where an element concentration was below detectability the concentrations are listed as less than the estimated detectability limit.

hafnium, the analyzed composition is approximately 8.9 mole% Y_2O_3 ; however, detectability of yttrium by this analysis technique is somewhat poor so that there may be significant error in the analyzed yttrium content.

Creep measurements for the YSZ specimens were carried out using applied stresses* of 12.5 to 100 MPa for the [110] and [111] alignments, and 25 to 100 MPa for the [100] alignment. Optical micrographs of typical creep specimens, both before and after testing, are shown in Figure 3. Some coloration of the specimens was observed after testing, which was independent of whether Ar-2% H_2 or He was used as the atmosphere. The darkening was minor, and could be easily reversed by short exposure to air at 800°C. Overall, the specimens exhibited little barrelling, but rather tended to display shear-like skew deformations. Because of this, sample cross sectional area remained relatively constant for low levels of strain (<6%), and thus the constant load tests approximated constant stress conditions.

In most cases each crystal specimen was utilized for more than one test, i.e., the temperature and/or stress was changed during the experiment. As long as a slight preload was maintained on the crystals during the change of conditions, little or no evidence was found for a primary creep regime. However, during the initial testing of a specimen, or if contact was not maintained during changes of test conditions, a short primary regime was sometimes observed. This suggests that any initial transient deformations observed in this system were due to "flattening" of the crystal/platen interface. Small (approximately 1 cm² by 3 mm thick) plates of [100] aligned YSZ were used as platens, with 12.5 μ m Mo foil used to separate the platens and crystal and prevent bonding. Minor indentation of the platens did occur, but was generally limited to the primary transient deformation mentioned above. Creep strains measured during the test were checked by measuring the total strain of the crystal following testing. The creep data was discarded if the strains did not match within 10%.

Typical plots of measured creep strain** (plotted as negative values since it is compressive) versus time are shown in Figure 4 for each sample orientation. In most cases, a linear dependence of strain with time was clearly indicated. Creep strains were found to remain linear with time for strains exceeding 10%, though creep rates were determined only on specimens with less than 6% total strain. Steady state creep rates were determined by linear regression fits to the linear parts of the strain versus time curves.

The measured steady state creep rates for [111], [110], and [100] YSZ are listed in Table 5 and shown graphically in Figures 5, 6, and 7, respectively. The first plot in each of these figures shows the temperature dependence of creep rate, the second plot shows the stress dependence. In general, the creep rates at a given stress and temperature varied with stress

* All stresses given are the applied, compressive stresses based on initial specimen cross section. No corrections were made for specimen shape changes or bending stresses caused by skew-type deformation.

** All strains given are true axial strains, measured from the reduction in length of the sample under test.

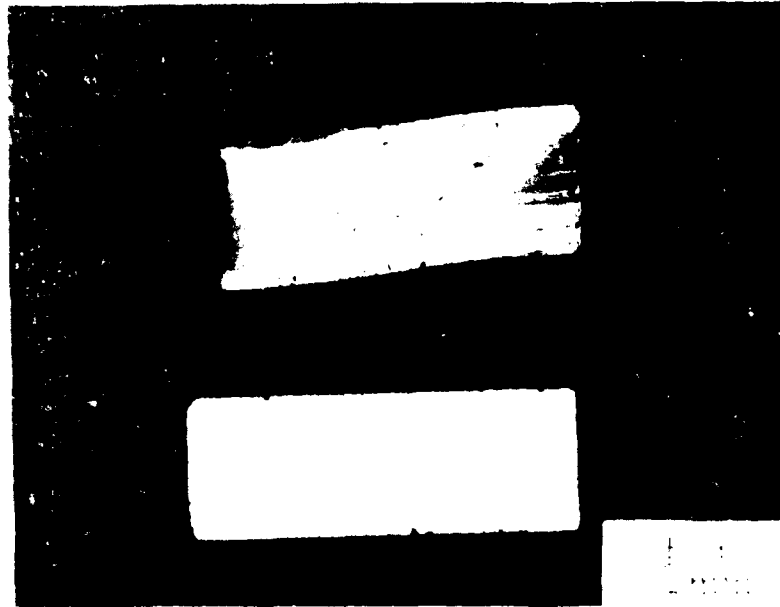


Figure 3. Typical YSZ creep specimens:
Bottom: as-polished
Top: after creep testing

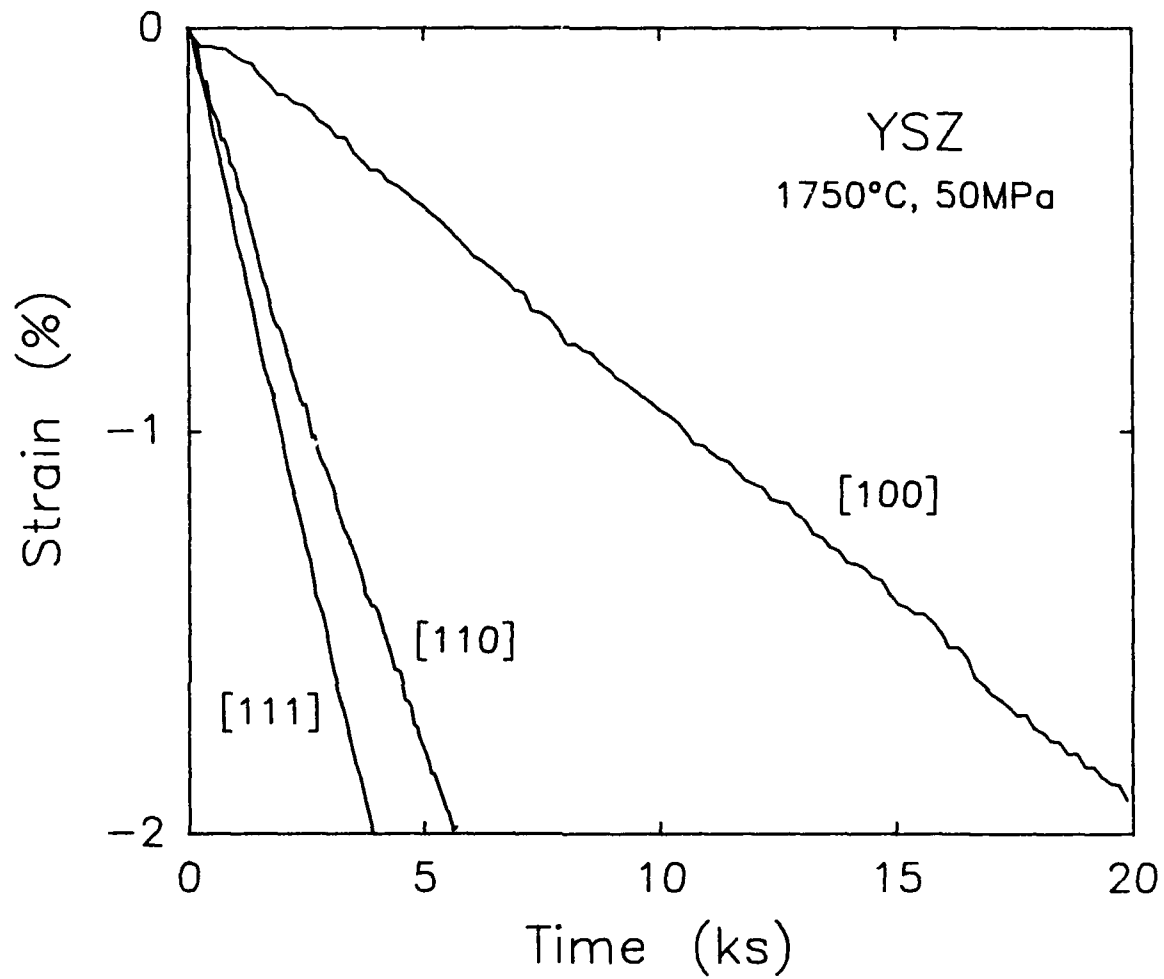


Figure 4. Typical creep strain vs. time behavior for YSZ specimens.

**Table 5. Steady-State Creep Data for Yttria-Stabilized Zirconia
Single Crystals**

Temperature (°C)	Stress (MPa)	Creep Rate (sec ⁻¹) for Given Stress Direction		
		[111]	[110]	[100]
1650	12.5	1.69x10 ⁻⁸	3.45x10 ⁻⁹	
	25	1.49x10 ⁻⁷	3.82x10 ⁻⁸	1.90x10 ⁻⁸
	50	8.47x10 ⁻⁷	6.37x10 ⁻⁷	1.73x10 ⁻⁷
	70			6.19x10 ⁻⁷
	100	3.22x10 ⁻⁵	1.51x10 ⁻⁵	1.25x10 ⁻⁵
	100			8.78x10 ⁻⁶
1750	12.5	4.30x10 ⁻⁸	8.94x10 ⁻⁹	
	25	3.92x10 ⁻⁷	1.46x10 ⁻⁷	1.07x10 ⁻⁷
	50	4.67x10 ⁻⁶	3.51x10 ⁻⁶	9.79x10 ⁻⁷
	70			4.42x10 ⁻⁶
	100	1.49x10 ⁻⁴	1.01x10 ⁻⁴	6.98x10 ⁻⁵
	100			6.05x10 ⁻⁵
1850	12.5	1.64x10 ⁻⁷	4.42x10 ⁻⁸	
	25	1.08x10 ⁻⁶	7.41x10 ⁻⁷	4.60x10 ⁻⁷
	50	2.08x10 ⁻⁵	1.34x10 ⁻⁵	5.49x10 ⁻⁶
	70			2.80x10 ⁻⁵
	100	8.82x10 ⁻⁴	8.00x10 ⁻⁴	4.60x10 ⁻⁴
	100			3.33x10 ⁻⁴

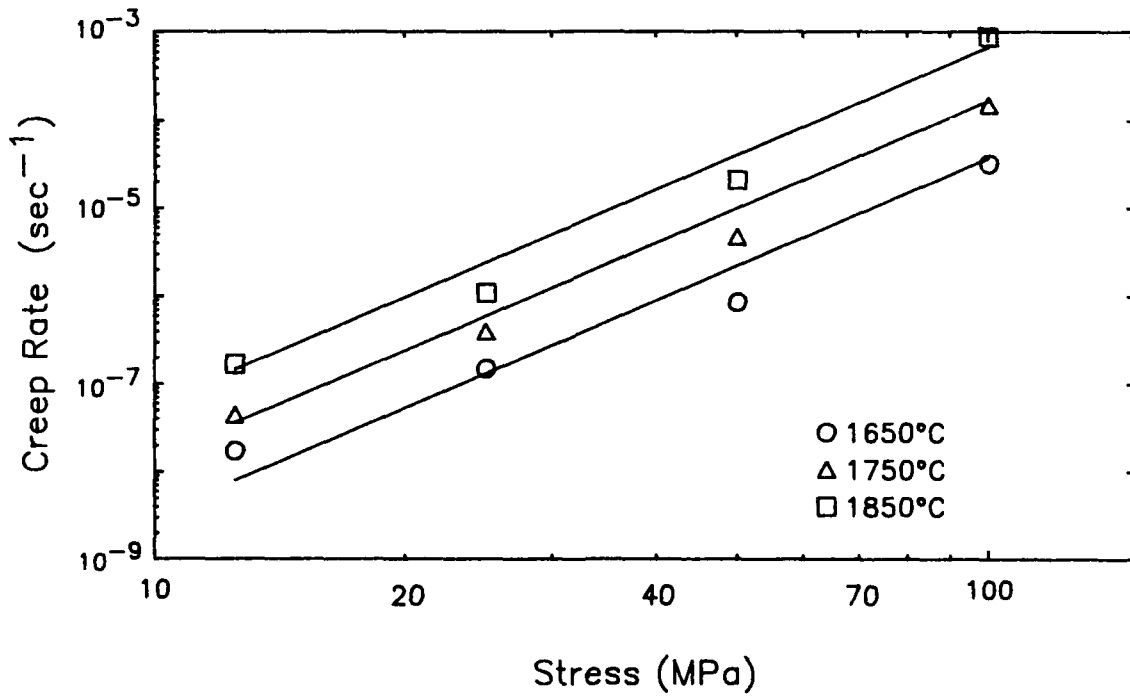
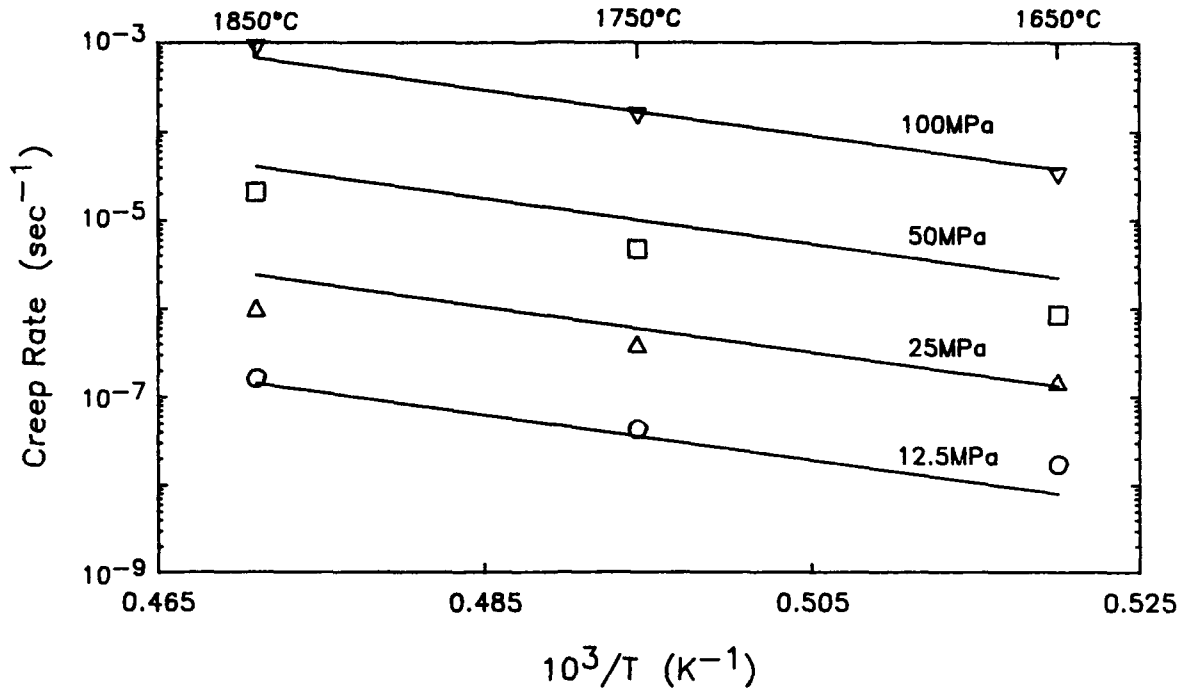


Figure 5. Steady state creep rate data for [111] YSZ.

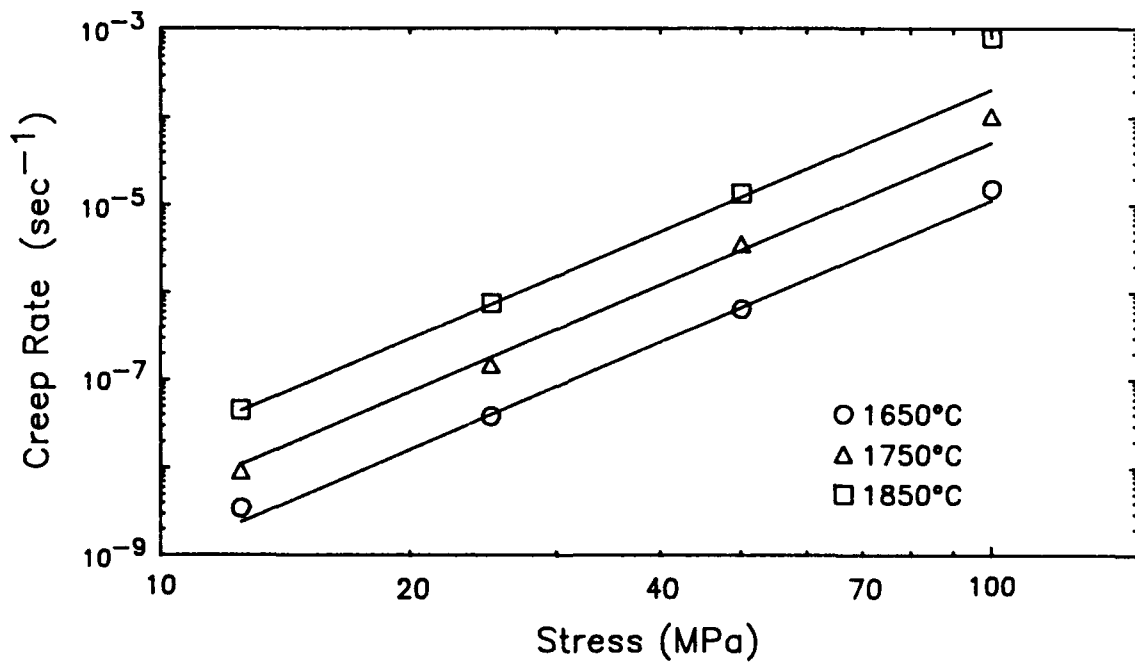
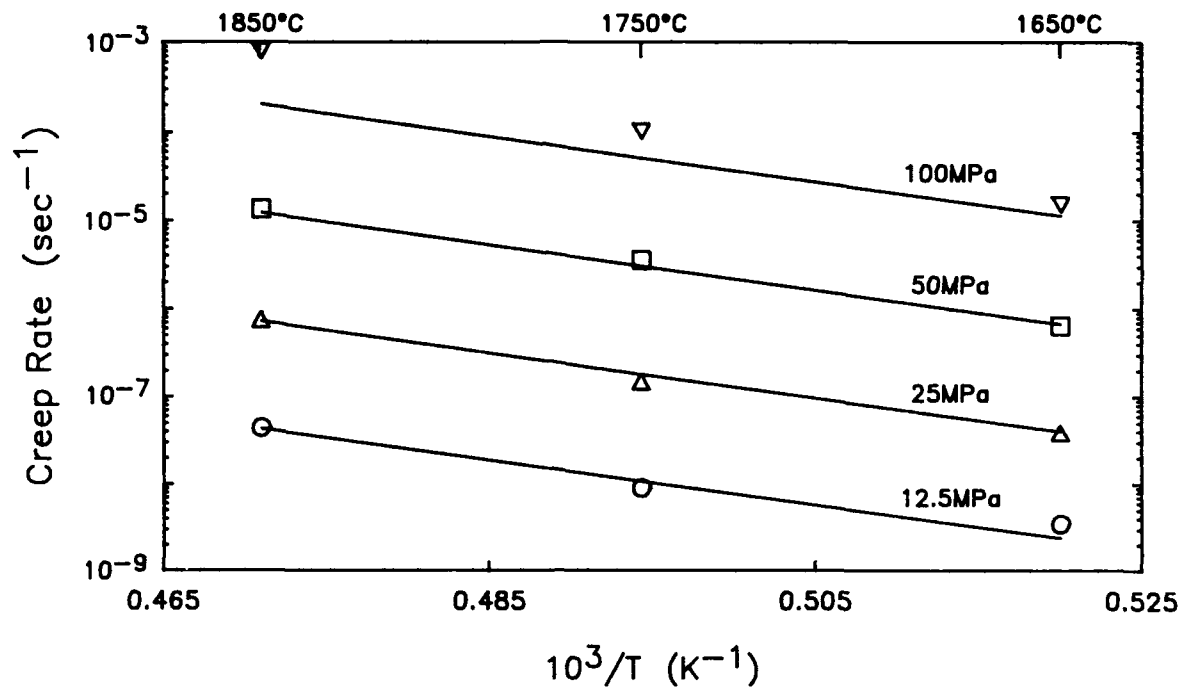


Figure 6. Steady state creep rate data for [110] YSZ

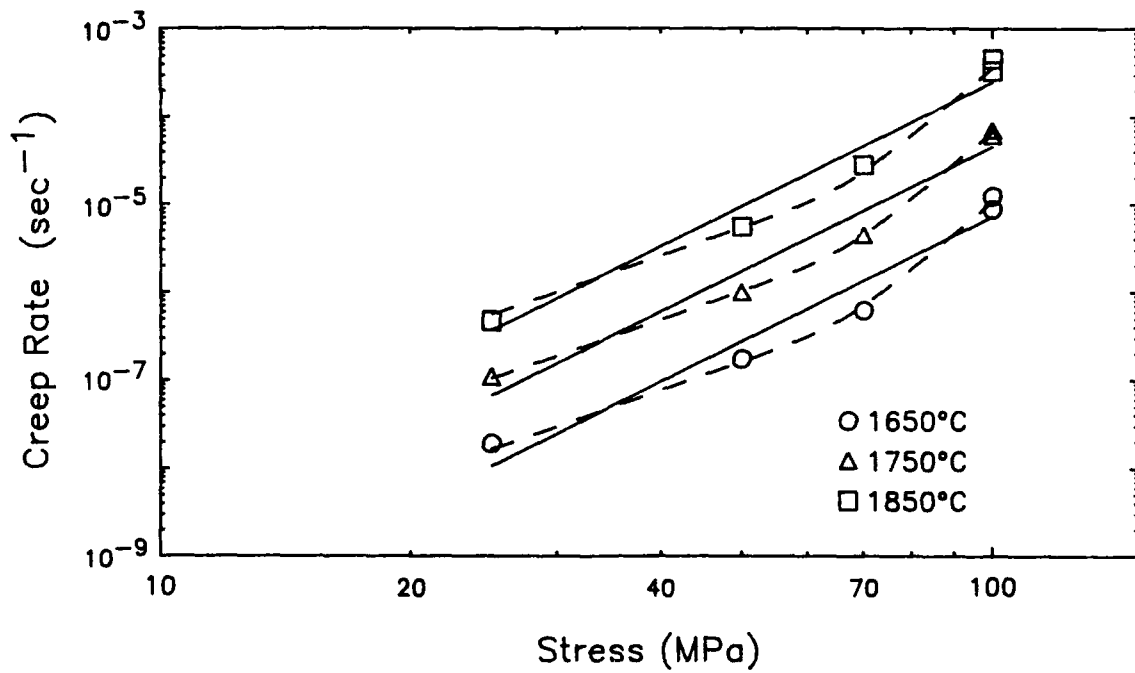
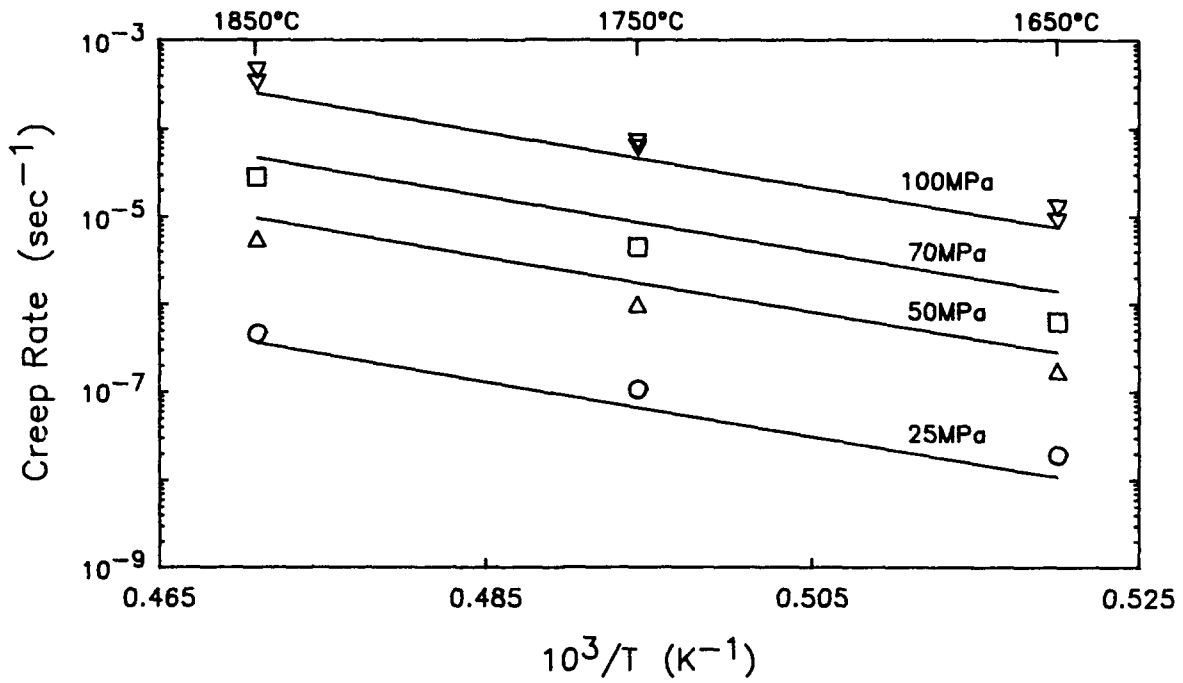


Figure 7. Steady state creep rate data for [100] YSZ

direction as $[111] > [110] > [100]$. Two separate sets of data were determined for the $[100]$ aligned crystals at 100 MPa, which confirm the repeatability of the measurements.

The creep data for the $[111]$ and $[110]$ aligned specimens were analyzed together, though separately from the $[100]$ samples. This was done since both the $[111]$ and $[110]$ alignments activate the $\{001\} < 110 >$ slip system, which is the easy slip system for cubic zirconia (2-4, 27), whereas the $[100]$ aligned specimens would not (see Table 2). The $[111]$ and $[110]$ data could therefore be combined using the proper Schmid factors to obtain the resolved stresses from the applied stresses. Multiple regression fitting of the creep data to Equation (6) yielded a stress exponent and activation energy of 4.07 ± 0.14 and 436 ± 46 kJ/mole, respectively, for creep of the $[111]$ and $[110]$ aligned crystals (the limits represent plus or minus one estimated standard deviation).

Creep data for the $[100]$ aligned specimens was also analyzed using Equation (6). The regression analysis gave estimated values of the stress exponent and activation energy of 4.73 ± 0.28 and 530 ± 61 kJ/mole, respectively. The difference in the stress exponents for the $[100]$ alignment versus the $[111]$ and $[110]$ alignments may be a result of the test matrix used. As can be seen in Figures 5 through 7, the strain rate versus stress plots tend to show a degree of upward curvature, particularly at high stresses. This was especially true for the $[100]$ specimens, where the data plotted in Figure 7 show a distinct non-exponential stress dependence (the solid lines are the result of the regression fit to Equation (6), the dashed lines show a second order exponential fit which more closely represents the data). Since measurements were not done at 12.5 MPa for the $[100]$ alignment, and since two sets of data were taken at 100 MPa, the high stress data points carry a greater relative influence for this alignment during the regression analysis. Removal of the 100 MPa data from all analyses limits the effects of the strain rate-stress nonlinearity on the regression fit, yielding estimated stress exponents of 3.61 for all YSZ creep data and leaving the activation energies relatively unchanged. This indicates that the stress exponents for all three alignments are the same at low stresses. The most likely reason for the nonlinearities in the strain rate versus stress data is the activation of duplex slip or secondary slip systems at the higher stresses.

Post-test examination of the samples using optical and scanning electron microscopies did not provide any evidence as to the active slip systems. No slip steps or bands were found on any YSZ crystal faces. Several crept specimens were treated in molten KOH at 500°C to try to form dislocation etch pits (27). Pitting of various morphologies was observed on several crystal faces, as shown in Figure 8. Micrographs A-C in Figure 8 indicate that surface damage caused by specimen preparation, including both surface scratches and subsurface damage revealed by etching, was effectively annealed out by exposure to 1650°C. Heated creep specimens should therefore have had few near-surface dislocations prior to testing. After testing, etch pits of varying morphology were observed on the different crystal faces, as shown in micrographs D-G of Figure 8. This suggests that the etch pits are indeed related to mobile dislocations generated during deformation. However, the etch pits were found to be essentially randomly distributed, with no noticed correlations of pit distribution with crystallographic direction. Active slip planes could therefore not be determined directly. Despite the lack of direct evidence, it is considered likely that the active slip system in the $[111]$ and $[110]$ aligned specimens is $\{001\} < 110 >$. This system has been previously observed in both yttria-



Figure 8. Surface features on undeformed YSZ creep specimens
A. as polished
B. polished and etched
C. polished, annealed and etched



Figure 8 Continued: Surface features on a deformed and etched [111] YSZ specimen:

D. (110) face E. (112) face F. (110) face G. (112) face
The [111] compression direction is shown by the arrows.

and calcia-stabilized zirconia single crystals (2-4, 27). The active slip system for the [100] aligned crystals is even less certain; however, previous studies (2-4) suggest the $\{111\} \langle 110 \rangle$ system.

Identification of the rate controlling mechanism for deformation is not possible without microstructural evidence. The measured stress exponents, 4.07 for the [111] and [110] aligned samples and 4.74 for the [100] aligned samples (or 3.61 for all alignments at low stresses), are lower than the values of between 8 and 9 previously measured for YSZ (2), though they fall within the range generally observed for dislocation creep mechanisms (16). The activation energy for the [111] and [110] alignments, 436kJ/mole, matches quite well the activation energies for cation diffusion in YSZ (423kJ/mole for yttrium and 391kJ/mole for zirconium (28)). This would suggest that the mechanism involves dislocation climb limited by cation diffusion. Previous studies (2,27), which examined deformed stabilized zirconia crystals using TEM, found significant evidence for dislocation climb. Unfortunately, so many different dislocation mechanism models have been derived (15, 29) which give similar values of the stress exponent and activation energies that determination of these quantities alone cannot identify the mechanism unambiguously.

It is not clear why the activation energy for the [100] aligned specimens, 530kJ/mole, should be higher than for the other alignments. However, a similar difference in activation energy with orientation has been previously observed for deformation of YSZ single crystals (4), though the activation energy values were higher than those determined here. It should also be noted that in previous studies on polycrystalline stabilized zirconias, where the deformation rates were also assumed to be controlled by cation diffusion, activation energy values of 535 to 570kJ/mole have been reported (30-32). Again, the reasons for the discrepancies between the creep and diffusion activation energies are not clear.

Even though the activation parameters differed from those previously measured for YSZ single crystals, the magnitudes of the creep rates are very consistent. Dominguez-Rodriguez and Heuer (4) used a constant strain rate technique to measure the deformation behavior of 9.4 mole% YSZ single crystals in air. Their flow stress data at a strain rate of 1.3×10^{-5} /sec is plotted in Figure 9 versus reciprocal temperature for both [111] and [100] stress directions. The stresses needed to produce this same strain rate at 1650, 1750 and 1850°C can be estimated from the regression fits to the creep data measured in this study. These estimated stresses are also plotted in Figure 9. The agreement between the lower temperature constant strain rate data and the high temperature creep data is quite good.

The slight darkening of the tested samples indicates that reducing atmosphere in the creep test furnace had an influence on the point defect concentrations in this material, which may have in turn influenced the measured creep behavior. Available literature data are contradictory on the influence of atmosphere on the creep behavior on stabilized zirconia. Early work by Seltzer and Talty(30) on 92% to 93% dense, polycrystalline YSZ indicated a significant influence of atmosphere, with creep rates being higher in air than under reducing conditions. More recent work by Dimos and Kohlstedt(31) on >99% dense YSZ indicates no dependence of creep rates on atmosphere for oxygen partial pressures from 2.5×10^{-8} to 1 atm. The fact that the creep rates from this study, which were measured in reducing (Ar-

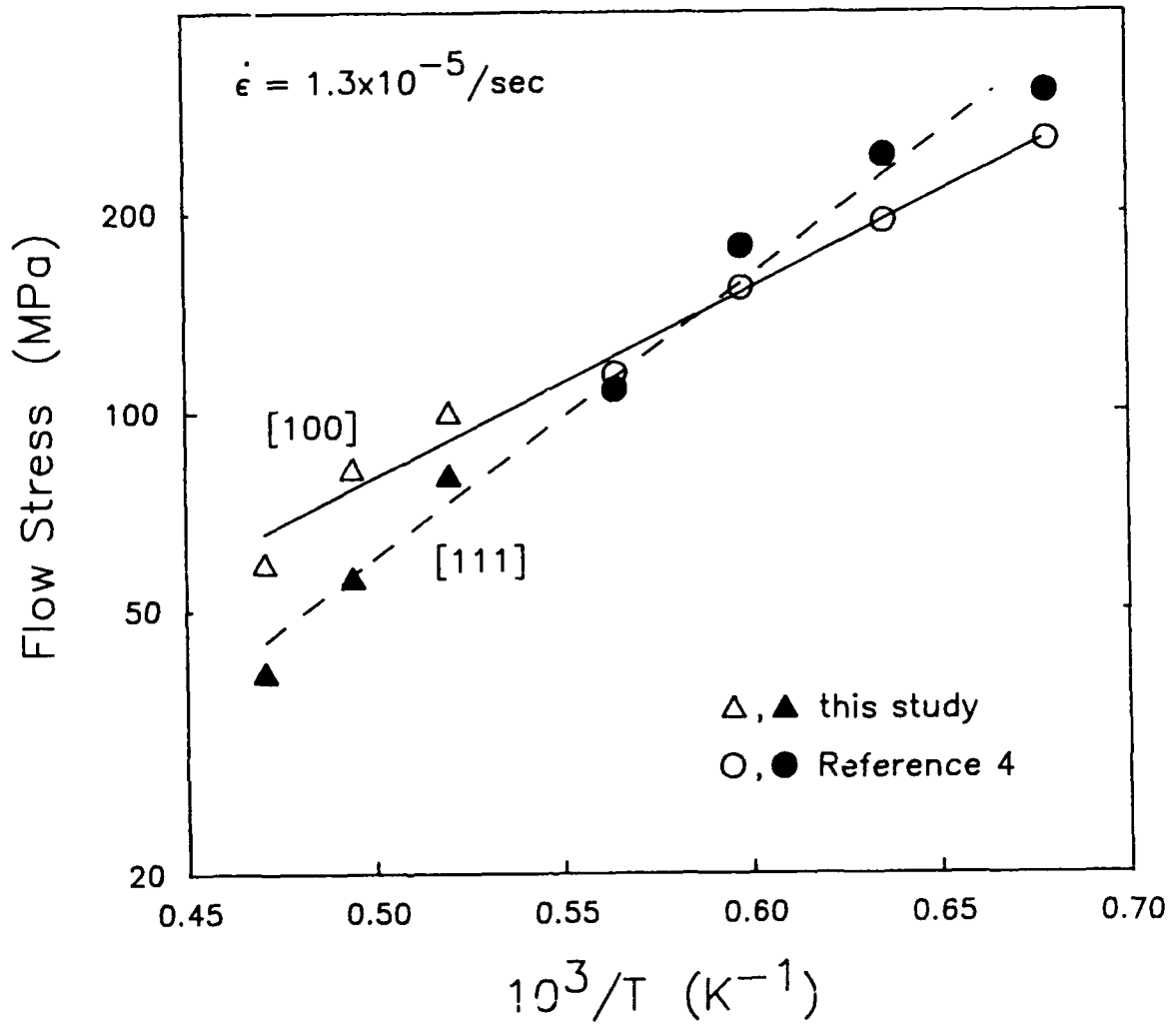


Figure 9. Comparison of YSZ high temperature creep data with lower temperature constant strain rate deformation data from Ref. 4.

2% H_2) and inert (He) atmospheres, agree with those observed by Dominguez-Rodriguez and Heuer(4), which were measured in air, suggest that atmosphere has no effect, in agreement with Dimos and Kohlstedt. The creep behavior of YSZ single crystals under oxidizing conditions should therefore be similar to that measured in this study.

3.3. Thoria

The thoria specimens could not be chemically analyzed using neutron activation analysis due to the activation of fertile isotopes in natural thorium and consequent high background radiation measurements. An attempt was also made to analyze a crystal using inductively coupled plasma emission spectroscopy, but again problems were encountered. First, it proved very difficult to get enough of a crystal into solution for analysis. Flux melting of a crystal with lithium tetraborate proved unsuccessful. One crystal was finally partially dissolved using a refluxed mixture of sulfuric and hydrofluoric acids. The use of HF acid, however, makes it impossible to quantitatively determine the presence of several elements due to possible etching of the Pyrex glassware and subsequent sample contamination. The analysis was further complicated in that thorium has a large number of emission lines which overlap many standard analysis lines for other elements. This necessitated the checking of multiple emission lines for a number of elements. As a consequence of these problems, the only elements of consequence detected were Pb (132 ppm) and V (23 ppm). These impurities are not surprising since the crystals were grown from a flux of mixed PbO and V_2O_5 . Other detected impurities, i.e., Si (10 ppm), Al (11 ppm), Na (69 ppm), and B (74 ppm), were probably contaminants from the Pyrex glassware.

As received, the ThO_2 crystals had a slight pinkish tint. Optical examination of the crystals indicated that they contained significant numbers of pores, inclusions and striations. As a consequence, some of the creep specimens contained such defects. Figure 10 shows a transmission optical micrograph of an undeformed ThO_2 specimen used for platen tests. This micrograph shows examples of the inclusions and striations (origin unknown) found in all of the as received crystals. Typical samples used for creep testing contained fewer and less severe defects than were present in this crystal. Following testing, the specimens all turned a very dark brown (almost black) color; however, as with the YSZ crystals, this color change could be reversed by annealing in air at 800°C.

Creep measurements were done using stresses in the range 50 to 100 MPa. Due to the shortage of good quality specimens, testing was done only on [100] and [110] aligned specimens, and only at three stress levels. Testing was done in Ar-2% H_2 atmosphere throughout. Plates of [100] YSZ were used as platens, with 12.5 mm thick Mo foil used to separate the ThO_2 samples from the YSZ platens. Despite the fact that ThO_2 proved to be more creep resistant than YSZ, little platen indentation was found.

A typical plot of strain versus time for a ThO_2 creep specimen is shown in Figure 11. As was found for the YSZ, a "primary creep" regime was generally observed only on initial testing of a crystal. Subsequent tests conducted after a change in stress or temperature showed no primary regime. As such, attainment of steady state creep was easily determined.



400 μm

Figure 10. Transmission optical micrograph of a polished ThO₂ specimen showing internal striations and inclusions.

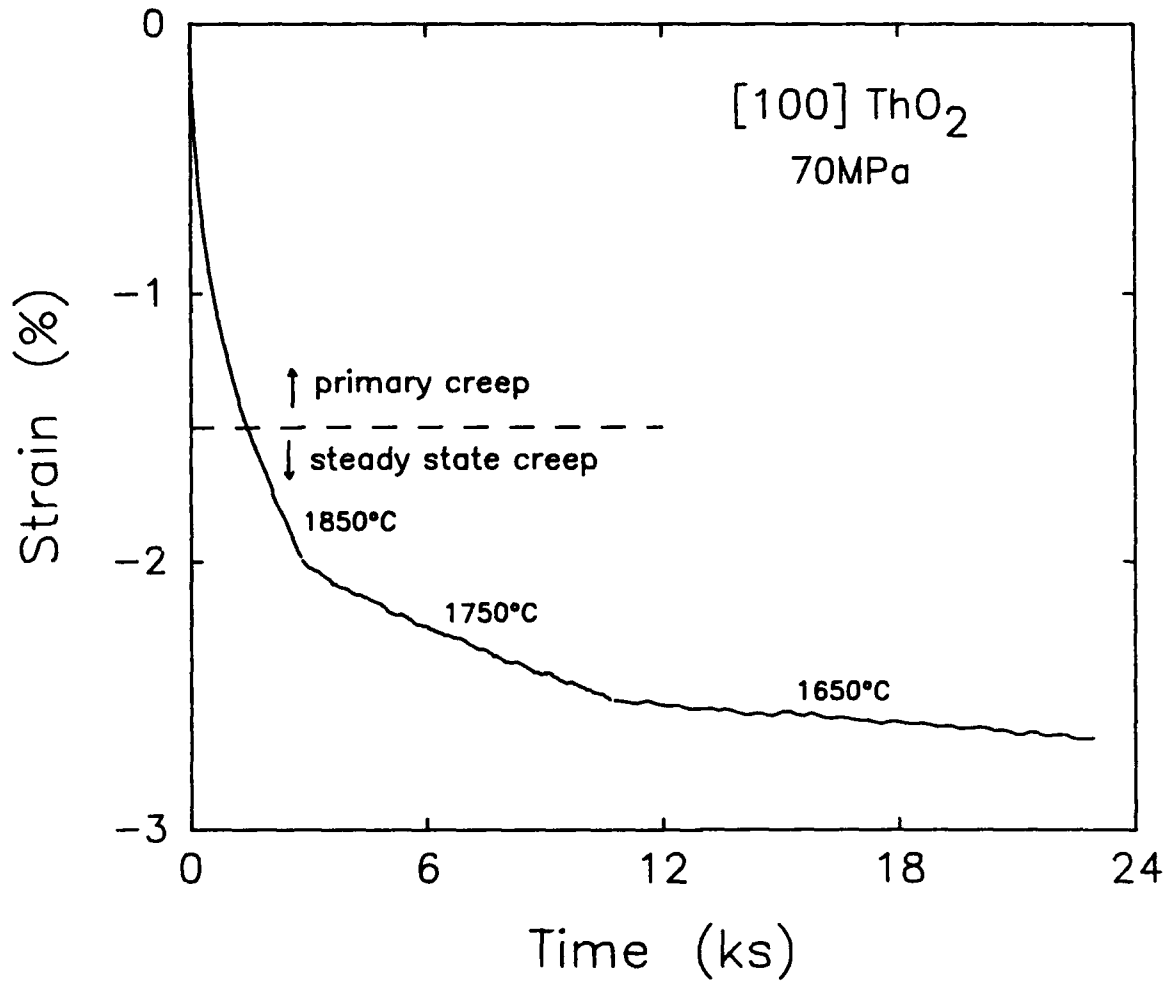


Figure 11. Typical creep strain vs. time behavior of ThO₂ specimens.

The measured steady state creep rates for [100] and [110] aligned ThO₂ are listed in Table 6 and shown graphically in Figures 12 and 13, respectively. Again, repeat measurements were made on [100] aligned crystals at 100 MPa to check the repeatability of the measurements. As can be seen, the agreement between these double measurements was very good. It should be noted that all [110] alignment measurements were made on a single sample. Very generalized conclusions based on the [110] alignment data are therefore not possible.

Regression analysis of the creep data from the two alignments was done separately. The measured creep data were fit to Equation (6) using the values of G_0 and δG given in Table 3. The determined values for the stress exponents and creep activation energies were 10.25 ± 0.35 and 473 ± 41 kJ/mole, respectively, for the [100] crystals, and 6.55 ± 0.16 and 591 ± 21 kJ/mole for the [110] crystal. The reasons for the large differences in stress exponents and activation energies between these two alignments are unclear. Both exponents are larger than the range generally associated with dislocation creep mechanisms (i.e. 3 to 6), but do fall within the range of exponents previously reported for deformation of oxide single crystals(15).

Also confusing is the fact that the activation energy for the [100] alignment is lower than that for the [110] alignment, which is opposite of that found for the YSZ data. Both activation energies are also much higher than those for oxygen self-diffusion in ThO₂ (209kJ/mole(33)). The activation energy for thorium self-diffusion in ThO₂ is somewhat controversial. Hawkins and Alcock(34) measured an activation energy of 246kJ/mole, whereas King(35) measured 626kJ/mole. The differences in these values were attributed to differences in measurement technique and data interpretation. King, using a precise sectioning technique, noted non-Gaussian tails on his diffusion profiles in ThO₂ single crystals, which he attributed to fast diffusion paths such as dislocations or sub-grain boundaries. Since King performed measurements on single crystals, and because he was able to detect and account for the influence of fast diffusion paths, his value of 626kJ/mole for Th diffusion is considered to be more accurate. It is therefore possible that the measured creep activation energies, which fall between the Th diffusion activation energies of King(35) and Hawkins and Alcock(34), are a result of combined volume and dislocation diffusion paths for Th. Alternately, the high level of Pb impurity may have a significant influence on Th diffusion, or may be directly controlling creep via some sort of impurity-dislocation association. In any case, the controlling mechanism for creep of these crystals is certainly not clear.

No previous creep data on single crystal ThO₂ could be found so that direct comparisons with previous research could not be done. Comparison of the present data with polycrystalline creep data, however, is somewhat instructive. Figure 14 shows creep data from the present study plotted with creep data on polycrystalline ThO₂(36). The polycrystalline ThO₂ was prepared by sintering, and had a density of 97.5% of theoretical and a grain size of ~ 10 μm . The plot shows that creep rates of the single crystals are roughly 1.5 to 2 orders of magnitude lower than for the sintered material at 50 MPa and comparable temperatures. This difference would decrease with increasing stress due to the high stress exponents of the single crystals; however, creep rates of the single crystals at 100 MPa are still comparable to the rates for the sintered ThO₂ at 50 MPa. This data clearly demonstrates the advantage in using

Table 6. Steady-State Creep Data for Thoria Single Crystals

Temperature (°C)	Stress (MPa)	Creep Rate (sec ⁻¹) for Given Stress Direction	
		[110]	[100]
1650	50	1.37x10 ⁻⁸	5.32x10 ⁻⁹
	70	1.05x10 ⁻⁷	1.11x10 ⁻⁷
	100	1.45x10 ⁻⁶	8.82x10 ⁻⁶
	100		7.94x10 ⁻⁶
1750	50	1.02x10 ⁻⁷	4.31x10 ⁻⁸
	70		5.82x10 ⁻⁷
	100	7.58x10 ⁻⁶	3.05x10 ⁻⁵
	100		5.93x10 ⁻⁵
1850	50	4.58x10 ⁻⁷	1.36x10 ⁻⁷
	70		3.55x10 ⁻⁶
	100	4.78x10 ⁻⁵	1.22x10 ⁻⁴
	100		1.23x10 ⁻⁴

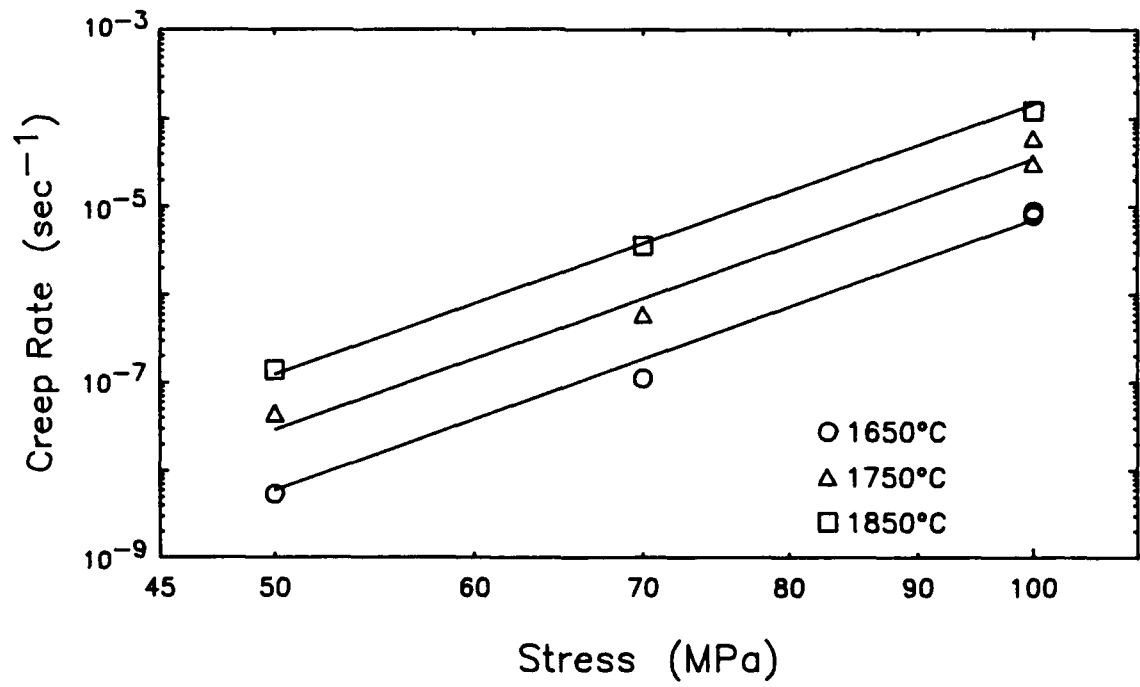
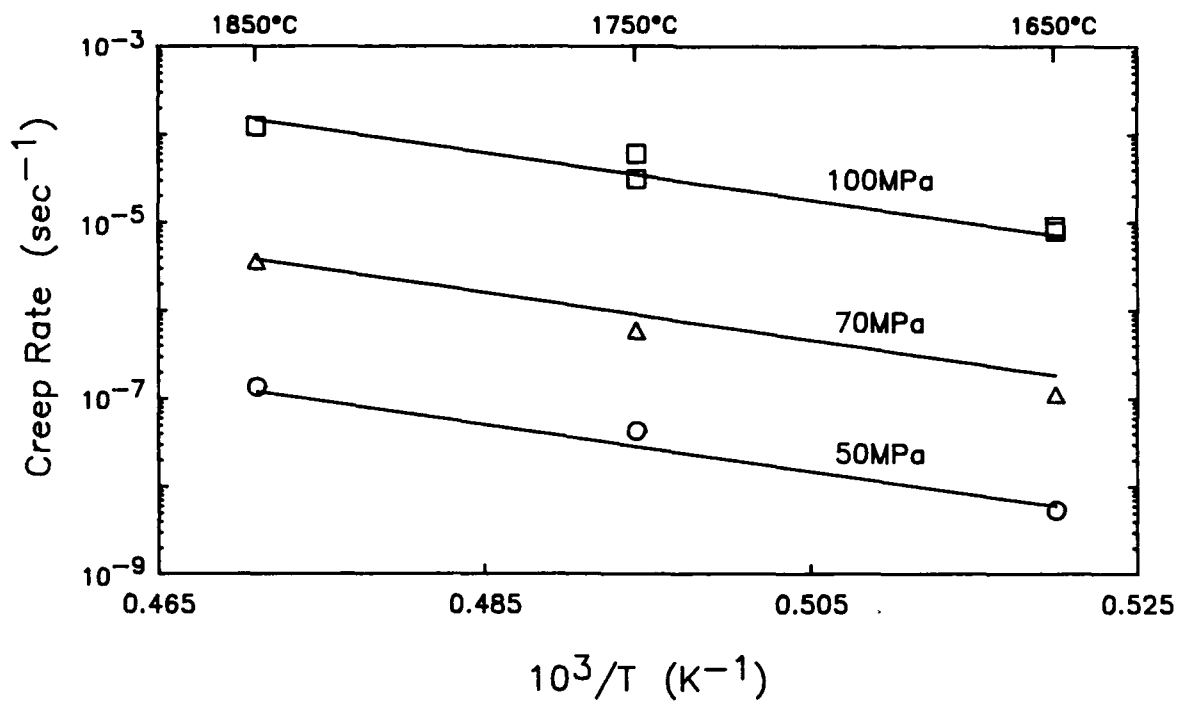


Figure 12. Steady state creep rate data for [100] ThO₂.

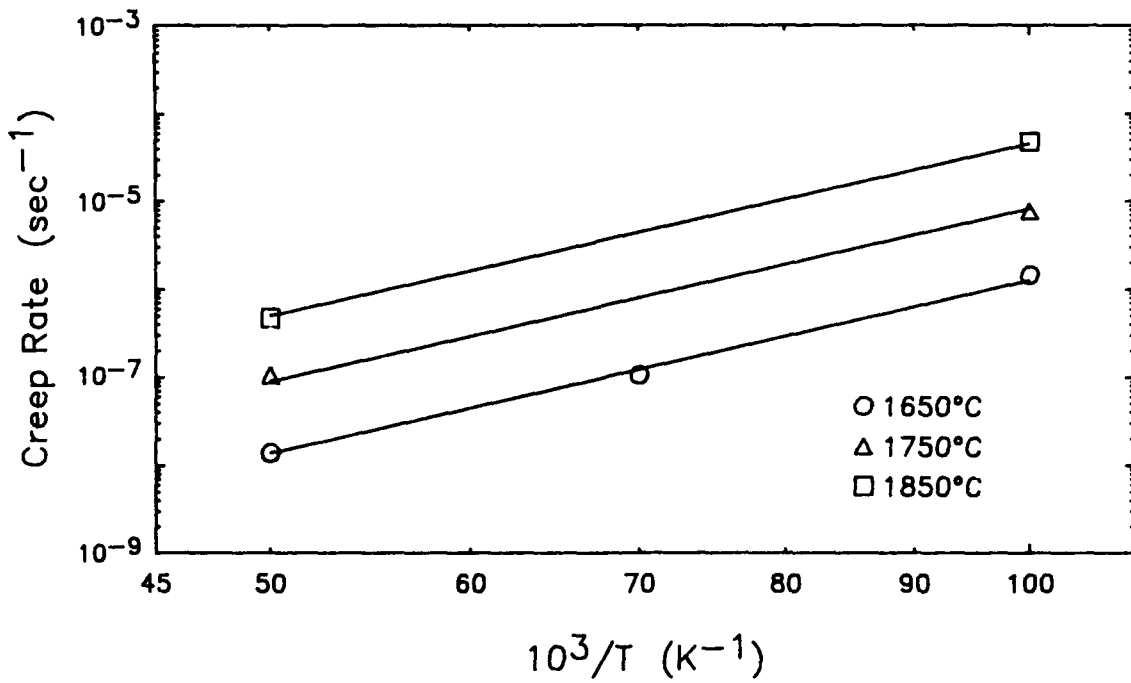
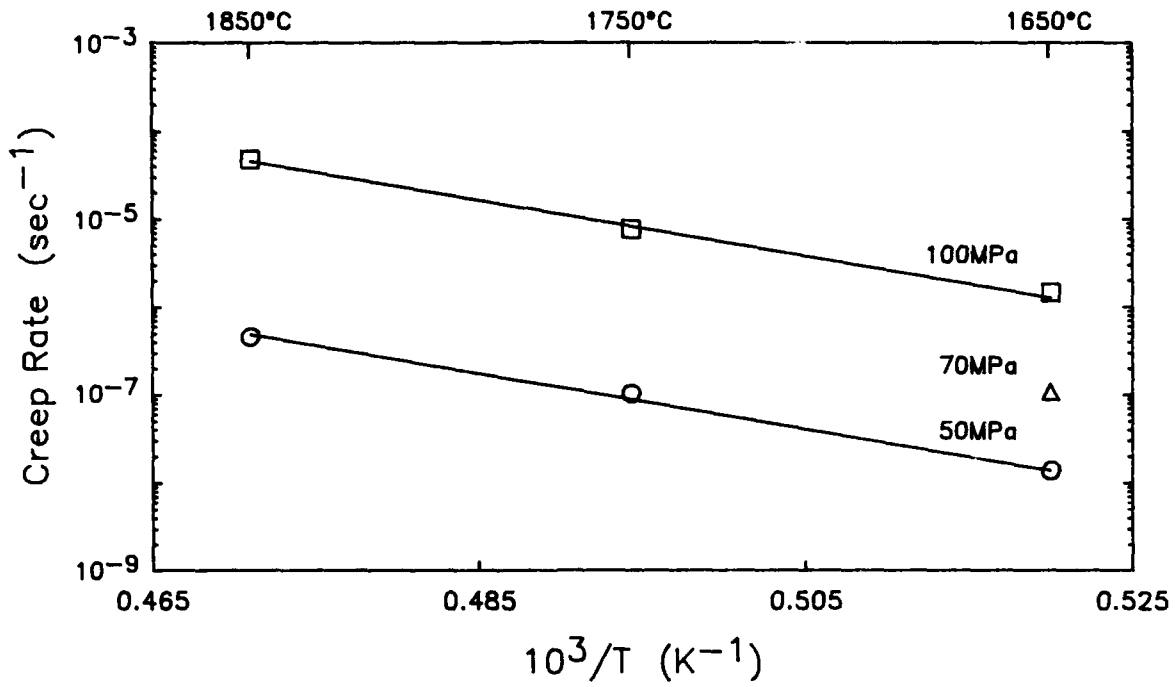


Figure 13. Steady state creep rate data for [110] ThO_2 .

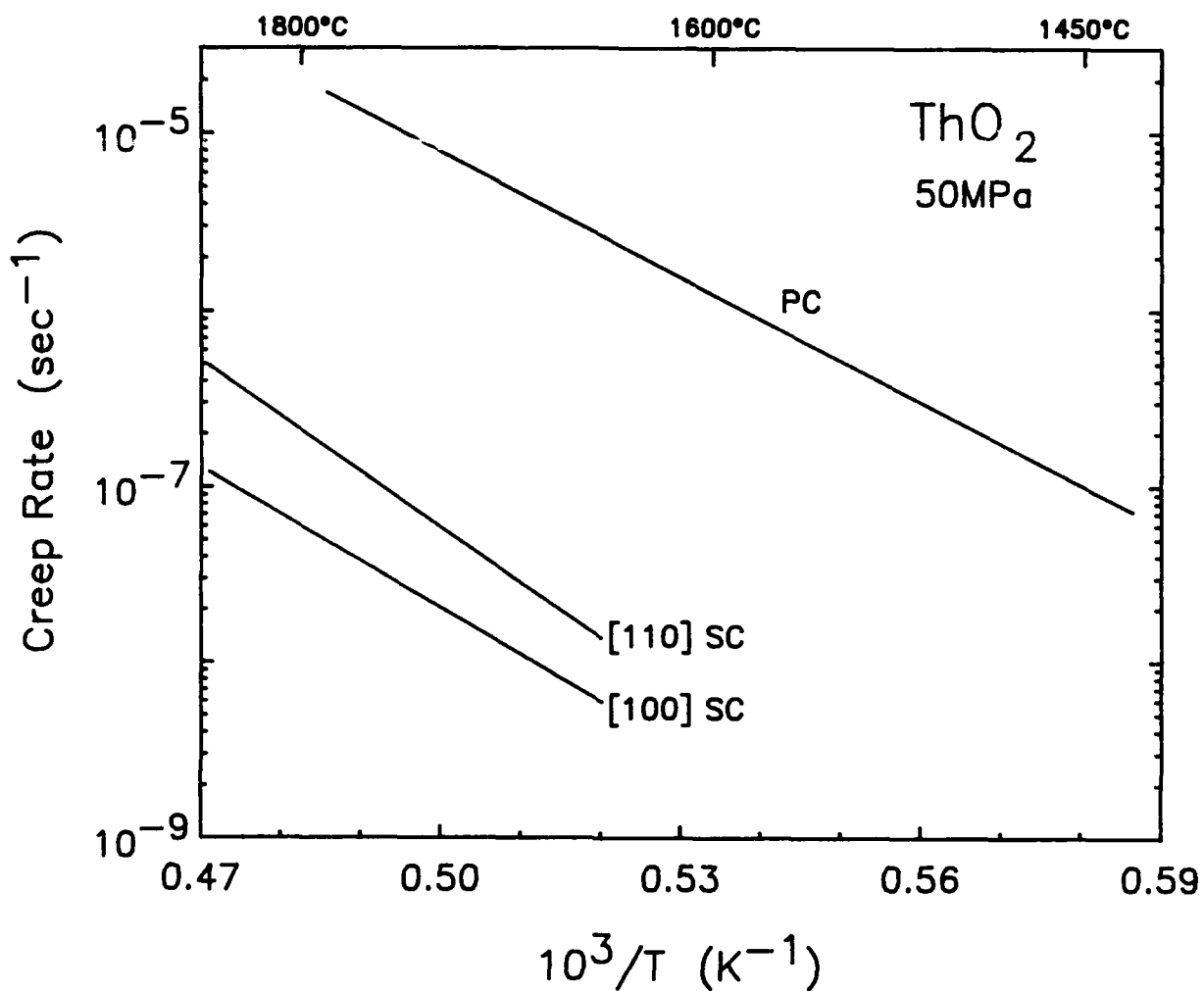


Figure 14. Comparison of the creep behavior of single crystal and polycrystalline ThO₂:
 SC- data on single crystals from this study
 PC- data on polycrystalline ThO₂ from ref. 36.

single crystal oxides as opposed to polycrystalline bodies for creep resistance.

3.4. Scandia

As noted earlier, the Sc_2O_3 crystals obtained were very small, strongly colored and poorly faceted. A sample crystal was chemically analyzed using neutron activation analysis, the results of which are given in Table 4. The major impurity detected was vanadium (1.38%), which helps explain the strong coloration. The presence of vanadium is not surprising since the crystals were grown in a flux containing V_2O_5 . Note that the estimated detectability limits for most elements were quite high. This was due to the small size of the scandia sample crystal.

Two crystals of the original batch obtained were X-ray aligned and polished. A transmitted light micrograph of a partially polished crystal is shown in Figure 15. This shows that, in addition to the small crystal size, there are a large number of internal pores, inclusions and striations (trapping of flux in some of the inclusions may help explain the high levels of V detected in the chemical analysis). As such, the crystals were determined to be unfit for creep testing.

At this point arrangements were made with Clarendon Laboratory personnel to attempt preparation of a new batch of Sc_2O_3 crystals on a best effort basis. Several crystal growth experiments were performed, including an attempt at seeded crystal growth. The resulting crystals are shown in Figure 16. Overall, the second batch of crystals were slightly larger, less strongly colored and had more well developed facets than those from the first batch. Two sample crystals from this batch were also aligned and partially polished in order to optically evaluate their quality. A transmission optical micrograph of one of the new crystals is shown in Figure 17. The newer crystals appeared to be free of many of the smaller pores and striations seen in the initial crystals, but still contained significant pores and inclusions. Some defect-free areas were observed, but they were of insufficient size to allow for creep specimen preparation. Creep testing of Sc_2O_3 was therefore dropped from the program.

3.5. Yttrium Aluminum Garnet

Neutron activation analysis results for the YAG material are given in Table 4. The only impurities which were above detectability limits were Mg (1700 ppm), Na (19 ppm) and Ir (0.7 ppm).

Creep measurements on YAG were all performed in a high purity He atmosphere. Applied stresses ranged from 100 to 280 MPa for [111] and [110] aligned specimens, with some experiments down to 50 MPa on the [100] specimens. Pieces of (111) aligned YAG plates, roughly 1 cm^2 by 3 mm thick, were used as platens. Only slight platen indentation was noted during testing. As before, specimen strains measured during testing were checked by measuring crystal dimensions after testing. If the measured and dimensional strains did not agree within 10% the creep data was discarded.

An optical micrograph of typical creep specimens, both before and after testing, is shown in Figure 18 (note that the YAG crystal was optically defect free; markings on the untested



200 μm

Figure 15. Transmission optical micrograph of a partially polished Sc₂O₃ crystal from Batch 1.



Figure 16. As-received Sc₂O₃ crystals from Batch 2.



200 μm

Figure 17. Transmission optical micrograph of a partially polished Sc_2O_3 crystal from Batch 2.

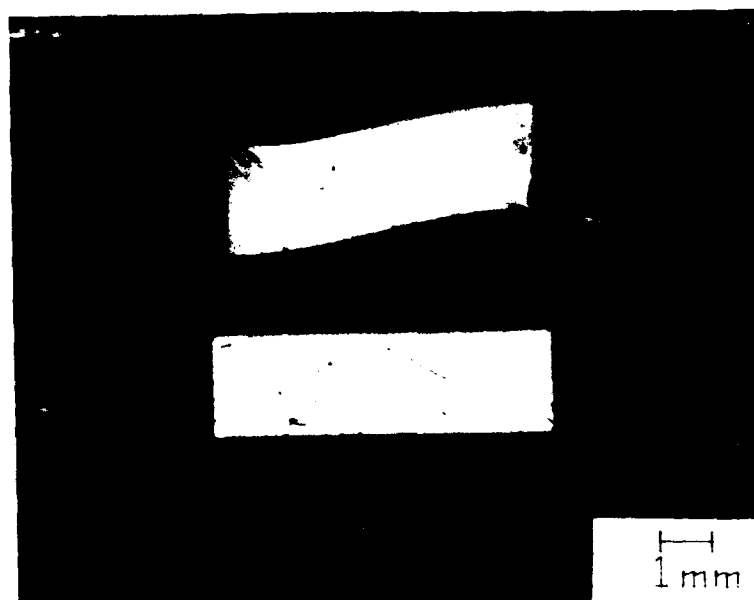


Figure 18. Typical YAG creep specimens:
Bottom: as polished
Top: after creep testing

crystal are primarily polishing scratches or dirt). As with the YSZ and ThO₂, the YAG specimens displayed primarily a skew-type deformation with little change in cross-sectional area for small strains.

As with the YSZ and ThO₂ materials, each creep specimen was utilized for more than one test. A primary creep regime was observed during most creep tests, even when a small load was maintained on the specimen during the change of test conditions. However, the primary regime was generally most extensive during initial testing of the specimens. The lengths of the primary regimes varied considerably with test temperature, stress and sample orientation, ranging from several tenths of a percent strain to being undetectable. Though most initial deformations were characterized by a decreasing strain rate with time, a few tests showed increasing strain rates, especially at high temperatures and stress levels. More typical creep behavior, having a relatively small primary regime, is shown in the strain versus time plots in Figure 19. Although Figure 19 shows the lowest creep rate for the [111] alignment and highest for the [100] alignment, the relative magnitudes of the creep rates for the three crystal directions changed considerably with temperature and stress.

The measured steady state creep rates for all three alignments of YAG are listed in Table 7 and shown graphically in Figures 20 through 22. Rather unusual creep behavior was found for the [100] and [110] alignments in that the stress exponents and activation energies appear to increase abruptly with increases in either temperature or stress. At first, the data were so confusing that several repeat experiments, as well as extra experiments at 1800°C, were conducted to try to better define the creep behavior. The observed behavior indicates a possible change in creep mechanism in the higher stress and temperature ranges. On the other hand, the data for the [111] alignment appear quite well behaved, with only the single data point at 1850°C and 280 MPa suggesting the onset of a higher creep rate regime.

Data analysis for the YAG specimens was complicated due to the apparent change in creep mechanism mentioned above. The data in the low temperature-low stress regimes were analyzed separately from that in the high temperature-high stress regimes (hereafter referred to as "low" and "high" regimes, respectively) for the [100] and [110] alignments. This was done by first visually separating the data points into their appropriate regimes. Regression analyses were then run on each data set to determine the activation parameters for that regime. The data were then compared with the predicted behavior from the regression fits and individual data points exchanged between the two regimes depending on which prediction it more closely matched. The regressions were then redone on the newly separated data sets. The results of this fitting procedure are indicated by the lines in Figures 20 and 21, where the predictions for the low regimes are shown by the solid lines, and those for the high regime by the dashed lines. The data for the [111] aligned crystals was analyzed all at once.

The determined values for the stress exponents and activation energies were as follows: $n = 2.69 \pm 0.20$, $Q = 674 \pm 40$ kJ/mole for the low regime of the [100] alignment; $n = 9.53 \pm 0.86$, $Q = 2064 \pm 1797$ kJ/mole for the high regime of the [100] alignment; $n = 6.18 \pm 0.26$, $Q = 650 \pm 56$ kJ/mole for the low regime of the [110] alignment; $n = 12.46 \pm 0.63$, $Q = 2390 \pm 161$ kJ/mole for the high regime of the [110] alignment; $n = 5.64 \pm 0.24$, $Q = 710 \pm 37$ kJ/mole for the [111] alignment. (Please note: Due to the small number of data

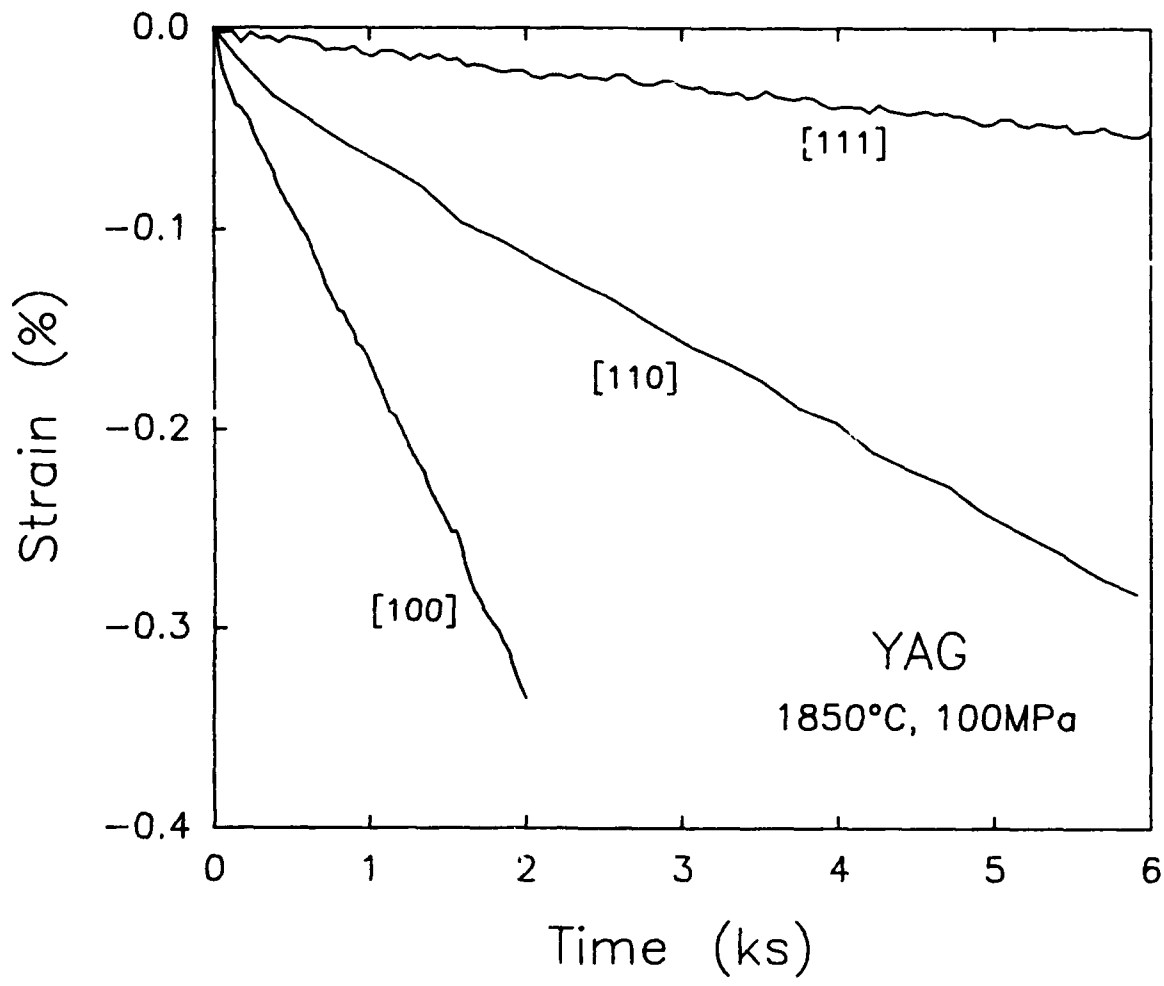


Figure 19. Typical creep strain vs. time behavior for YAG specimens.

**Table 7. Steady-State Creep Data for Yttrium
Aluminum Garnet Single Crystals**

Temperature (°C)	Stress (MPa)	Creep Rate (sec ⁻¹) for Given Stress Direction		
		[111]	[110]	[100]
1650	100		1.73x10 ⁻⁹	2.27x10 ⁻⁸
	140	1.17x10 ⁻⁸	1.50x10 ⁻⁸	4.64x10 ⁻⁸
	200	8.88x10 ⁻⁸	1.43x10 ⁻⁷	1.17x10 ⁻⁷
	200		7.26x10 ⁻⁸	2.32x10 ⁻⁷
	280	4.36x10 ⁻⁷	1.14x10 ⁻⁶	4.25x10 ⁻⁷
1750	70		5.95x10 ⁻⁸	
	100	1.52x10 ⁻⁸	1.31x10 ⁻⁸	2.20x10 ⁻⁷
	140	8.32x10 ⁻⁸	8.00x10 ⁻⁸	5.17x10 ⁻⁷
	200	3.38x10 ⁻⁷	9.82x10 ⁻⁷	9.58x10 ⁻⁷
	200		5.13x10 ⁻⁶	
	200		9.02x10 ⁻⁷	
	280	5.62x10 ⁻⁶	1.67x10 ⁻⁴	4.81x10 ⁻⁵
1800	100			3.42x10 ⁻⁷
	140		1.11x10 ⁻⁶	1.22x10 ⁻⁶
	200		1.42x10 ⁻⁴	4.05x10 ⁻⁵
1850	50			2.17x10 ⁻⁷
	70			6.65x10 ⁻⁷
	100	8.66x10 ⁻⁸	3.60x10 ⁻⁷	1.61x10 ⁻⁶
	140	6.69x10 ⁻⁷	6.51x10 ⁻⁵	1.74x10 ⁻⁵
	200	5.76x10 ⁻⁶	3.20x10 ⁻³	3.80x10 ⁻⁴
	200		2.25x10 ⁻³	
	280	1.78x10 ⁻⁴		

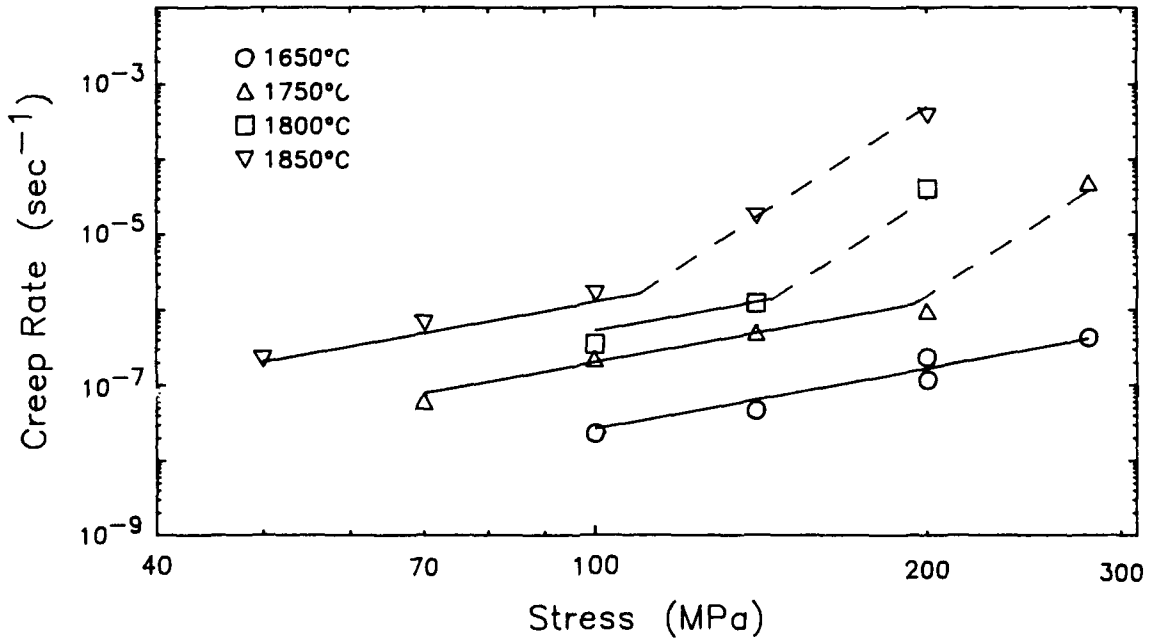
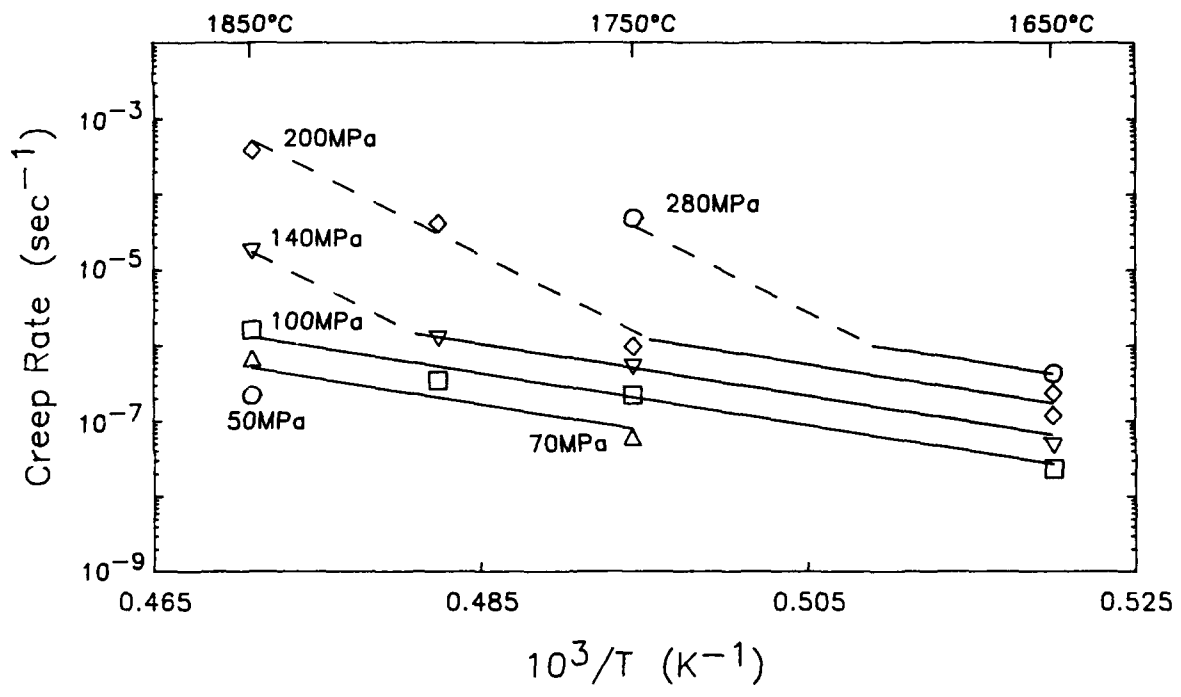


Figure 20. Steady state creep rate data for [100] YAG

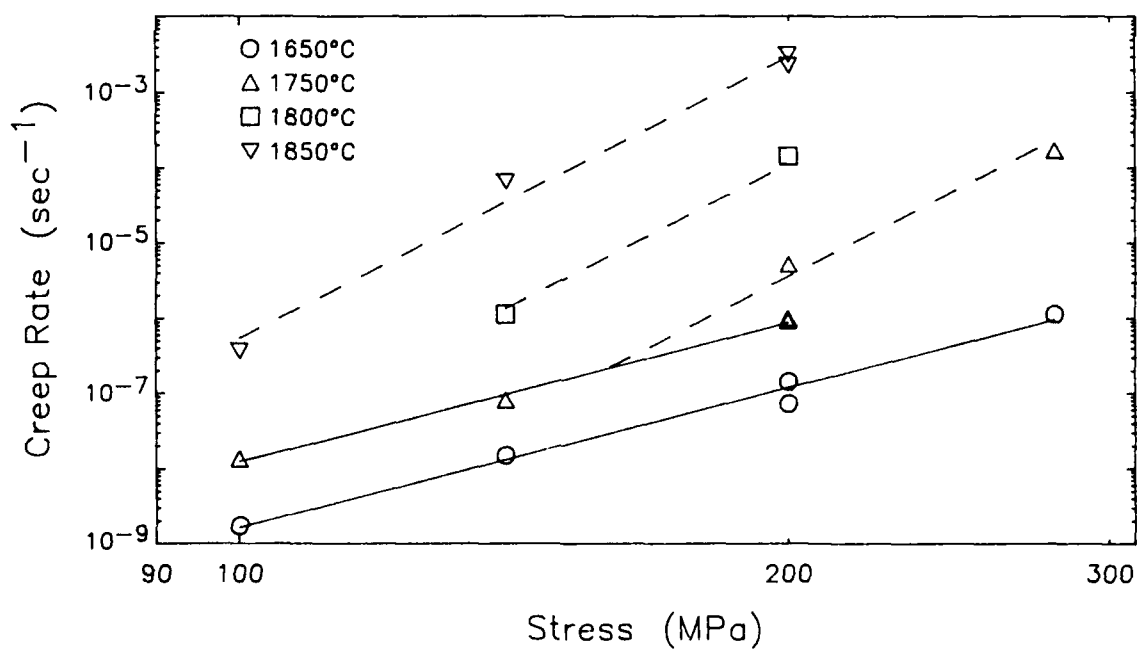
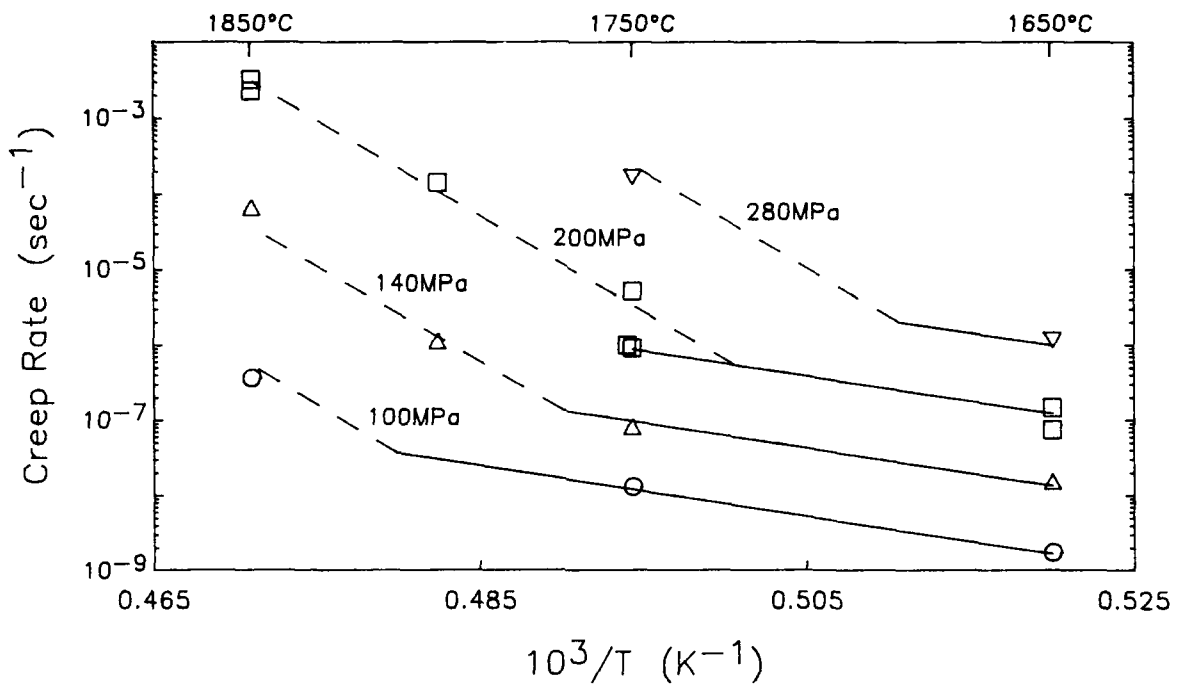


Figure 21. Steady state creep rate data for [110] YAG

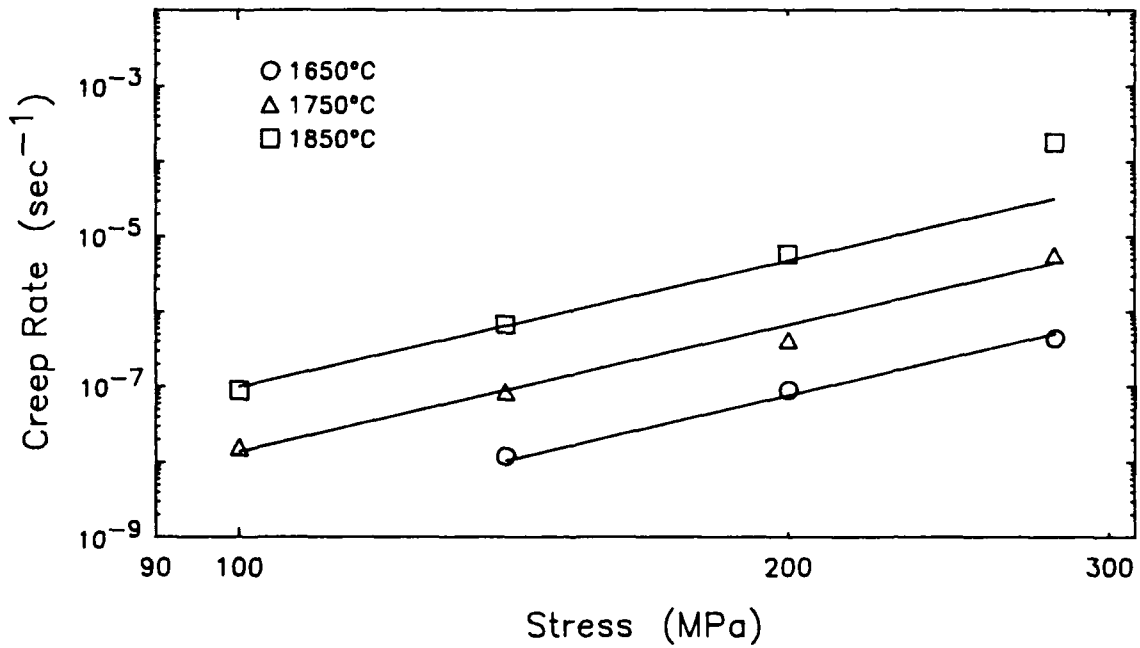
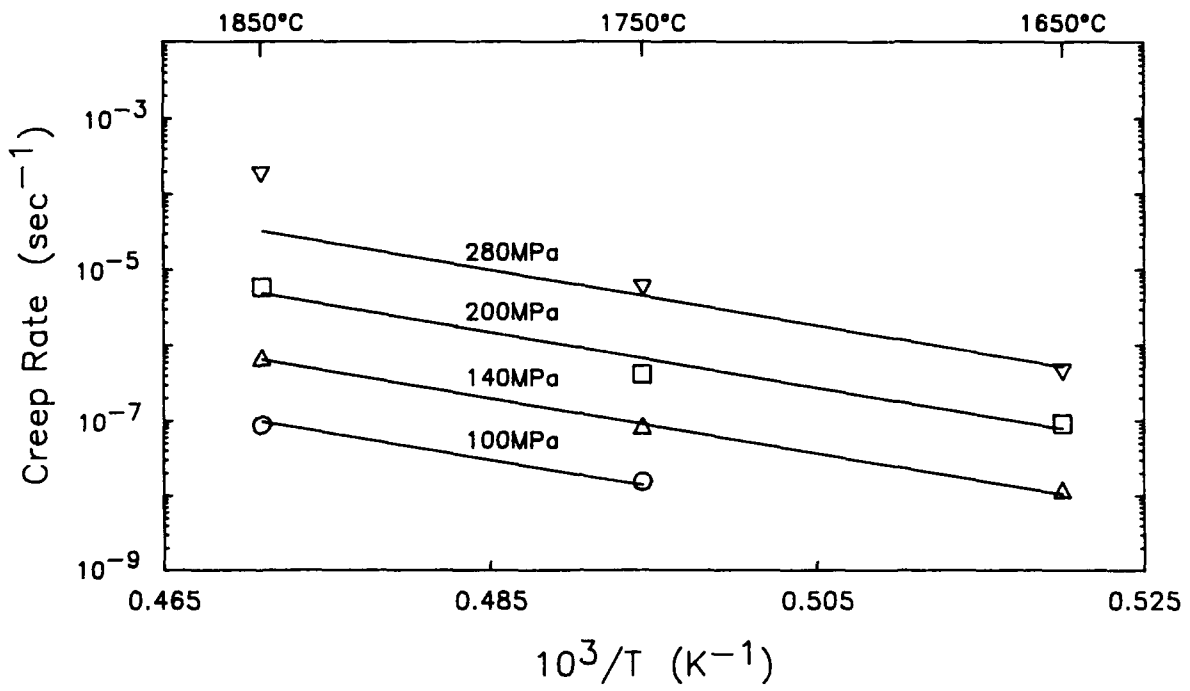


Figure 22. Steady state creep rate data for [111] YAG

points in the high creep rate regimes, values for the stress exponents and activation energies for these regimes should be considered to be rough approximations only. The values are not intended to represent rigorous determination of the activation parameters of any deformation process, but are given simply to allow relative comparisons of the data from the different regimes.) The activation energies for the low creep rate regimes, though they do show variation, all fall within 10% of each other. It would thus appear that this activation energy (average value 678kJ/mole) is indeed representative of the rate controlling mechanism in the low creep rate regime. This is over twice the value for the reported activation energy for O diffusion in YAG (297 to 325kJ/mole depending on heat treatment (37)). Activation energies for cation diffusion in YAG could not be found. Whether or not diffusion plays a significant role in the deformation of YAG is therefore still unanswered.

Another surprising aspect of the creep data is the large variation of stress exponent with orientation. Stress exponents for [111] YAG and the low regime of the [110] alignment (5.64 and 6.18, respectively) are in reasonable agreement; however, the stress exponent for the [100] low regime, 2.67, is substantially lower. In fact, the creep rate data from the [111] alignment and low creep rate regime of the [110] alignment agree very well, yet both differ substantially with the [100] low regime data. The primary slip system for YAG has never been determined unambiguously; nevertheless, the slip systems listed in Table 2 are expected to be the most likely based on theoretical considerations (38, 39), etch pit analysis (39) and observations on other garnet materials (40-42). The fact that the low regime stress exponent for the [100] alignment is so much lower than for the other alignments suggests that different slip systems may be active for this alignment. This would be consistent with slip occurring on the {100} planes, since those slip systems would not be activated by a [100] stress. Slip for the [100] orientation would then presumably occur via slip on a secondary, more difficult system. Unfortunately this is inconsistent with the fact that creep of the [100] orientation in the low regime is generally higher than for the other orientations. As such, the creep mechanism and active slip systems for YAG are still uncertain.

Figures 23 and 24 show several optical micrographs of tested YAG surfaces. The appearances of the surfaces varied from sample to sample. Most tested crystals appeared identical to as-polished crystals, as shown in Figure 23. A few crystals showed evidence of what appears to be dendritic deposits and/or a "crazed" surface (Figure 24A), and still others have an appearance suggesting partial melting or vaporization (Figure 24B). Most of the dendritic-type features were found on {100} type surfaces on [100] aligned specimens. The "melted" appearance occurred only in samples heated to 1800°C or above, yet several other specimens heated to 1850°C showed no such features. Due to the lack of sufficient relief, these features were generally not discernable in the SEM; however, the white balls in Figure 24B were identified as tungsten using energy dispersive analysis of X-rays (EDAX). These are most likely the result of vapor transport from the tungsten mesh heating elements. EDAX analysis of the rest of the surface, and the surfaces of other samples, detected only Al and Y. Thus, the cause for these unusual surface features remains unknown.

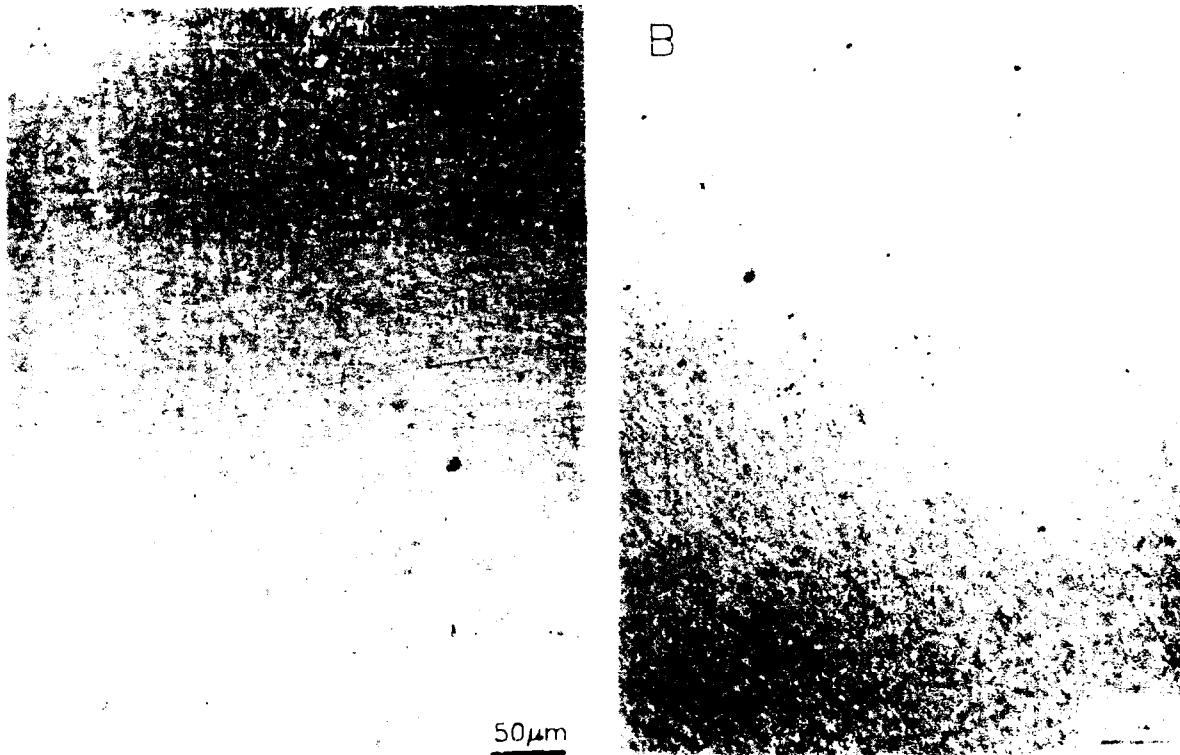


Figure 23. Surface features on YAG creep specimens:
A. As-polished.
B. Tested, showing common featureless surface.

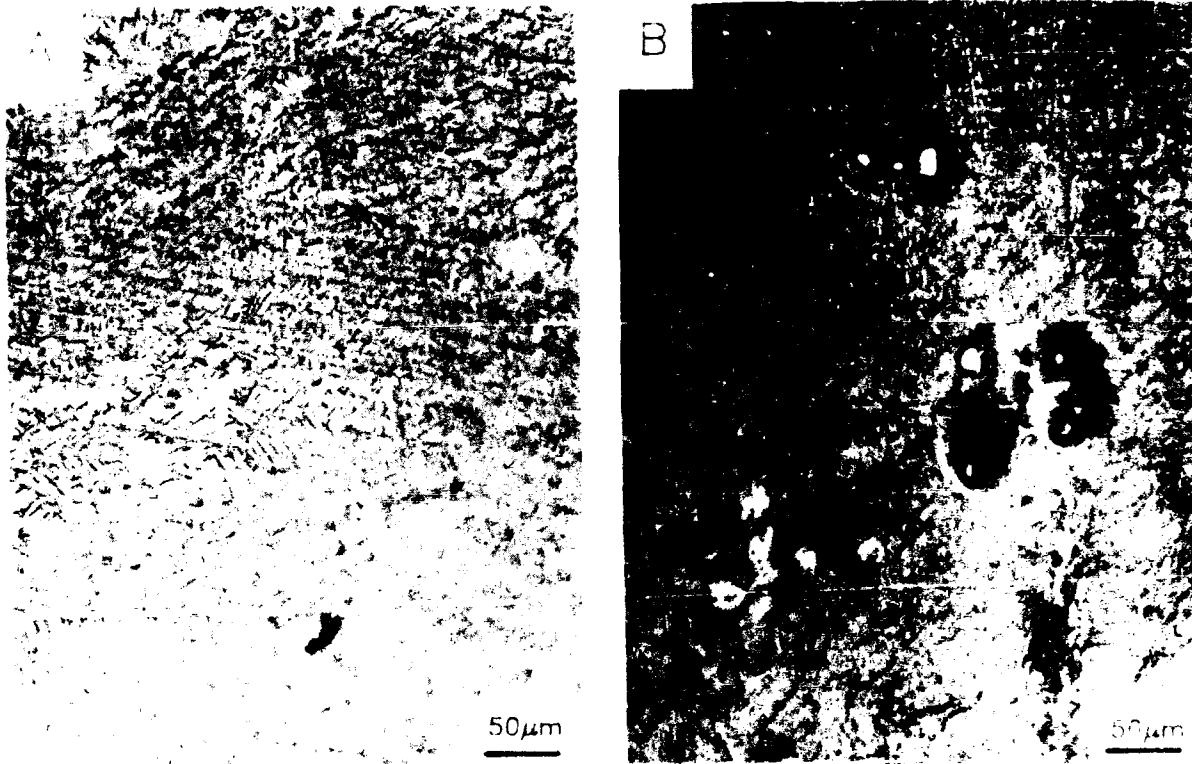


Figure 24. Surface features on YAG creep specimens:
A. Tested, showing "dendritic" deposits.
B. Tested, showing "melted" surface appearance.

3.6. Beryllia

Chemical analysis results for the single crystal BeO are given in Table 4. The only detected impurities of significant concentration were Na (33 ppm) and Mo (30 ppm). This indicates that very little flux was incorporated into the crystal lattice.

Creep of BeO was found to be extremely anisotropic. In order to keep creep rates below 10^{-3} /sec it was necessary to test the $[1\bar{1}01]$ aligned BeO at temperatures from 900° to 650°C. The $[1\bar{1}00]$ and $\langle 0001 \rangle$ alignments were tested in the range 1650° to 1850°C. Due to the low temperatures involved, $[1\bar{1}01]$ samples were tested using $\{100\}$ plates of YSZ as platens with no platen indentation noted. The $[1\bar{1}00]$ BeO was tested using either YSZ or (0001) sapphire plates as platens. As will be discussed later, all $[1\bar{1}00]$ aligned samples buckled during testing so that direct comparisons of crystal strains measured during and post-test could not be done. However, little platen deformation was noted following creep testing. Severe platen problems were experienced with the $[0001]$ aligned samples, which will be discussed below. All creep testing of BeO was done in a high purity He atmosphere.

Due to the high degree of anisotropy found in the behavior of BeO, the creep results for each alignment will be discussed separately. The creep strain versus time behavior was very similar to that discussed previously for the YSZ, ThO₂ and YAG specimens. Steady state creep rates were again determined using linear regression analysis of the linear portions of the strain versus time plots. The creep rate data are listed in Table 8.

The $[1\bar{1}01]$ data indicate that significant creep rates were observed at very low temperatures, as low as 650°C. Plots of the observed steady state creep rates as functions of temperature and stress for the $[1\bar{1}01]$ aligned samples are shown in Figure 25. Creep of this orientation was expected since many hexagonal materials display easily activated basal slip; however, deformation at such a low temperature (less than 1/3 of the melting point) is unusual in ceramics. Although distinct slip traces were not evident on the crystal surfaces due to masking by the grinding marks, the skewed shape of the deformed crystals indicated that basal slip had occurred.

Another unusual observation was that consistent creep rates could not be determined at stresses above 70 MPa. Multiple creep experiments were run at 100 MPa and at temperatures from 600° to 700°C. The measured creep rates were comparable to or lower than the corresponding data at 70 MPa, were not linearly dependent on reciprocal temperature, and were not reproducible. For these reasons the 100 MPa data was not included in Table 8 or Figure 25.

It is not clear why the creep rates should become erratic with increased stress. Previous researchers(43) concluded that BeO had very similar yield stresses for basal, $(0001)\langle 1\bar{1}20 \rangle$, and prismatic, $\{1100\}\langle 1\bar{1}20 \rangle$, slip at 1000°C. It is possible that at stresses below 100 MPa the observed creep behavior is dominated by basal slip, but that at 100 MPa or above the prismatic system is activated. Cross-slip on these two systems could then lead to a loss of dislocation mobility and the observed decreases in creep rate. This explanation, however, is purely speculative.

Table 8. Steady State Creep Data for Beryllia Single Crystals

Orientation	Temperature (°C)	Stress (MPa)	Creep Rate (sec ⁻¹)
[1101]	650	50	1.31x10 ⁻⁷
		70	7.29x10 ⁻⁷
	700	25	3.15x10 ⁻⁸
		50	1.85x10 ⁻⁶
		70	4.49x10 ⁻⁶
	750	25	3.81x10 ⁻⁷
		50	1.15x10 ⁻⁵
	800	12.5	1.97x10 ⁻⁷
		25	2.11x10 ⁻⁶
		30	8.31x10 ⁻⁶
	850	12.5	9.19x10 ⁻⁷
	900	12.5	9.70x10 ⁻⁶
	[1100]	1650	50
100			1.55x10 ⁻⁷
1750		50	3.35x10 ⁻⁸
		70	9.23x10 ⁻⁸
		100	3.34x10 ⁻⁷
1850		140	1.10x10 ⁻⁶
		50	2.35x10 ⁻⁷
		70	4.79x10 ⁻⁷

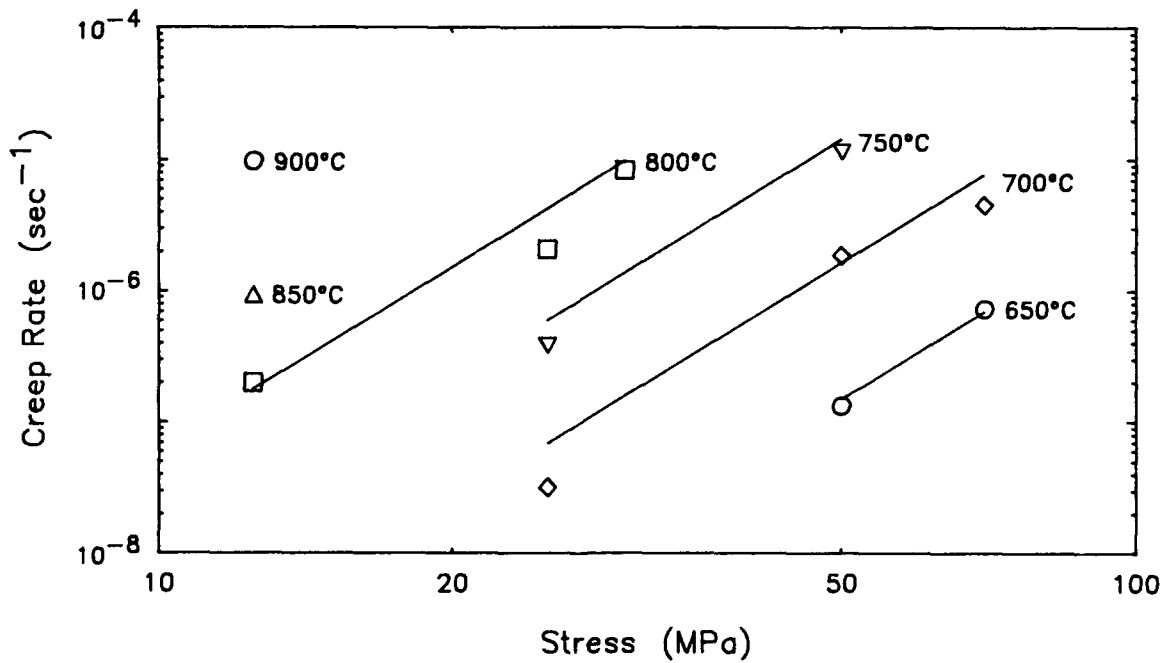
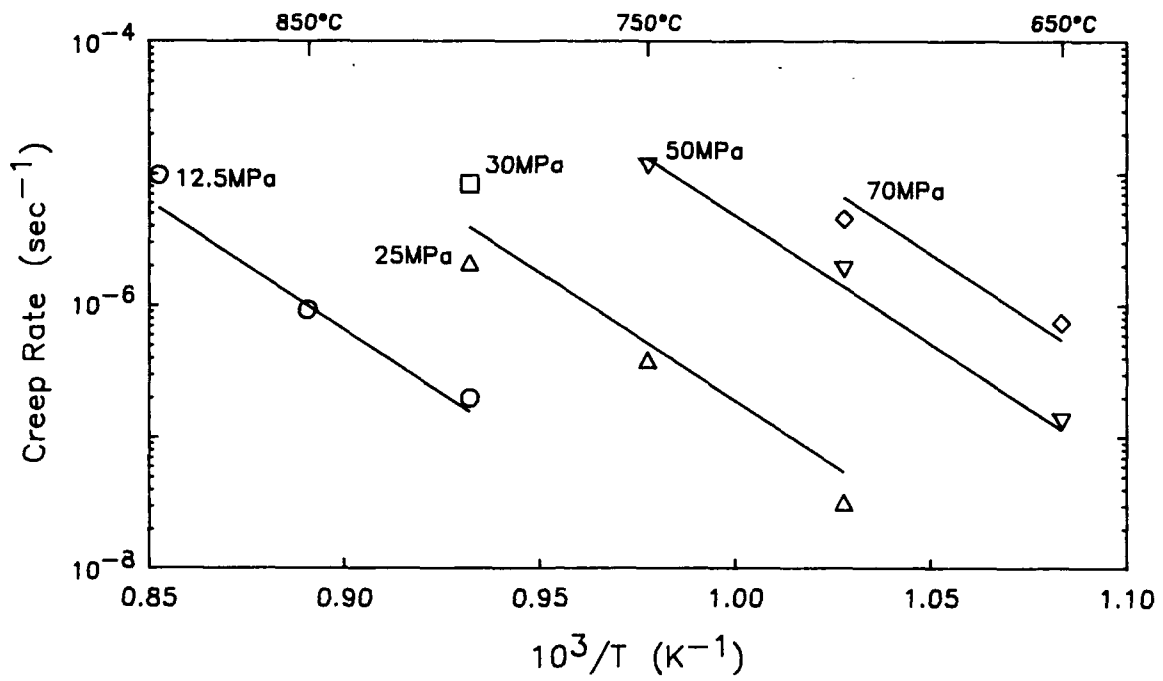


Figure 25. Steady state creep rate data for $[1101]$ BeO.

Regression analysis of the $[\bar{1}101]$ alignment data gave a stress exponent of 4.66 ± 0.36 and an activation energy of 376 ± 26 kJ/mole. This exponent falls well within the range expected for slip creep mechanisms (3 to 5). Activation energies reported in the literature for self diffusion in BeO single crystals similar to those used in this study are 268kJ/mole for Be diffusion (44) and 287kJ/mole for O diffusion (45). It thus appears unlikely that creep of this orientation is diffusion controlled, which is not surprising since the deformation is observed at temperatures below that where diffusive mechanisms would be expected to dominate behavior.

Steady state creep rate data for the $[\bar{1}100]$ BeO alignment are shown in Figure 26. Only eight data points were obtained for this alignment due to severe buckling problems. The $[\bar{1}100]$ alignment places the basal planes on edge. Due to the very easy basal slip discussed above, this orientation is unstable, much like a deck of cards laid on end. Any slight misalignment or bending force would place a shear stress on the basal planes, causing the samples to buckle. A set of specimens displaying varying degrees of buckling deformation is shown in Figure 27.

All $[\bar{1}100]$ specimens buckled in this way during testing, with most samples buckling during initial loading. Once buckling initiated, further deformation proceeded very rapidly. Deformation following buckling was generally so extensive that the loading rod displacement exceeded the measurement range of the LVDT, and proceeded until the sample was unloaded or failed. Only three crystals resisted buckling long enough for adequate creep data to be collected. The creep data in Table 8 and Figure 26 were obtained from these three crystals. Even these three crystals, however, eventually buckled during testing.

The small amount of creep data obtained was well behaved and self consistent, as shown by the plots in Figure 26. Multiple regression analysis of this data yielded a stress exponent of 3.38 ± 0.36 and an activation energy of 496 ± 63 kJ/mole. While the stress exponent is in the range expected for slip creep mechanisms, the activation energy is again larger than those reported for self diffusion in BeO. Indeed, the activation energy is substantially larger than that measured for the $[\bar{1}101]$ alignment. Reported activation energies for creep in polycrystalline BeO range from 402 to 414kJ/mole when a diffusive mechanism is observed (46,47), up to 607kJ/mole for dislocation controlled creep (48). There is thus a significant discrepancy between diffusion data and creep data with regard to activation energies, making interpretation of the activation energies measured in this study practically impossible.

Creep testing was also performed on $[0001]$, or c-axis, aligned crystals; however, no unambiguous creep data were obtained due to deformation of, or reaction of the sample with, the platens used. The entire supply of eleven samples were tested using platens of BeO, YSZ, sapphire, YAG, CVD SiC, graphite and various combinations of the above. In no case was a perfectly acceptable platen material found. The BeO, YSZ and sapphire platens all deformed much more than the crystal being tested, and the YAG and SiC both reacted with the samples. Only graphite appeared to be a useful platen material. Thermodynamically, BeO and carbon should react at the testing temperatures used in this study forming beryllium carbide and CO, provided there is no build up of CO to limit the reaction. A BeO specimen was creep tested at 1750°C for over 16 hours in contact with graphite platens with no signs of

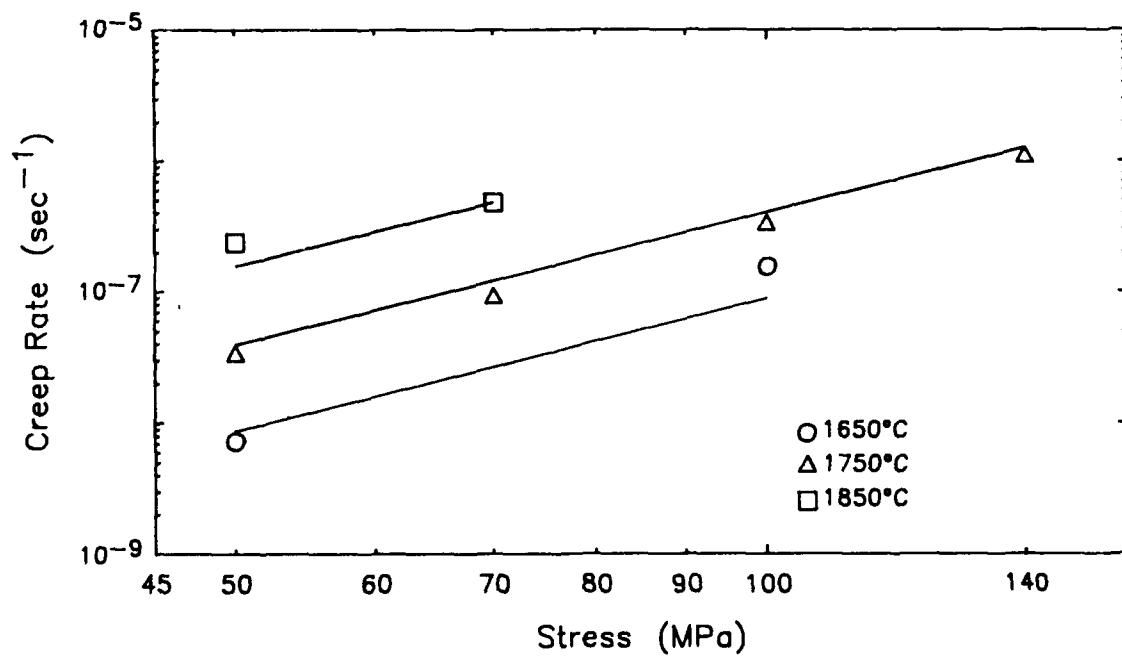
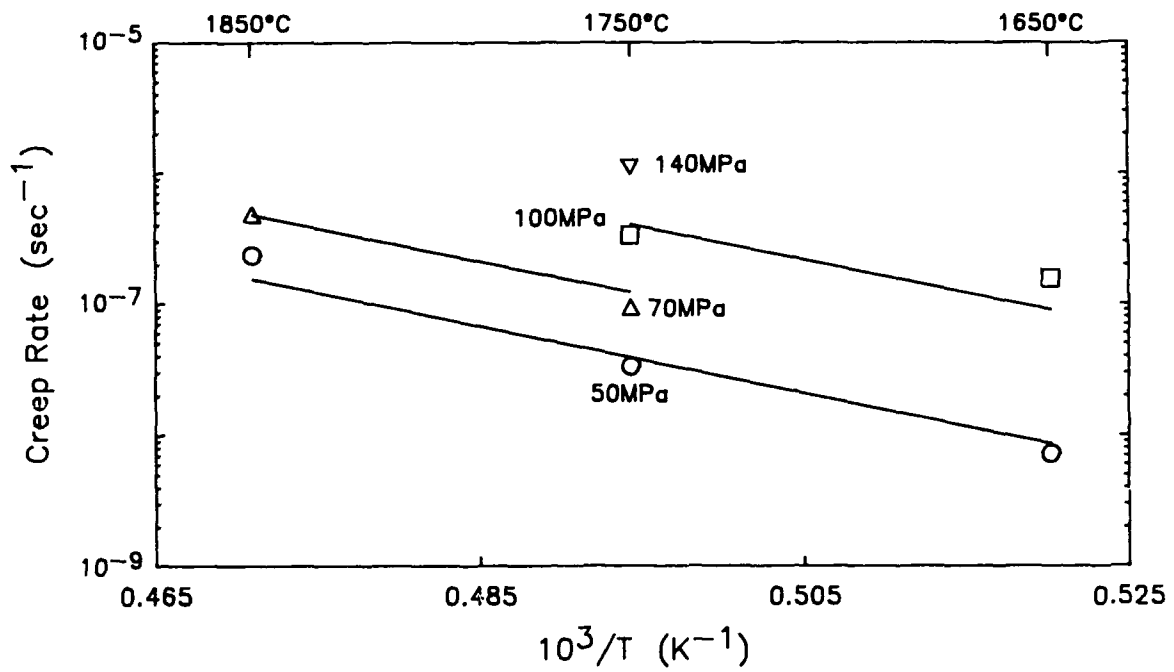


Figure 26. Steady state creep rate data for $[1\bar{1}00]$ BeO.



Figure 27. Micrograph of $[1\bar{1}00]$ BeO creep specimens showing progressive levels of buckling deformation.

reaction. This suggests that there was little migration of CO from the sample/platen interface and the reaction was self limiting. The strain measured from sample dimensions following the test was, however, only one third of that measured from loading rod displacement during the test. This indicates that some platen deformation, most probably some deformation/reaction of the graphite platens with the tungsten loading rods, did occur.

Assuming that the actual crystal deformation occurred at a constant rate over the length of the test, the estimated creep rate would be 1.7×10^{-8} /sec at 1750°C and 100 MPa. This is a very low creep rate, comparable to [111] or [110] YAG at these same conditions. However, this represents an upper bound on the creep rate of c-axis BeO; the actual creep rate may be somewhat lower. As such, the creep behavior of c-axis BeO is yet to be determined.

3.7. Alumina

Limited creep testing of single crystal Al_2O_3 (sapphire) was performed primarily as a check of the test equipment and procedures. Sapphire, due to its availability in fiber form, has perhaps been studied more than any other single crystal oxide in terms of deformation behavior. Sapphire is also generally considered a reference material against which performance of other ceramics are often judged, with c-axis sapphire being one of the most creep resistant oxides known. Since the creep behavior of a material can vary somewhat depending on test conditions, direct comparisons of the creep behavior of the materials studied here with sapphire would require that the sapphire be tested under identical conditions.

Only c-axis aligned crystals were tested in this study. Measurements were done in the range of 1650° to 1850°C and 140 to 400 MPa. During several creep tests the creep rate was found to accelerate, often following a period of steady state creep. This accelerated creep led to cracking and failure of most specimens.

Examination after testing indicated that samples exhibiting accelerated creep were twinned. Micrographs of one of these crystals is shown in Figure 28. Three features are evident on the micrographs: slip steps in the crystal faces parallel to the basal planes, twinned regions, and cracks. Examination of the different faces of several twinned crystals indicates that the twin plane is consistent with a {0112} type (using the structural unit cell with $c/a = 2.73$), which agrees with previous results for sapphire (43). Most twins observed appeared to emanate from a crystal corner, and were often associated with cracking. Micrograph B in Figure 28 shows the nucleation of a crack from intersecting twin bands. The complex microstructures observed make it difficult to interpret the exact cause of the creep rate accelerations. Since sapphire was not one of the major materials of interest in this study this aspect of its deformation behavior was not studied in detail. One likely scenario is as follows: first, due to slight crystal or platen misalignments or offsets in the crystal end due to pyramidal slip, the crystals were subject to some non-axial stress; next, the nonaxial stress caused basal slip, with the resultant shear deformation contributing further to the off-axis stresses; thirdly, the off-axis stresses caused stress concentrations on the crystal corners, nucleating twins and/or cracks; finally, twin growth and intersection caused further cracking. The sudden, discontinuous increases in deformation generally associated with twinning were not detected during the creep testing. This suggests that the twinning and cracking occurred far into the accelerated



Figure 28. Reflected light micrographs of a twinned Al_2O_3 creep specimen:
Top: showing twin and crack structure.
Bottom: showing crack initiation at intersecting twinned regions.
The crystal [0001] compression axis is shown by the arrows.

creep rate regime, and that the onset of accelerated creep was due to the initiation of significant basal slip. Creep data collected prior to the acceleration in creep rate should therefore be indicative of normal c-axis crystal creep behavior.

The creep data measured in this study is listed in Table 9 and shown graphically in Figure 29. Overall the data appear to be well behaved and self-consistent. Multiple regression analysis of the data, using the values for G_0 and δG given in Table 3, resulted in a stress exponent of 4.54 ± 0.20 and an activation energy of 470 ± 27 kJ/mole. Various values for activation energies for self diffusion in Al_2O_3 have been measured(50). Likewise, reported stress exponents and activation energies for c-axis sapphire have varied widely in the literature(15). As such, comparison of the activation parameters measured here with values selected from the literature is not very instructive. Both the stress exponent and activation energy for creep fall within the range of previously reported values.

It is perhaps more informative to compare the actual creep rates measured with those from the literature. A plot of creep rate (or strain rate for constant strain rate experiments) versus reciprocal temperature for an applied stress (or flow stress) of 200 MPa is shown in Figure 30. Since few investigators performed measurements at the same stresses used here, it was necessary to estimate strain rates at 200 MPa from the available data. Only studies where the stresses used were above and below 200 MPa, which would allow interpolation of creep rates rather than extrapolations, are included in the graph. Overall the agreement of the data is rather good, with most data falling within a band less than half an order of magnitude wide. Had the basal slip and twinning observed in the tested crystals had a significant contribution to the measured creep rates, one would expect the current creep rates to be much higher than in previous studies. The good agreement of the present c-axis sapphire creep data with previous literature data indicates that the testing procedure was accurate.

3.8. Silicon Carbide

Chemical analysis of the SiC single crystal was not performed due to its already being an extremely high purity, electronic grade material. Based on vendor data (54), total metallic impurities are below 10 ppm, with N being the major impurity dopant at $2 \times 10^{16}/cm^3$ (roughly 0.3 ppm by weight). The crystal was transparent with a greenish tint from the N impurity.

Creep of the SiC single crystal was anticipated to be highly anisotropic due to its having the 6H (hexagonal) polytype structure. We therefore decided to measure only two crystal orientations; [0001] or c-axis, and 45° from the c-axis. These directions were expected to be the best and worst directions, respectively, with regard to creep resistance due to the anticipated easy slip on the basal plane. All creep testing of SiC was done in a He atmosphere using platens of CVD SiC. Graphite was also placed in the furnace hot zone as an oxygen getter to prevent active oxidation of the SiC sample and platens by trace impurity oxygen. An initial test done with graphite platens caused the sample crystal surfaces to darken, presumably from vapor transport of excess carbon from the platens. Samples tested with SiC platens exhibited no color change.

It should be noted that only limited testing of either alignment was done due to limitations in material and time. Nevertheless, the creep data obtained were very interesting. Steady

**Table 9. Steady State Creep Rate Data for
C-Axis Sapphire**

Temperature (°C)	Stress (MPa)	Creep Rate (sec⁻¹)
1650	140	9.50x10 ⁻⁸
	200	3.88x10 ⁻⁷
	280	2.62x10 ⁻⁶
	400	9.06x10 ⁻⁶
1750	140	4.55x10 ⁻⁷
	200	1.38x10 ⁻⁶
	280	9.50x10 ⁻⁶
1850	140	1.28x10 ⁻⁶
	200	8.46x10 ⁻⁶
	280	3.66x10 ⁻⁵

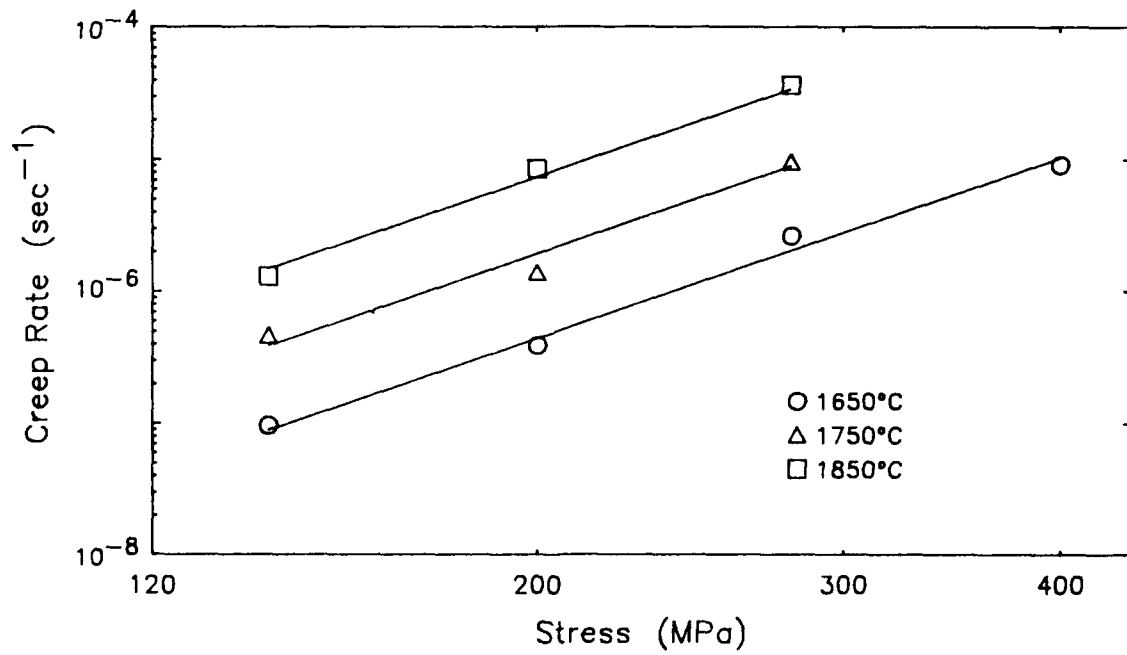
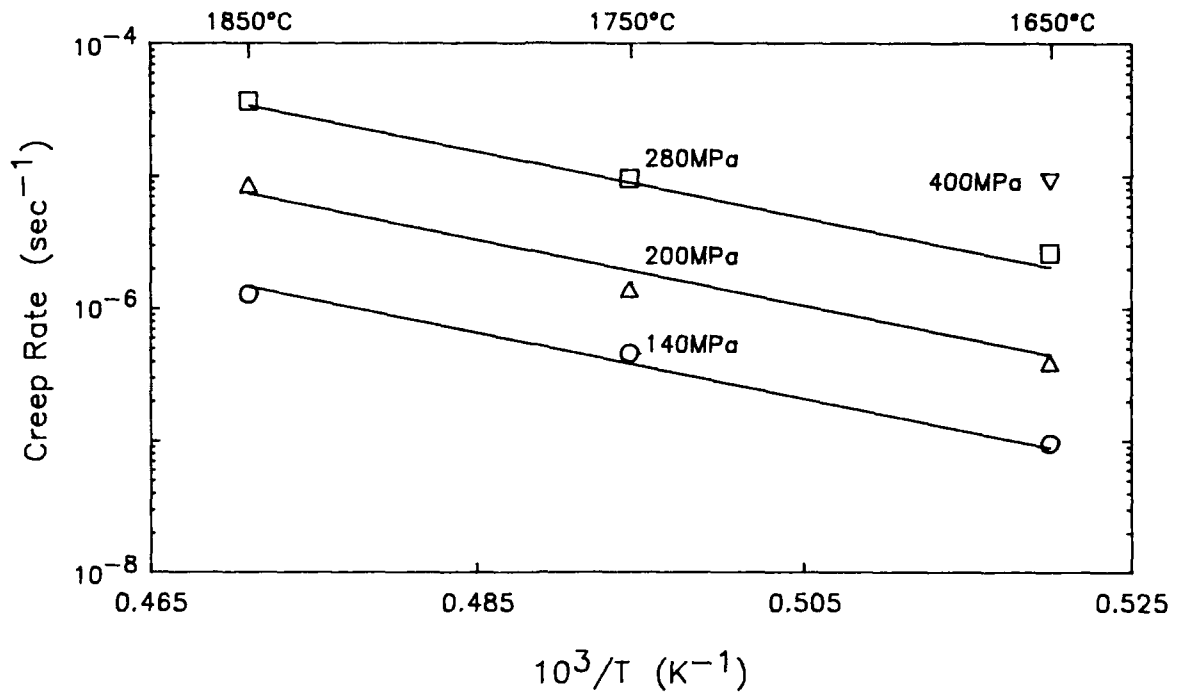


Figure 29. Steady state creep rate data for [0001] Al_2O_3 .

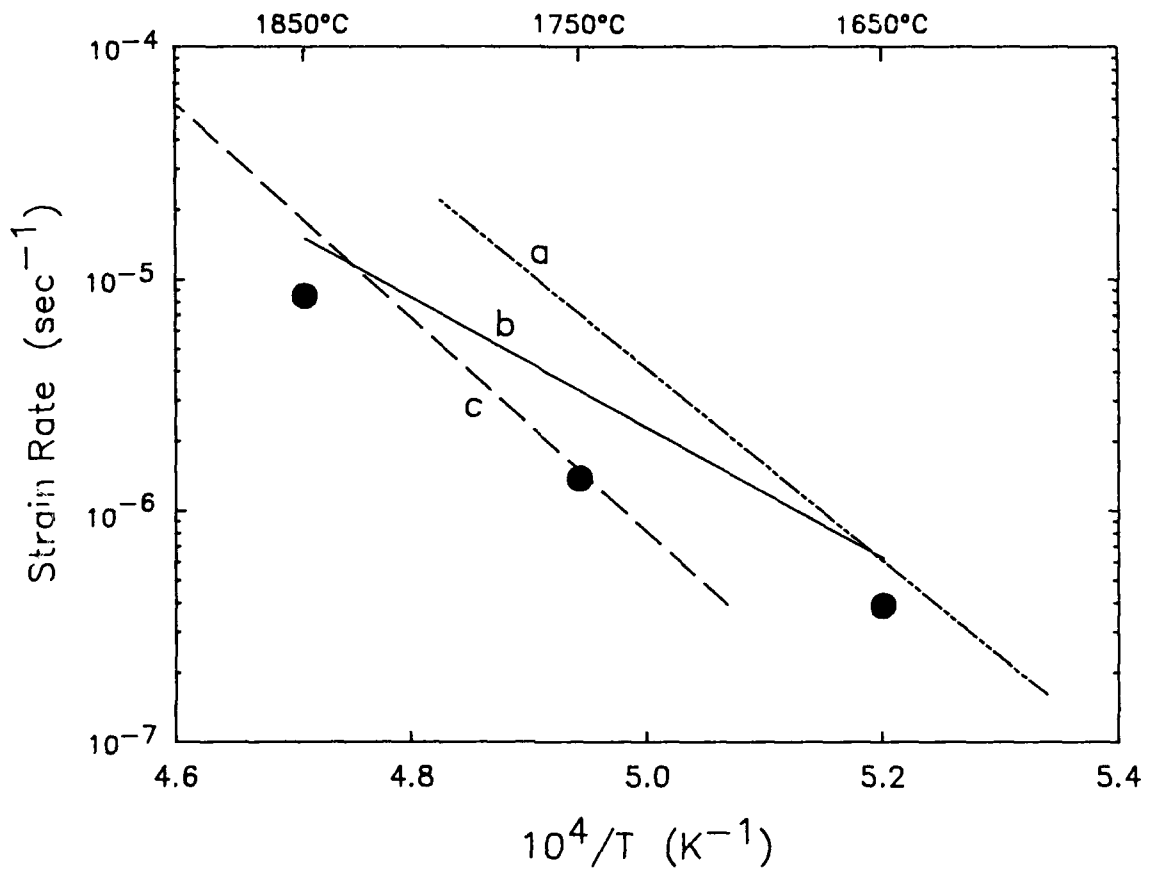


Figure 30. Comparison of [0001] Al_2O_3 creep data at 200 MPa from the present study (dots) with previous deformation data (a. Ref 51; b. Ref. 52; c. Ref 53).

state creep rate data for the SiC single crystals are given in Table 10, and shown graphically in Figures 31 and 32.

As is typical of many hexagonal materials, the 45° alignment was found to creep quite readily via basal slip. Figure 33 shows a micrograph of a specimen surface, clearly showing slip steps at 45° to the crystal axis, and therefore parallel to the basal plane. What was surprising was that significant creep rates ($>10^{-7}/\text{sec}$) could be measured at temperatures as low as 800°C. To our knowledge, this is the lowest temperature at which macroscopic creep of SiC in any form has been measured.

The creep behavior of this alignment was so poor that the accuracy of the measurements were in doubt; however, the easy basal slip of SiC is corroborated by earlier measurements on similar crystals. Maeda(55) has previously measured fairly low yield stresses for basal slip in 6H SiC at temperatures above 1000°C. Using a constant strain rate test, with an approximate strain rate of $3 \times 10^{-4}/\text{sec}$, Maeda measured a resolved yield shear stress of about 30 MPa at 1200°C. For our specimen orientation (45° from the c-axis toward an a-axis, Schmid factor of 0.5) this would correspond to an applied stress of 60 MPa. Results of the regression analysis (see below) predict a creep rate of $2 \times 10^{-5}/\text{sec}$ for 60 MPa, 1200°C and this orientation. Thus the constant strain rate data of Maeda would correspond to an even higher creep rate than measured here. Also, Niihara (56) has predicted considerable plasticity by basal slip above 800°C based on high temperature hardness measurements on 6H SiC single crystals. The relatively easy activation of basal slip in 6H SiC single crystals is therefore confirmed.

Multiple regression analysis of the creep data gave a stress exponent of 3.32 ± 0.41 and an activation energy of 282 ± 23 kJ/mole. This activation energy is much lower than that for the self-diffusion of C (715kJ/mole) or Si (697kJ/mole) in alpha-SiC (57,58). On the other hand, the activation energy for basal slip determined by Maeda (55) was 328 ± 68 kJ/mole, in fair agreement with the value measured here. The stress exponent determined by Maeda was 3.1, also in good agreement.

Measured creep rates for the c-axis SiC samples were also much higher than expected. In a previous creep study of CVD SiC (59) no creep strain could be detected on samples stressed parallel to the deposition direction for test temperatures up to 1750°C and stresses as high as 220 MPa. The deposition direction of this highly oriented material corresponded to the [111] direction of the cubic beta polytype and c-axis of the hexagonal polytypes present. We therefore expected the creep resistance of the single crystal to be comparable to that of the CVD SiC. To the contrary, creep rates above $10^{-8}/\text{sec}$ were measured at temperatures and stresses as low as 1650°C and 140 MPa, respectively.

Tested c-axis SiC specimens had distinct slip steps parallel to the basal planes, as shown in Figure 34. In contrast to the sapphire samples, the c-axis SiC underwent shear by basal slip very early during creep testing as the shear strains were visually evident during the test. Consequently, the samples were subject to significant off-axis loads during creep testing, and could therefore deform via the slip systems listed in Table 2 which would not be active for a pure c-axis stress. This makes the creep data for this alignment somewhat suspect, and may help explain why the creep rates were so unexpectedly high. On the other hand, the creep data obtained in this study was measured from tests on four specimens having various levels

Table 10. Steady State Creep Data for Silicon Carbide Single Crystal

Orientation	Temperature (°C)	Stress (MPa)	Creep Rate (sec ⁻¹)
45°	800	200	1.95x10 ⁻⁷
		100	7.29x10 ⁻⁷
	900	200	2.50x10 ⁻⁶
		50	2.65x10 ⁻⁷
		100	2.91x10 ⁻⁶
	1000	200	2.80x10 ⁻⁵
		50	8.32x10 ⁻⁷
		100	1.42x10 ⁻⁵
	1100	50	8.32x10 ⁻⁷
		100	1.42x10 ⁻⁵
		100	1.36x10 ⁻⁴
	<0001>	1650	140
200			6.70x10 ⁻⁸
1750		140	1.50x10 ⁻⁸
		200	9.90x10 ⁻⁸
		280	5.25x10 ⁻⁷
1850		400	3.08x10 ⁻⁶
		140	3.63x10 ⁻⁸
		200	1.42x10 ⁻⁷

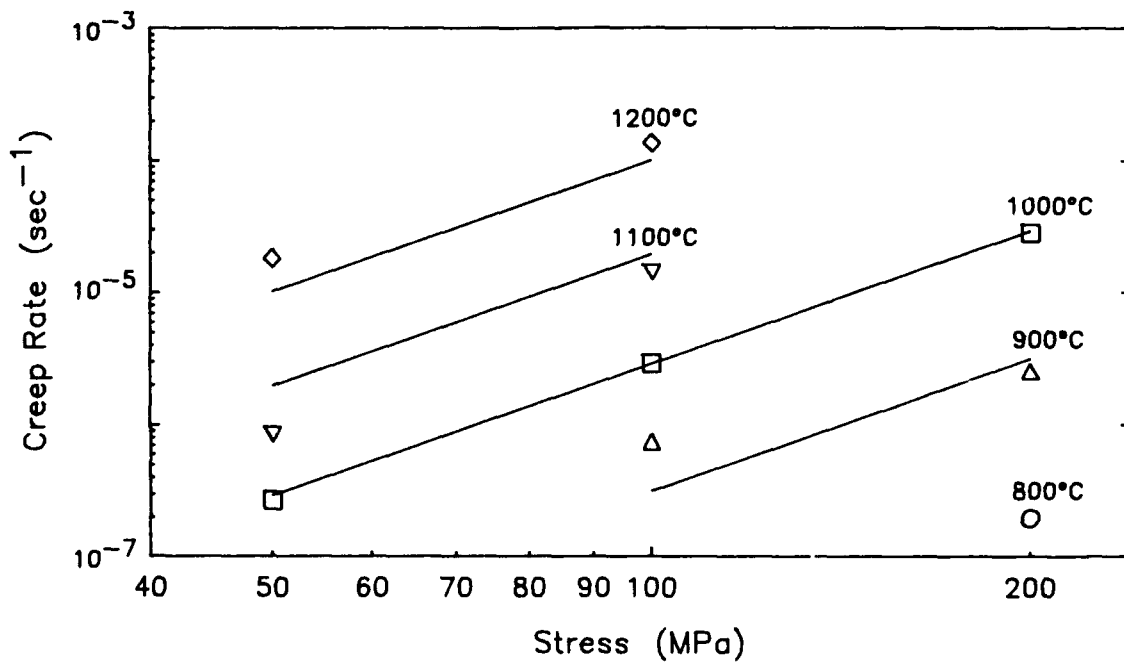
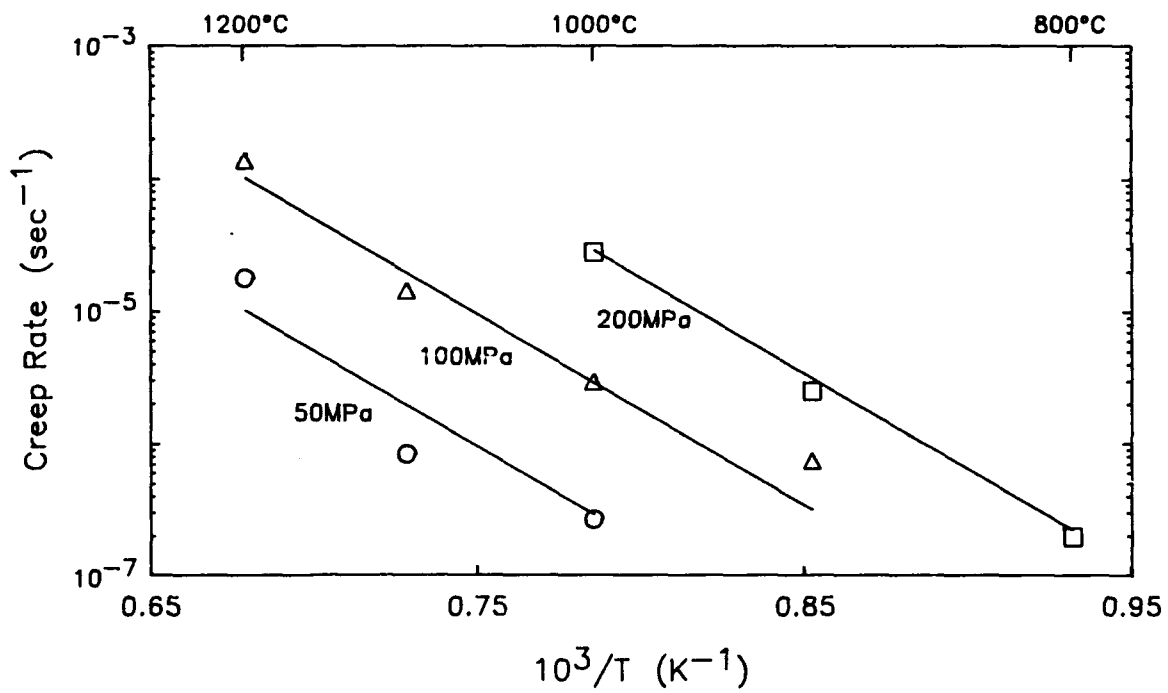


Figure 31. Steady state creep rate data for 45° SiC.

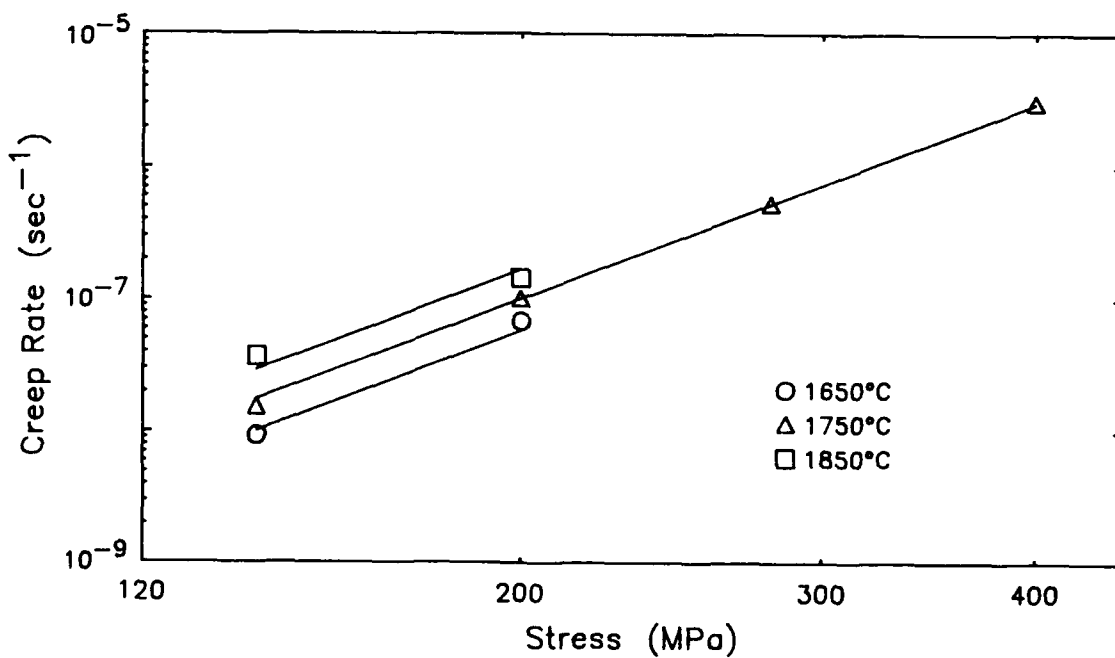
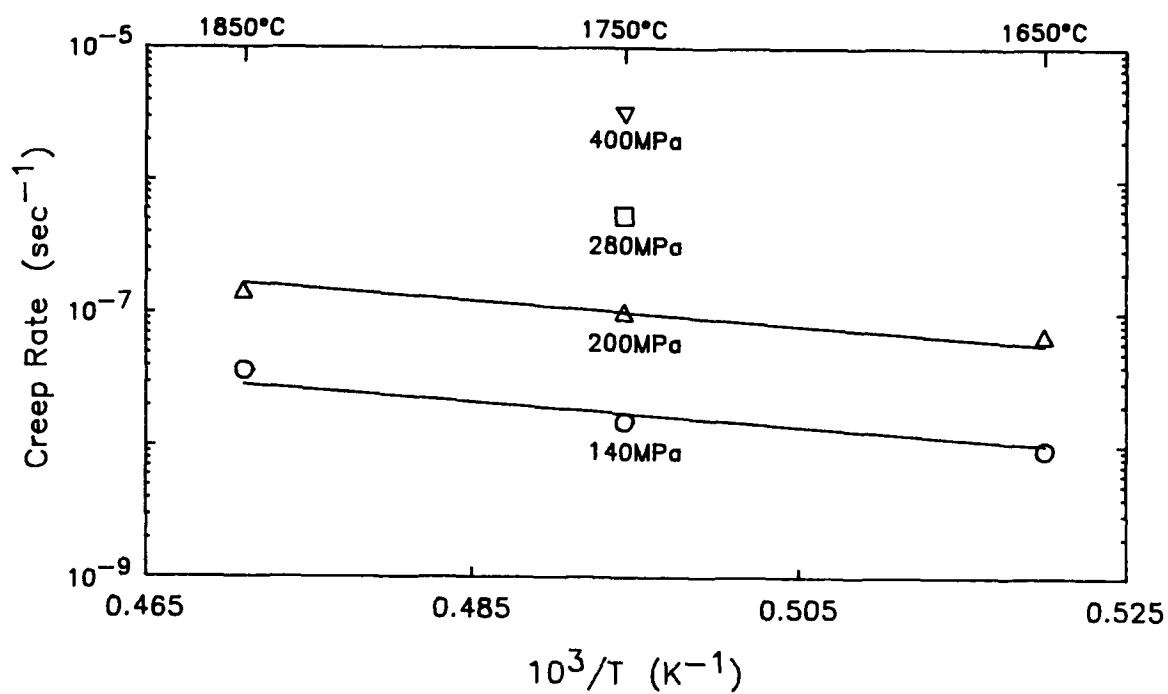


Figure 32. Steady state creep rate data for [0001] SiC.

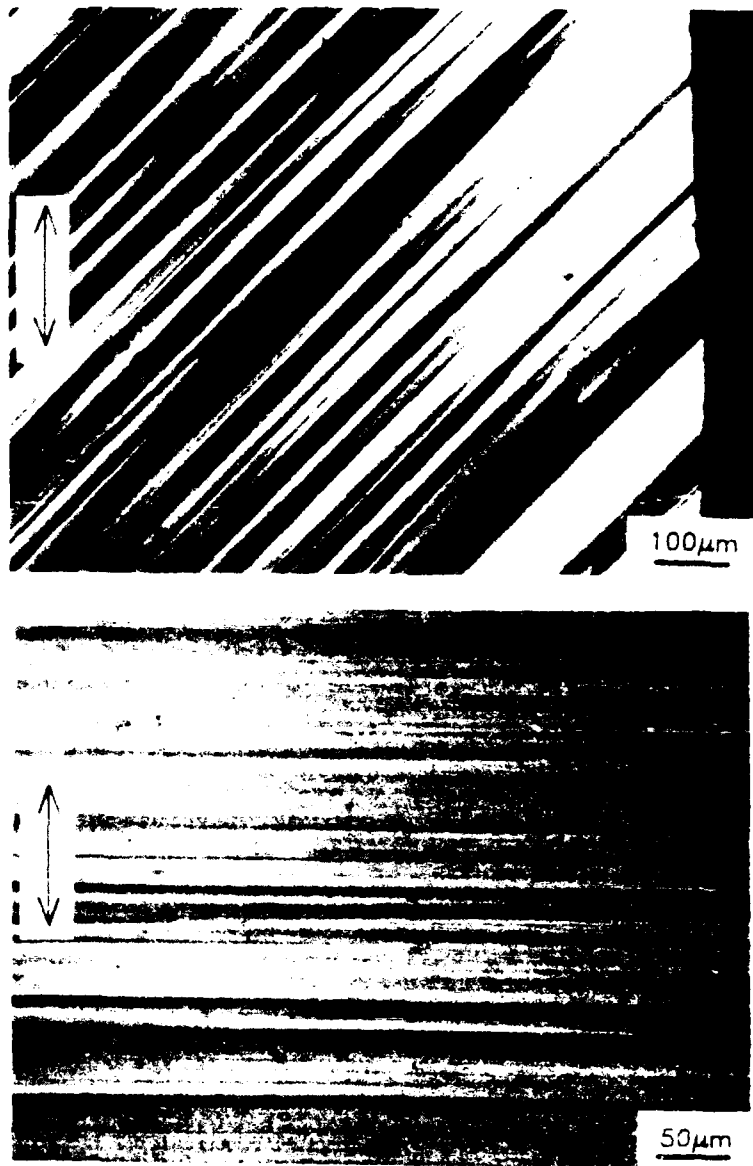


Figure 33. Surfaces of a tested 45° SiC specimen:
Top: $\{1100\}$ type face.
Bottom: face 45° between (0001) and $\{11\bar{2}0\}$.
The compression axis is shown by the arrows.

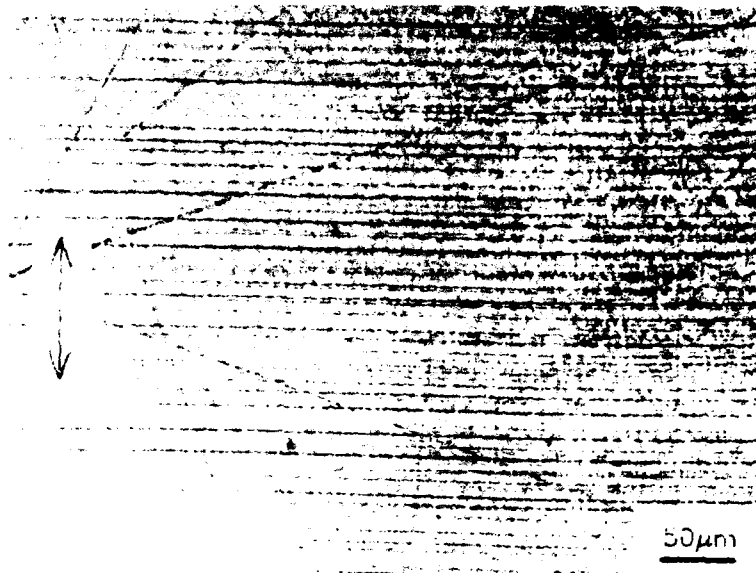


Figure 34. Surface of [0001] SiC creep specimen showing slip steps parallel to the basal plane and polishing scratches. The [0001] compression axis is shown by the arrow.

of initial strain. If the shear from basal slip were affecting the data then its influence should be dependent on previous crystal strain, and the data would not be likely to be very consistent. However, the measured creep data is very self-consistent, as shown in Figure 32. This would suggest that the shear deformation from basal slip had little effect on the c-axis creep behavior and that the measured creep data are representative of true c-axis creep. In either case, independent testing of this material should be performed to corroborate or refute the present data.

Regression analysis of the c-axis creep data gave a stress exponent 4.93 ± 0.16 and an activation energy of 170 ± 27 kJ/mole. The previous study of CVD SiC (59) measured an activation energy of 175kJ/mole, in excellent agreement with that measured here. The stress exponent of the CVD material was temperature dependent, measuring 3.7 at 1750°C and 2.3 below 1750°C.

The relatively poor creep resistance of the single crystal measured here is indicated by the data in Figure 35. This shows the creep data for the c-axis alignment compared to data on several other forms of SiC measured under similar conditions. It shows that creep rates for the c-axis single crystal were comparable to or higher than rates for reaction bonded and sintered SiC materials in the temperature range tested, and over an order of magnitude higher than for CVD SiC. However, the CVD SiC data in Figure 35 is for samples stressed at 45° to the deposition direction, and should therefore be rightfully compared to the 45° single crystal data. Just why the single crystal creep behavior should be so much poorer than other forms of SiC is not entirely clear. SiC does not have 5 independent slip systems, so that plastic deformations of polycrystalline bodies via slip alone is not possible. Creep of polycrystalline materials (in cases where viscous grain boundary phases do not dominate deformation) has therefore generally been found to be diffusion controlled. Creep rates of pure, polycrystalline SiC are comparatively low due to the low diffusivities of C and Si. Still, the highly oriented CVD SiC could presumably deform primarily via slip, and yet it is much more creep resistant than the single crystal material. Apparently the very high purity, exact stoichiometry and perfection of the single crystal allows for much easier dislocation motion than in the mixed polytype CVD material.

4. DISCUSSION

Test results for the individual materials were discussed in the previous sections. This section will deal primarily with comparisons of the different materials and correlations of creep behavior with other material properties.

A summary graph of the creep rates at 100 MPa for the oxide materials tested in this study, along with data on MgAl_2O_4 (63), Y_2O_3 (64) and MgO (65) taken from the literature, is shown in Figure 36. The lines shown in the plot are from the regression fits to the measured creep data, and represent the most creep resistant direction of each material tested ([100] YSZ, [110] ThO_2 , [111] YAG and c-axis BeO and Al_2O_3). This graph clearly indicates the outstanding creep resistance of YAG as compared to other oxides.

The first question to be answered is whether any of the materials have adequate creep resistance to be used as a reinforcement fiber above 1650°C (3000°F). For high precision,

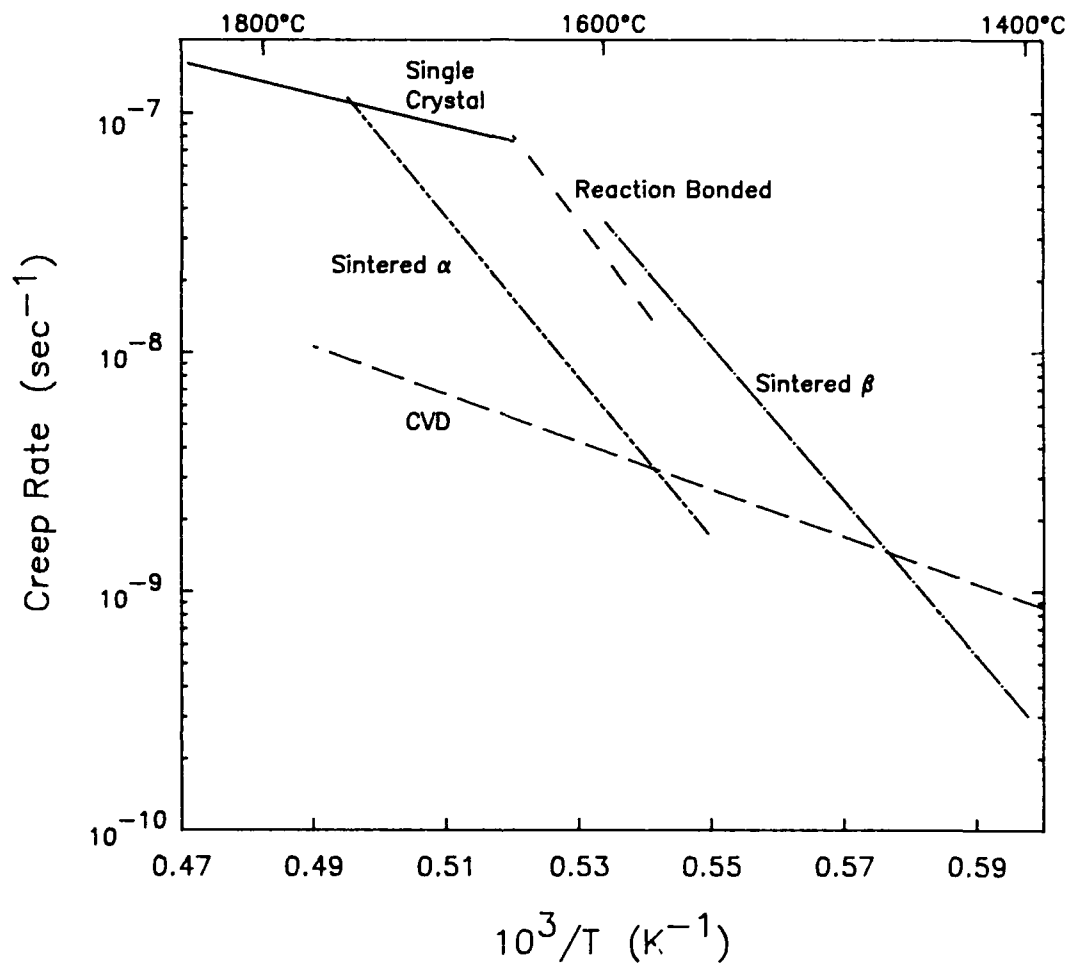


Figure 35. Creep data for several forms of SiC at 200 MPa:
 Single Crystal: [0001], this study.
 CVD: Ref. 59.
 Reaction Bonded: Ref. 60.
 Sintered α : Ref. 61.
 Sintered β : Ref. 62.

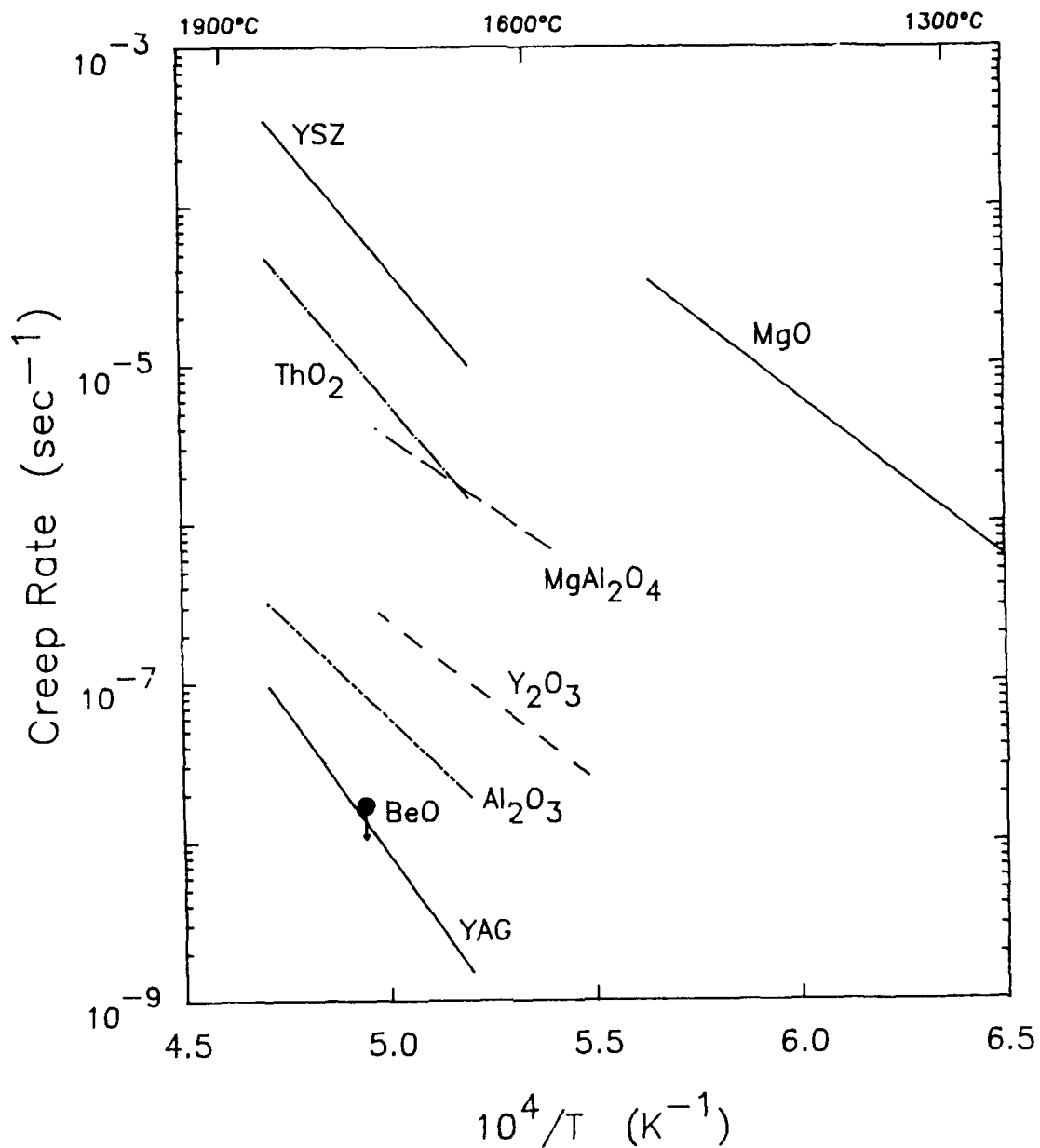


Figure 36. Creep Rates for several single crystal oxides at 100MPa.

MgO - [110], ref. 65	YSZ - [100], this study
ThO ₂ - [110], this study	MgAl ₂ O ₄ - [100], ref. 63
Y ₂ O ₃ - [110], ref. 64	Al ₂ O ₃ - [0001], this study
BeO - [0001], this study	YAG - [111], this study

tight tolerance machinery such as gas turbine engines, the amount of allowable deformation during the lifetime of any component is fairly low. If we assume a maximum tolerable strain of 1% for a 1000 hour lifetime component, then the maximum allowable creep rate would be 2.8×10^{-9} /sec. Accordingly, component designers often consider creep rates below 10^{-8} /sec. to be negligible. Of the materials tested, only YAG (and possibly c-axis BeO) approaches this creep rate at the modest stress of 100 MPa.

Of course, if the temperature or stress are reduced, or if more strain is allowed, then more materials become useful. Maximum use stresses or temperatures for each material can be estimated for a given level of allowable creep rate using the regression fits of Equation (6). Determined values of the constants A, n and Q are given in Table 11. Along with the estimates of G from Table 3, these constants and Equation (6) can be used to predict the creep behavior for a range of stresses and temperatures. For instance, assuming an allowable creep rate of 10^{-8} /sec, the maximum use temperature for an applied stress of 100 MPa, and the maximum allowable stress for a use temperature of 1650°C have been calculated and are listed in Table 12 (calculations were not done for [1101] BeO and 45° SiC due to their relatively poor creep resistance). Note that many of the estimates fall outside the range of the measurements, and thus should be considered only very approximate. Also, the relative ranking of the materials can vary with conditions due to the different temperature and stress dependencies of creep rates for the different materials. Nevertheless, these estimated limits do indicate several general trends. The creep limited use temperatures and stresses are considerably lower for the fluorite structure materials, YSZ and ThO_2 , than for the other oxides. Here again YAG comes out at least as well, and most times better than c-axis sapphire. In fact, the stress limits for YAG at 1650°C are about the same as for the c-axis SiC; however, the temperature limit for SiC is much higher than any of the oxides due to its very low activation energy for creep.

The second problem to consider is how the generated data can be interpreted and utilized to identify other creep resistant materials. There are many material characteristics which have been assumed to influence the relative creep resistance of ceramic materials. The most widely quoted criteria are refractoriness, diffusivities of constituent ions, material structure, and dislocation behavior. While being far from an extensive collection of oxide single crystal creep data, the data presented in Figure 36 can be used to assess the relative usefulness of these criteria as applied to high-melting point oxides.

The "refractoriness" of a material generally refers to its melting temperature. As the melting point increases a given use temperature becomes a smaller fraction of the melting point, and the creep resistance is therefore assumed to improve. The fact that ThO_2 , which is the highest melting oxide known, exhibits such poor creep resistance indicates that this criterion has limited applicability. To demonstrate this, the creep data from Figure 36 have been replotted in Figure 37, where creep rate is shown as a function of reciprocal homologous temperature. Were melting point a substantial factor in predicting creep behavior such a treatment should act to lessen the differences between the different materials. Clearly, this is not illustrated by Figure 37.

Table 11. Values of A, n, and Q Determined from Regression Fitting of the Creep Data to Equation 6.

Material and Orientation	A (K/Pa-sec)	n	Q (kJ/mole)
[100] YSZ	5.01×10^{13}	4.73	530
[110] YSZ	5.60×10^9	4.07	436
[111] YSZ	1.86×10^{10}	4.07	436
[100] ThO ₂	5.21×10^{29}	10.25	473
[110] ThO ₂	3.04×10^{21}	6.55	591
[100] YAG (low)	1.25×10^{11}	2.69	674
[100] YAG (high)	4.86×10^{65}	9.53	2064
[110] YAG (low)	6.77×10^{19}	6.18	650
[110] YAG (high)	2.71×10^{82}	12.46	2390
[111] YAG	5.94×10^{19}	5.64	710
$\bar{1}\bar{1}\bar{0}\bar{0}$ BeO	1.33×10^9	3.38	496
[1101] BeO	2.11×10^{22}	4.66	376
[0001] Al ₂ O ₃	1.90×10^{11}	4.54	470
[0001] SiC	1.64×10^3	4.95	170
45° SiC	2.45×10^8	3.32	282

**Table 12. Estimated Temperature and Stress Limitations
for an Allowable Creep Rate of 10^{-8} /sec.**

Material and Orientation	Maximum Temperature at 100 MPa (°C)	Maximum Stress at 1650°C (MPa)
[100] YSZ	1350	25
[110] YSZ	1275	17
[111] YSZ	1225	13
[100] ThO ₂	1315	53
[110] ThO ₂	1435	48
[100] YAG	1610	72
[110] YAG	1740	134
[111] YAG	1740	141
[$\bar{1}100$] BeO	1555	62
[0001] Al ₂ O ₃	1610	87
[0001] SiC	1970	144

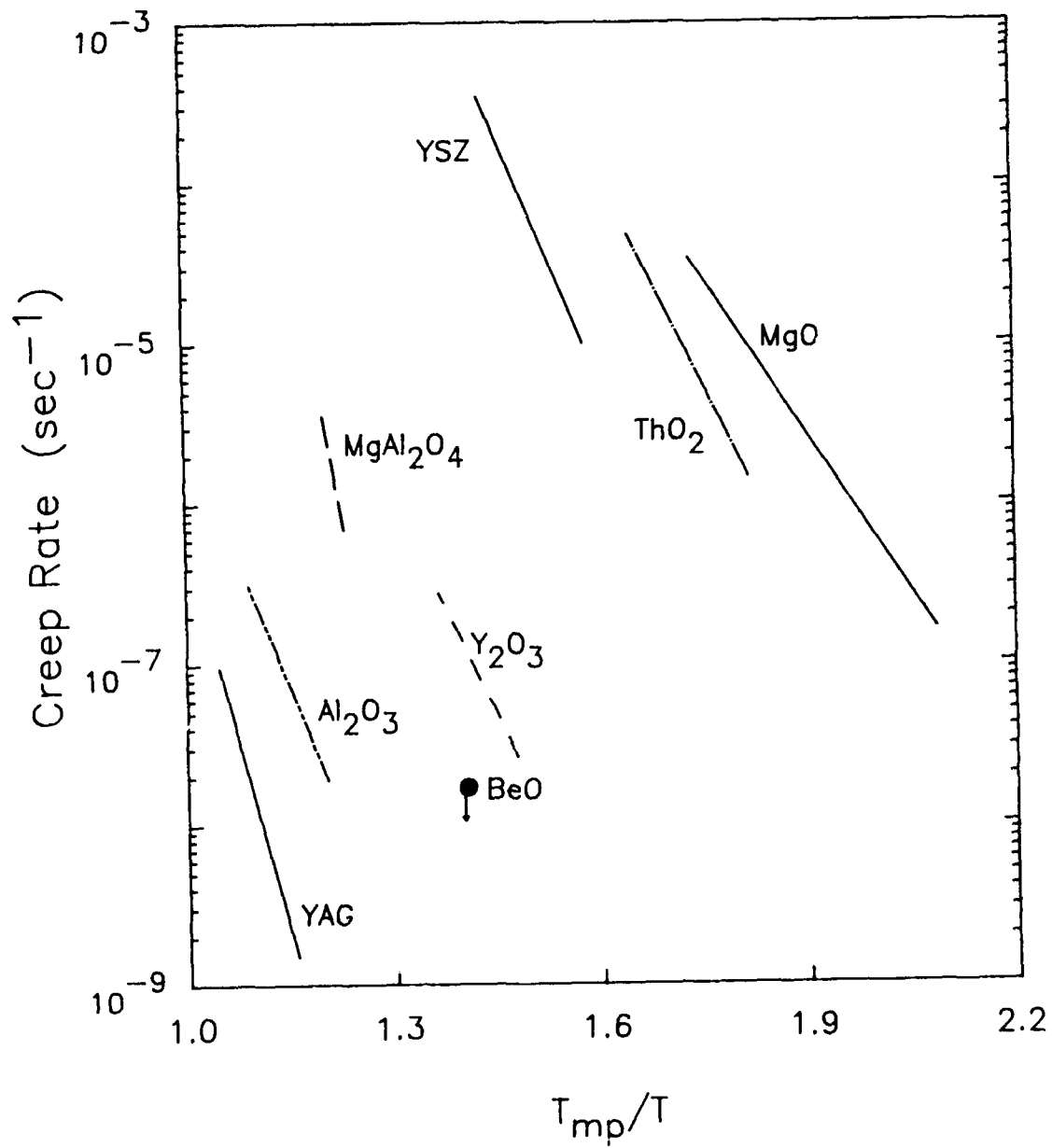


Figure 37. Creep rates at 100 MPa for several single crystal oxides as a function of inverse homologous temperature.

This is not to say that melting point cannot be a useful criteria. The materials included in Figures 36 and 37 were chosen specifically for their high melting points and thus represent a small subset of all oxides. Were data available on a wider range of oxides one would expect some rough correlation of creep resistance with melting point, especially for materials with the same structure. However, melting point does not appear to be a prime factor influencing the creep of high-melting oxide single crystals.

The second generally accepted criterion for predicting creep behavior is diffusivities in the material. Almost all theoretical models for creep include diffusivity as a term in the model equation. Indeed, the correlation between creep and diffusion activation energies in metals has been well established (66). However, the relationship is not nearly as clear for ceramic materials. In this study, only the data for the [111] and [110] YSZ showed any reasonable agreement between creep activation energy and diffusion activation energy. Also, diffusion data often does not exist for many materials of interest. When data is available from more than one source, it is often widely scattered or contradictory. This limits the usefulness of diffusivities for predicting creep behavior.

Bulk diffusivities for the materials in Figure 36 are plotted in Figure 38. Diffusion may play a role in the deformation of these single crystals by controlling the rate of dislocation climb. Since a flux of all ionic species is required for climb, the diffusivities controlling climb would be those of the slowest species in each material. As such, only the lowest self-diffusion coefficients are plotted in Figure 35. Based on this diffusivity data, one would expect the lowest creep rates for Al_2O_3 and ThO_2 , and the highest for Y_2O_3 and YAG. Clearly the ranking of materials based on diffusivities do not match those based on actual creep behavior. This would indicate that diffusivities are of limited utility for predicting creep behavior of a variety of oxides.

The nature, number and mobility of dislocations in a material is determined to a large extent by the structure of the material. Thus the effects of structure and dislocation characteristics on the deformation of single crystals cannot be fully separated. Structure/dislocation effects will therefore be discussed in tandem.

In this study, structure has been found to have two distinct effects. The first of these has to do with the anisotropy of the creep behavior. The materials tested are all either cubic or hexagonal, with the degree of anisotropy being much greater for the hexagonal materials. Therefore, proper comparisons of the hexagonal materials requires the recognition of orientation effects.

Figure 39 shows a plot of the applied stress necessary to cause a deformation rate of 10^{-5} /sec for the hexagonal materials studied. The lines in Figure 39 for SiC, BeO and c-axis Al_2O_3 were calculated from the regression fits to the creep data measured in this study. The data for a-axis and off-axis Al_2O_3 were taken from References 67 through 69. This plot clearly shows the severe anisotropy of these materials. Using the sapphire data as an example, the stress needed to generate the given creep rate is a factor of 40 less for off-axis crystals as it is for c-axis crystals at the same temperature. Alternately, extrapolation of the off-axis data indicates that, for the same level of stress, off-axis sapphire temperature limits are 700° to 800°C lower than for c-axis sapphire. The plot also indicates that BeO has a much larger

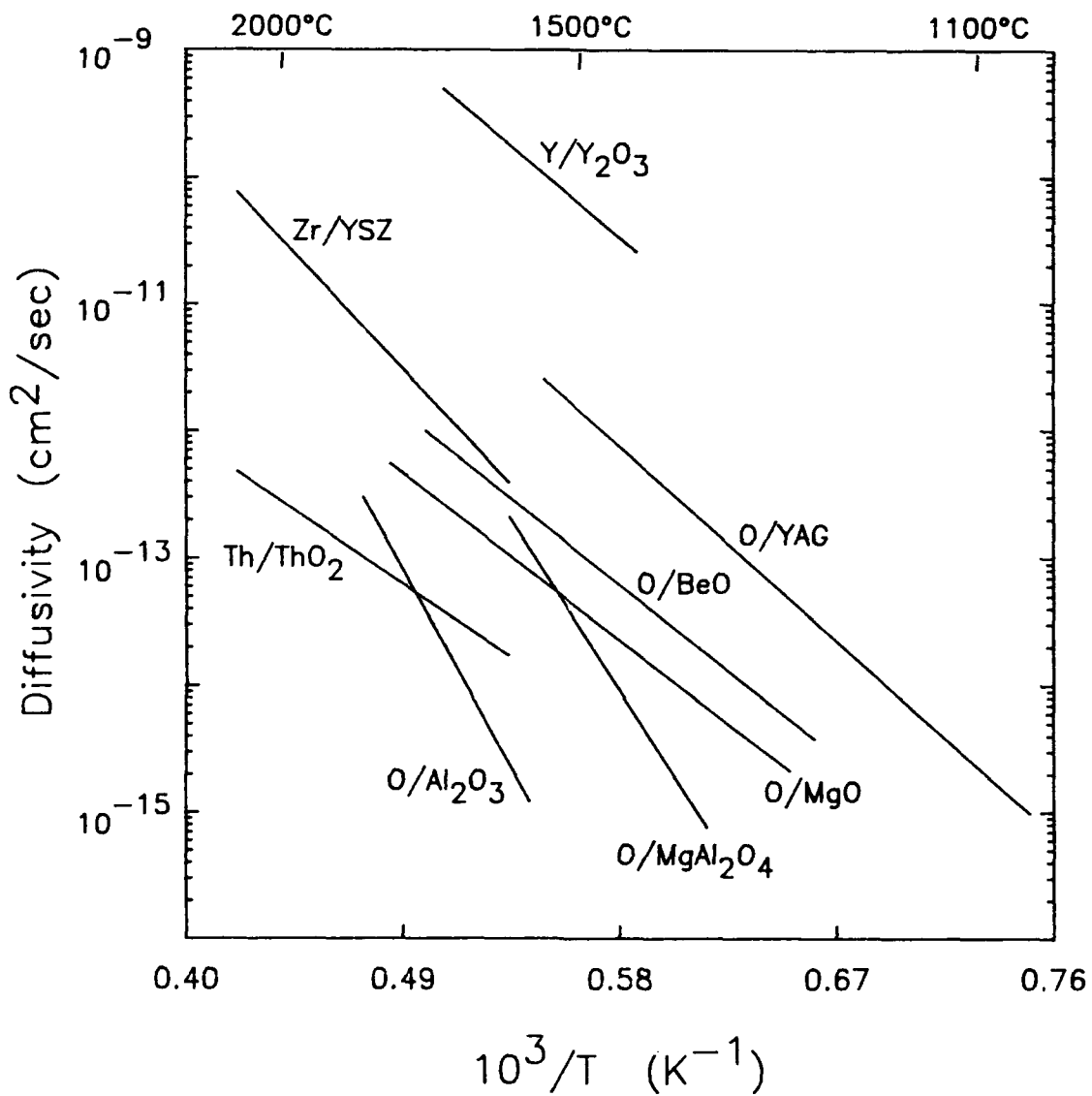


Figure 38. Bulk diffusivities for the slower moving species in a number of oxides.

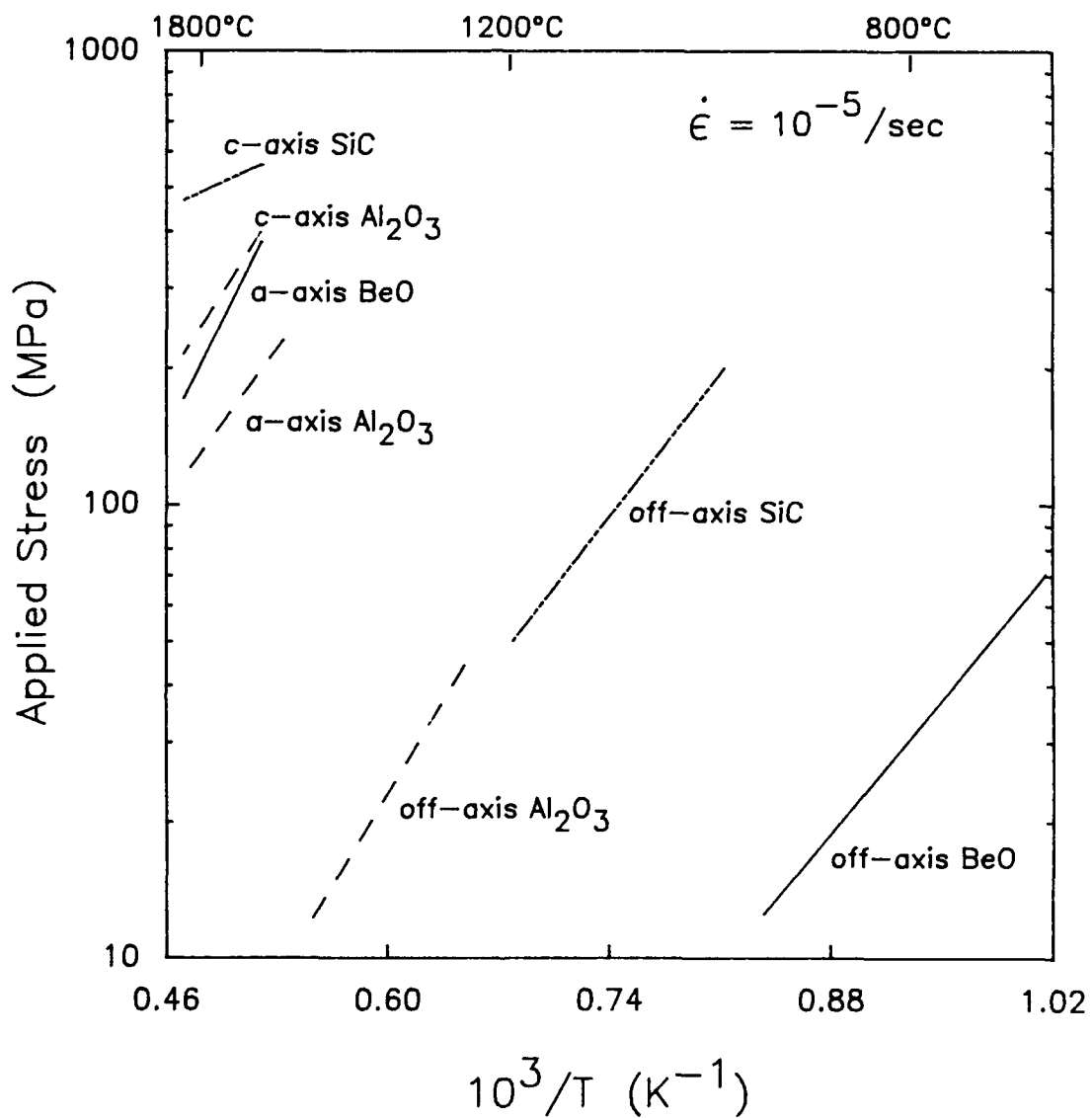


Figure 39. Flow stress at a deformation rate of $10^{-5}/\text{sec}$ for various orientations of BeO, Al₂O₃ and SiC.

creep anisotropy than either the sapphire or SiC.

This large creep anisotropy of hexagonal materials can be considered as either a blessing or a curse. On the positive side, the symmetry of the crystals allow one to orient the samples (or fibers) in such a manner as to eliminate, for a uniaxial stress, deformation by the basal and prismatic slip systems (i.e., the c-axis orientation). Since pyramidal slip is much harder to activate than basal or prismatic, c-axis aligned fibers would have very low axial creep rates, as demonstrated by the c-axis creep data measured here. However, this only holds for true uniaxial loading. In real composite components, where the component shape, fiber orientations and stress conditions are seldom simple, it is highly unlikely that the reinforcement fibers will see such a simple stress state. Any bending, shear or off-axis loading of the fibers could cause severe deformation of the fibers via basal slip, thereby changing the crystallographic direction of the fiber axis and possibly creating steps or bends in the fibers. The consequences of such fiber deformation on the fracture properties of the composites are likely to be very deleterious. It is thus considered unlikely that highly anisotropic (with respect to creep) fibers will be suitable for long-term use at high temperatures except under well controlled stress conditions, or with highly engineered multi-dimensional fiber architectures.

Anisotropy of the cubic materials, as would be expected from the crystal symmetry, was much lower. As indicated in Table 12, differences in allowable stresses at 1650°C are within a factor of 2 from the worst to best directions. This means that the crystallographic axis of the fiber can still be chosen for best axial creep resistance without sacrificing significantly in the off-axis or shear behavior.

Among the cubic materials, the outstanding creep resistance of YAG was somewhat surprising. At this time, we believe the good creep resistance of YAG is related primarily to its structure and dislocation size. To understand this it is necessary to consider the mechanism of deformation of these single crystal oxides. Since grain boundary sliding is not possible, and diffusion distances are too great for macroscopic deformation via diffusion, the deformation behavior is undoubtedly controlled by dislocation motion. To minimize the creep rates of the material one would therefore like to minimize the dislocation density, mobility by glide, and mobility by climb. Dislocation climb is controlled by self-diffusion of the material, which was discussed above. Diffusivities in many oxides can be significantly influenced by controlling the point defect equilibria of the material with doping. Such effects have not been considered in this study. Moreover, the deformation behavior of most of the materials studied does not appear to be strongly linked to diffusion as the creep activation energies did not match those for self-diffusion.

This leaves dislocation density and mobility by glide as the two factors of interest. Dislocation densities are influenced by a large number of material and crystal preparation parameters. To a first approximation, however, one would expect the ease of generating dislocations to be inversely proportional to the energy required. The line energy of a dislocation is given by

$$E = \alpha Gb^2 \quad (7)$$

where E is the line energy, G is the shear modulus, b is the magnitude of the Burger's vector, and α is a constant on the order of 1. Thus a high shear modulus and large Burger's vector should help to limit the number of dislocations.

One would also like to minimize the glide mobility of the dislocations. The main barrier to dislocation glide in a material is the Peierls-Nabarro stress, which represents an intrinsic stress or energy barrier the moving dislocation must overcome. This stress can be expressed, again to a first approximation, by the equation

$$\gamma = 2G/(1 - \nu) e^{(-2\pi a/b(1-\nu))} \quad (8)$$

where ν is Poisson's ratio and a is the spacing between slipped and unslipped planes (on the order of an interatomic distance). Thus to maximize the Peierls-Nabarro stress one again desires a high shear modulus and large Burger's vector.

Values for room temperature shear moduli and Burger's vectors for the cubic materials shown in Figure 35 are listed in Table 13. The shear modulus for YAG is on the high side for the oxides listed, but is lower than that for MgO. Since MgO has relatively poor creep resistance, shear modulus effects alone cannot explain the YAG results. However, the trend in creep resistance closely follows the trend in magnitude of the Burger's vector. The material with the largest b , YAG, also has the best creep resistance, and the material with the smallest b , MgO, has the poorest creep resistance.

Clearly the list of materials in Table 13 is far from extensive, and the correlation between creep resistance and Burger's vector may be somewhat fortuitous. However, this trend has been noted previously in the literature (70). Since no other clear correlations between creep behavior and crystal properties were identified, the trend between large b and good creep resistance could be used as a selection criterion for identifying other potentially creep resistant oxide single crystals. One should therefore look for oxides with complex structures, having large unit cells, which will generally require a large Burger's vector.

**Table 13. Shear Moduli and Burger's Vectors
for Several Cubic Oxides**

Material	Shear Modulus (GPa)	Lattice Parameter (nm)	Glissile b	Magnitude of b (nm)
MgO	139	0.420	$1/2\langle 110 \rangle$	0.297
YSZ	59	0.514	$1/2\langle 110 \rangle$	0.363
ThO ₂	101	0.559	$1/2\langle 110 \rangle$	0.395
MgAl ₂ O ₄	109	0.806	$1/2\langle 110 \rangle$	0.570
Y ₂ O ₃	66	1.061	$1/2\langle 110 \rangle$	0.750
YAG	117	1.201	$1/2\langle 111 \rangle$	1.040

5. CONCLUSIONS AND RECOMMENDATIONS

Compressive creep testing of several single crystal materials was performed primarily in the temperature range 1650° to 1850°C. The equivalence of the compressive tests with tensile creep testing of filaments was demonstrated by comparing data generated on c-axis sapphire with previous data from the literature. Compressive creep testing is therefore considered a viable method for evaluating the creep behavior of single crystal filament candidate materials.

Results for single crystal yttria-stabilized zirconia and thoria indicate rather poor creep resistance of these materials, despite their high melting points and low cation diffusivities. It is therefore considered unlikely that a creep resistant fiber could be developed from any oxide with the fluorite structure. Creep activation energies for [110] and [111] alignments of the yttria-stabilized zirconia are consistent with deformation being controlled by cation diffusion.

Of the materials tested, yttrium aluminum garnet displayed the best creep resistance. Creep rates for YAG were comparable to or lower than creep rates for c-axis sapphire at the same stresses and temperatures. To the best of our knowledge, this makes YAG the most creep resistant oxide known for which quantitative data exist. Also, anisotropy of YAG deformation behavior, due to its cubic structure, is relatively small. YAG therefore represents the best oxide candidate to date for development of creep resistant, single crystal filament reinforcements.

The creep behavior of beryllia is very anisotropic. An alignment allowing basal slip was found to creep appreciably at temperatures as low as 650°C, whereas [1100] aligned crystals displayed creep rates intermediate between those of a-axis and c-axis sapphire. Due to platen deformation and reactivity problems, quantitative creep data could not be obtained for c-axis BeO; however, based on a single semi-quantitative observation, c-axis BeO is anticipated to have comparable or superior creep resistance to that of YAG. Thus c-axis BeO is probably a viable reinforcement candidate. Unfortunately, the extreme anisotropy in creep behavior will probably greatly limit the usefulness of BeO as a high temperature composite reinforcement.

The creep behavior of high-purity single crystal 6H SiC has also been determined. Again, creep behavior was very anisotropic with crystals stressed at 45° to the c-axis showing measurable creep at temperatures as low as 800°C. Measured creep rates for c-axis crystals were comparable to those for polycrystalline sintered or reaction bonded SiC materials, and an order of magnitude higher than a CVD SiC. There thus appears to be no advantage of single crystal over polycrystalline SiC with regard to creep behavior. However, significant shear of the c-axis specimens via basal slip was observed during testing, which may have increased the measured creep rate due to off-axis stresses. As such, the results for c-axis SiC need to be independently corroborated.

Review of the creep data generated here and from the literature indicates that material structure appears to be the dominant factor controlling creep behavior of highly refractory single crystal oxides. A direct relationship between creep resistance and size of the glissile dislocation Burger's vector is suggested. As such, future investigations into creep resistant, single crystal oxides should consider materials with complex crystal structures and large unit cells.

REFERENCES

1. W.B. Hillig, "Prospects for Ultra-High-Temperature Ceramic Composites," in Tailoring Multiphase and Composite Ceramics, R.E. Tressler, G.L. Messing, C.G. Pantano and R.E. Newnham eds., Plenum Publishing Corp., 1986, pp. 697-712.
2. A. Dominguez-Rodriguez, K.P.D. Lagerlof and A.H. Heuer, "Plastic Deformation and Solid Solution Hardening of Y_2O_3 -Stabilized ZrO_2 ," J. Am. Ceram. Soc., 69(3) 281-284 (1986).
3. A. Dominguez-Rodriguez, V. Lanteri and A.H. Heuer, "High Temperature Precipitation Hardening of Two-Phase Y_2O_3 -Stabilized ZrO_2 Single Crystals: A First Report," J. Am. Ceram. Soc., 69(3) 285-287 (1986).
4. A. Dominguez-Rodriguez and A.H. Heuer, "Plastic Deformation of Y_2O_3 Stabilized ZrO_2 (YSZ) Single Crystals," Cryst. Latt. Def. and Amorph. Mat., 16, 117-123 (1987).
5. Engineering Property Data on Selected Ceramics, Vol. III, Single Oxides, Battelle Columbus Labs, Columbus, Ohio, 1981.
6. P.J. Dixon-Stubbs and B. Wilshire, "Deformation Processes During Creep of Single and Polycrystalline CaO," Phil.Mag.A, 45(3) 519-529 (1982).
7. L. Eyring, "The Binary Rare Earth Oxides," in Handbook of the Physics and Chemistry of Rare Earths, Vol. 3, K.A. Gschneider and L. Eyring eds., North Holland Publishing Co., New York, 1979, pp. 337-399.
8. H. Garem, J. Rabier and P. Veyssiere, "Slip Systems in Gadolinium Gallium Garnet Single Crystals," J.Mat.Sci., 17, 878-884 (1982).
9. B.M. Wanklyn, Clarendon Laboratory, personal communication.
10. S.B. Austerman, "Flux Process for Growth of Large Crystals with Application to Beryllia," J. Cryst. Growth, 42, 284-288 (1977).
11. K. Nassau, "Cubic Zirconia, The Latest Diamond Imitation and Skull Melting," Lapidary Journal, 31, 900-904, 922-926 (1977).
12. K. Nassau, "Cubic Zirconia: An Update," Lapidary Journal, 35(6) 1194-1200, 1210-1214 (1981).
13. J. Fitzgibbon, Saphikon, Inc., personal communication.
14. K.C. Goretta and J.L. Routbort, "Effect of Aspect Ratio on Compression of MgO Single Crystals," J.Mat.Sci.Lett., 6, 862-864 (1987).
15. W.R. Cannon and T.G. Langdon, "Creep of Ceramics, Part 1; Mechanical Characteristics," J. Mat. Sci., 18, 1-50 (1983); "Creep of Ceramics, Part 2; An Examination of Flow Mechanisms," *ibid.*, 23, 1-20 (1988).

16. Z. Hashin and S. Shtrikman, "On Some Variational Principles in Anisotropic and Nonhomogenous Elasticity," *J. Mech. Phys. Solids*, 10, 335-342 (1962); "A Variational Approach to the Theory of the Elastic Behavior of Polycrystals," *ibid.*, 10 343-352 (1962).
17. R.P. Ingel and D. Lewis III, "Elastic Anisotropy in Zirconia Single Crystals," *J. Am. Ceram. Soc.*, 71(4) 265-271 (1988).
18. H.M. Kandil, J.D. Greiner and J.F. Smith, "Single-Crystal Elastic Constants of Yttria-Stabilized Zirconia in the Range 20° to 700°C," *J. Am. Ceram. Soc.*, 67(5) 341-346 (1984).
19. S. Spinner, L. Stone, and F.P. Knudsen, "Temperature Dependence of the Elastic Constants of Thoria Specimens of Varying Porosity," *J. Res. Natl. Bur. Stds.*, 67C(2) 93 (1963).
20. S. Spinner, F.P. Knudsen and L. Stone, "Elastic Constant-Porosity Relations for Polycrystalline Thoria," *J. Res. Natl. Bur. Stds.*, 67C(1) 39 (1963).
21. R.E. Fryxell and B.A. Chandler, "Creep, Strength, Expansion, and Elastic Moduli of Sintered BeO as a Function of Grain Size, Porosity, and Grain Orientation," *J. Am. Ceram. Soc.*, 47(6) 283-291 (1964).
22. E.G. Spencer, R.T. Denton, T.B. Bateman, W.B. Snow and L.G. VanUitert, "Microwave Elastic Properties of Nonmagnetic Garnets," *J. Appl. Phys.*, 34(10) 3059-3060 (1963).
23. W.J. Alton and A.J. Barlow, "Temperature Dependence of the Elastic Constants of Yttrium Aluminum Garnet," *J. Appl. Phys.*, 38(7) 3023-3024 (1967).
24. T. Goto, O. Anderson, I. Ohno and S. Yamamoto, "Elastic Constants of Corundum up to 1825K," *J. Geophys. Res.*, 94(B6) 7588-7602 (1989).
25. T.D. Gulden, "Mechanical Properties of Polycrystalline α -SiC," *J. Am. Ceram. Soc.*, 52(11) 585-590 (1969).
26. A.G. Evans and R.D. Rawlings, "The Thermally Activated Deformation of Crystalline Materials," *Phys. Stat. Sol.*, 39, 9-31 (1969).
27. M.L. Mecartney, W.T. Donlon and A.H. Heuer, "Plastic Deformation in CaO-Stabilized ZrO₂ (CSZ)," *J. Mat. Sci. Lett.*, 15, 1063-1065 (1980).
28. Y. Oishi, K. Ando, and Y. Sakka, "Lattice and Grain-Boundary Diffusion Coefficients of Cations in Stabilized Zirconias," in *Advances in Ceramics, Vol. 7, Additives and Interfaces in Electronic Ceramics*, M.F. Yan and A.H. Heuer eds., American Ceramic Society, Columbus, Ohio, 1983, pp. 208-219.
29. R. Lagneborg, "Dislocation Mechanisms in Creep," *Intl. Metall. Reviews*, 17, 130-146 (1972).

30. M.S. Seltzer and P.K. Talty, "High-Temperature Creep of Y_2O_3 -Stabilized ZrO_2 ," J. Am. Ceram. Soc., 58(3-4) 124-130 (1975).
31. D. Dimos and D.L. Kohlstedt, "Diffusional Creep and Kinetic Demixing in Yttria-Stabilized Zirconia," J. Am. Ceram. Soc., 70(8) 531-536 (1987).
32. R. Duclos and J. Crampon, "High-Temperature Deformation of a Fine-Grained Zirconia," J. Mat. Sci. Lett., 6, 905-908 (1987).
33. K. Ando, Y. Oishi and Y. Hidaka, "Self-Diffusion of Oxygen in Single Crystal Thorium Oxide," J. Chem. Phys., 65(7) 2751-2755 (1976).
34. R.J. Hawkins and C.B. Alcock, "A Study of Cation Diffusion in UO_2 and ThO_2 Using α -Ray Spectrometry," J. Nuc. Mater., 26, 112-122 (1968).
35. A.D. King, "Thorium Diffusion in Single Crystal ThO_2 ," J. Nuc. Mater., 38, 347-349 (1971).
36. L.E. Poteat and C.S. Yust, "Creep of Polycrystalline Thorium Dioxide," J. Am. Ceram. Soc., 49(8) 410-414 (1966).
37. H. Haneda, Y. Miyazawa and S. Shirasaki, "Oxygen Diffusion in Single Crystal Yttrium Aluminum Garnet," J. Cryst. Growth, 68 581-588 (1984).
38. K.J. Roberts, "Dislocations in $Y_3Al_5O_{12}$," J. Mat. Sci., 16, 2517-2520 (1981).
39. V.G. Govorkov, N.N. Voinova, Kh.S. Bagdasarov and E.A. Stepanosov, "Plasticity of Single Crystals of Yttrium-Aluminum Garnet," Sov. Phys. Crystallogr., 20(5) 598-600 (1975).
40. J. Rabier, H. Garem and P. Veysiere, "Transmission Electron Microscopy Determination of Dislocation Burgers Vectors in Plastically Deformed Yttrium Iron Garnet Single Crystal," J. Appl. Phys., 47(11) 4755-4758 (1976).
41. J. Rabier, P. Veysiere, H. Garem and J. Grilhe, "Sub-Grain Boundaries and Dissociations of Dislocations in Yttrium Iron Garnet Deformed at High Temperatures," Phil. Mag. A, 39(6) 693-708 (1979).
42. H. Garem, J. Rabier and P. Veysiere, "Slip Systems in Gadolinium Gallium Garnet Single Crystals," J. Mat. Sci., 17, 878-884 (1982).
43. G.G. Bente and K.T. Miller, "Dislocations, Slip, and Fracture in BeO Single Crystals," J. Appl. Phys., 38(11) 4248-4257 (1967).
44. S.B. Austerman, "Self-Diffusion in Beryllium Oxide," J. Nuc. Mater., 14, 248-257 (1964).
45. J.B. Holt, "Self-Diffusion of Oxygen in Single-Crystal Beryllium Oxide," J. Nuc. Mater., 11, 107-110 (1964).
46. R.R. Vandervoort and W.L. Barmore, "Compressive Creep of Polycrystalline Beryllium Oxide," J. Am. Ceram. Soc., 46(4) 180-184 (1963).

47. W.L. Barmore and R.R. Vandervoort, "High-Temperature Plastic Deformation of Polycrystalline Beryllium Oxide," *J.Am.Ceram.Soc.*, 48(10) 499-505 (1965).
48. W.L. Barmore and R.R. Vandervoort, "High-Temperature Creep and Dislocation Etch Pits in Polycrystalline Beryllium Oxide," *J.Am.Ceram.Soc.*, 50(6) 316-320 (1967).
49. W.D. Scott, "Deformation Twinning in Ceramics," in *Deformation of Ceramic Materials II*, Materials Science Research Vol. 18, R.E. Tressler and R.C. Bradt eds., Plenum Press, New York, 1984, pp. 235-249.
50. P.J. Harrop, "Self-Diffusion in Simple Oxides," *J.Mat.Sci.*, 3, 206-222 (1968).
51. D.J. Gooch and G.W. Groves, "The Creep of Sapphire Filament with Orientations Close to the C-Axis," *J.Mat.Sci.*, 8, 1238-1246 (1973).
52. D.M. Kotchick, B.J. Busovne, R.E. Tressler and D.J. Barber, "Dynamics of Flow of C-Axis Sapphire," *J.Mat.Sci.*, 17, 1977-1987 (1982).
53. P. Shahinian, "High-Temperature Strength of Sapphire Filament," *J.Am.Ceram.Soc.*, 54(1) 67-68 (1971).
54. Dr. E. Hunker, Cree Research, personal communication.
55. K. Maeda, "Dislocation Glide Induced Plasticity of 6H SiC Single Crystals," *Yogyo Kyokai Shi*, 94(8) 784-789 (1986).
56. K Niihara, "Slip Systems and Plastic Deformation of Silicon Carbide Single Crystals at High Temperatures," *J.Less Common Met.*, 65 155-166 (1979).
57. J.D. Hong and R.F. Davis, "Self-Diffusion of Carbon-14 in High Purity and N-Doped α -SiC Single Crystals," *J.Am.Ceram.Soc.*, 63(9-10) 546-552 (1980).
58. J.D. Hong, R.F. Davis and D.E. Newbury, "Self-Diffusion of Silicon-30 in α -SiC Single Crystals," *J.Mat.Sci.*, 16, 2485-2494 (1981).
59. C.H. Carter, R.F. Davis and J. Bentley, "Kinetics and Mechanisms of High-Temperature Creep in Silicon Carbide: II, Chemically Vapor Deposited," *J.Am.Ceram.Soc.*, 67(11) 732-740 (1984).
60. C.H. Carter, R.F. Davis and J. Bentley, "Kinetics and Mechanisms of High-Temperature Creep in Silicon Carbide: I, Reaction Bonded," *J.Am.Ceram.Soc.*, 67(6) 409-417 (1984).
61. J.E. Lane, C.H. Carter and R.F. Davis, "Kinetics and Mechanisms of High-Temperature Creep in Silicon Carbide: III, Sintered α -Silicon Carbide," *J.Am.Ceram.Soc.*, 71(4) 281-295 (1988).
62. S. Prochazka, General Electric Corporate Research and Development, unpublished data.

63. R. Duclos, "High Temperature Deformation Mechanisms in MgO in Al₂O₃ Spinels," in Deformation of Ceramic Materials II, Materials Science Research Vol. 18, R.E. Tressler and R.C. Bradt eds., Plenum Press, New York, 1984, pp.159-175.
64. R.J. Garboriaud, "Fluage Haute Temperature du Sesquioxyde d'Yttrium: Y₂O₃," Phil.Mag., 44A(3) 561-587 (1981).
65. A.H. Clauer and B.A. Wilcox, "High Temperature Tensile Creep of Magnesium Oxide Single Crystals," J.Am.Ceram.Soc., 59(3-4) 89-96 (1976).
66. O.D. Sherby and A.K. Miller, "Combining Phenomenology and Physics in Describing the High Temperature Mechanical Behavior of Crystalline Solids," J.Eng.Mat.Technol., 101, 387-395 (1979).
67. D.M. Kotchick and R.E. Tressler, "Deformation Behavior of Sapphire Via the Prismatic Slip System," J.Am.Ceram.Soc., 63(7-8) 429-434 (1980).
68. R. Chang, "Creep of Al₂O₃ Single Crystals," J.Appl.Phys., 31(3) 484- 487 (1960).
69. M.L. Kronberg, "Dynamical Flow Properties of Single Crystals of Sapphire, I" J.Am.Ceram.Soc., 45(6) 274-279 (1962).
70. T.E. Mitchell, L.W. Hobbs, A.H. Heuer, J. Castaing, J. Cadoz and J. Philibert, "Interaction Between Point Defects and Dislocations in Oxides," Acta Met., 27, 1677-1691 (1979).